

University of Nottingham
UK | CHINA | MALAYSIA

Optimisation of encapsulated oil properties to maximise asphalt self-healing

Nilo Ruiz Riancho

Thesis submitted to the University of Nottingham for the degree of Doctor of Philosophy

March 2022

To my family and friends.

Abstract

The development of self-healing materials could make a relevant impact on our economy and environment, especially when the material is as widely used as asphalt. Asphalt mixture is a self-healing material, which implies that its cracks can close autonomously. The limitation is that self-healing occurs very slowly, and cracks tend to open faster than they close. There is evidence that the addition of encapsulated oil into the asphalt mixtures can improve their natural self-healing properties, which could significantly prolong their lifespan. Besides being a sustainable and resilient alternative, it does not require human action to activate the healing process, which is triggered automatically when the material has deteriorated. The oil released by the capsules reduces the viscosity of the bitumen, promoting the filling of the cracks by bitumen. Properties such as the internal structure, strength, and size of the capsules influence the oil release. However, in order to commercialise self-healing capsules as an additive for self-healing roads, they must not worsen properties of the road as specified by the Highways Agencies, such as skidding resistance, fatigue durability or rutting resistance.

Additionally, the high expenditure on road networks maintenance (around 10 billion euros in 2019 in Europe) is recently generating particular interest in increasing the durability of asphalt pavements. Encapsulated oil could represent a significant reduction of this expenditure from the governments of European countries. In addition to that, the CO_2 emissions related to the bitumen demand and traffic jams caused by the conventional maintenance techniques of roads could be significantly reduced.

The capsules containing sunflower oil which were investigated in this thesis were manufactured through the ionic gelation of alginate. The strength and the size of the capsules were varied to produce ten different types of capsules and perform a multivariable experimental study that aims to select the capsule size and strength

that optimise the asphalt self-healing properties for mitigating reflective cracking, skid resistance, fatigue durability, deformation under loading (rutting) and the amount of oil released in the bitumen. The influence of capsules' strength and size in their compressive strength and the influence of their thermal expansion, thermal resistance and internal structure in the release of the oil were also analyzed.

The capability of the encapsulated bitumen rejuvenators to mitigate the reflective cracking effect was assessed by reproducing the traffic-induced reflective cracks in stone mastic asphalt mixtures. Cyclical loading tests were carried out using a laboratory wheel tracker to analyse the fatigue durability, self-healing properties and rutting effect. Furthermore, computerised tomography scanning technology was used to analyse the changes in the internal structure of the capsules inside the asphalt. Finally, Fourier-transform infrared spectrometry was applied to measure the amount of oil released by the capsules.

The results showed that the strength of the capsules was influenced by the pore size of the calcium-alginate structure, the resistance of the capsules to the temperature reached during asphalt mixing and compaction and the fact that approximately 50% of the oil may not be released during self-healing. It was also concluded that the oil released does not influence the skid resistance, that capsules delay the reflective cracking of asphalt and that rutting increases proportionally to the oil released.

Finally, a discrete multi-physics model was implemented to investigate the mechanical response (including breakage and release of the internal liquid) of single core–shell capsules under compression as the first step to develop an automated capsule design system. The model combined Smoothed Particle Hydrodynamics for modelling the fluid and the Lattice Spring Model for the elastic membrane. Owing to the meshless nature of discrete multi-physics, the model can easily account for the fracture of the capsule's shell and the interactions between the internal liquid and the solid shell.

The simulations replicated a parallel plate compression test of a single core–shell capsule. The inputs of the model were the size of the capsule, the thickness of the shell, the geometry of the internal structure, the Young's modulus of the shell material and the density and viscosity of the fluid. The outputs of the model were the fracture type, the maximum force needed for the fracture and the force–displacement curve. The data were validated by reproducing equivalent experimental tests in the laboratory. The simulations accurately reproduced the breakage of capsules with different mechanical properties. The proposed model can be used as a tool for designing capsules that, under stress, break and release their internal liquid at a specific time.

Keywords: Self-healing asphalt; capsules; reflective cracking; optimisation; discrete Multiphysics model

Acknowledgements

First and foremost, I would like to express my extreme and sincere gratitude to my supervisor, Dr. Alvaro Garcia for his advice, mentorship, patience, and continuous moral and technical support during the whole PhD. The originality of his ideas and his perspective together with his immense knowledge and experience in the topic inspired and helped me immensely to complete this thesis.

This huge gratitude extends to Dr. Alessio Alexiadis for his unvaluable technical knowledge, patience and crucial support in a very important part of this thesis.

I would also like to thank Dr. Jose Norambuena, Dr. Daniel Grossegger and Dr. Tahseen Saadoon for his mentorship, advice, and technical support in the laboratory.

I also would like to acknowledge and extend my sincere gratitude to Dr. Gordon Airey and the technical staff of the Nottingham Transportation Engineering Centre (NTEC) for their assistance in the performance of the experimental testing required for this research.

I would like to thank Dr. Davide LoPresti for giving me the priceless opportunity of conducting my thesis in an international environment, and in the framework of the SMARTI ETN project which received funding from the European Union's H2020 Programme for research, technological development and demonstration under grant number 721493.

Finally, my most heartfelt gratitude to my family and friends for the unconditional moral support provided during the whole PhD.

List of Publications

1. J. Norambuena-Contreras, B. Gomez-Meijide, T. Al-Mansoori, E. Erkut, **N. Ruiz-Riancho**, Q. Liu, J-F. Su, A. Garcia, 'Self-healing capability of asphalt mixtures using encapsulated rejuvenators: an experimental approach by fatigue tests', 1st International conference of Sustainable Mega Infrastructures and 3rd International conference of Sustainable Construction Materials (SMI and SCM 2018), Wuhan, China, 2018.

2. A. Garcia-Hernández, S. Salih, **N. Ruiz-Riancho**, J. Norambuena-Contreras, R. Hudson-Griffiths, and B. Gomez-Meijide, 'Self-healing of reflective cracks in asphalt mixtures by the action of encapsulated agents', Constr. Build. Mater., vol. 252, p. 118929, 2020.

3. **N. Ruiz-Riancho**, T. Saadoon, A. Garcia, R. Hudson-Griffiths, 'Enhanced self-healing properties in stone mastic asphalt with encapsulated bitumen rejuvenators', RILEM International Symposium on Bituminous Materials, Lyon, France, 2020.

4. **N. Ruiz-Riancho**, A. Alexiadis, Z. Zhang, A. Garcia-Hernandez, 'A discrete multi-physics model to simulate fluid structure interaction and breakage of capsules filled with liquid under coaxial load', Processes, vol. 9, no. 2:354, 2021.

5. **N. Ruiz-Riancho**, A. Garcia, D. Grossegger, T. Saadoon, R. Hudson-Griffiths, 'Properties of Ca-alginate capsules to maximize asphalt self-healing properties', Constr. Build. Mater., vol. 284, 122728, 2021.

6. **N. Ruiz-Riancho**, T. Saadoon, A. Garcia, D. Grossegger, R. Hudson-Griffiths, 'Optimisation of self-healing properties for asphalts containing encapsulated oil to mitigate reflective cracking and maximize skid and rutting resistance', Constr. Build. Mater., vol. 300, 123879, 2021.

7. J. Norambuena-Contreras, Q. Liu, A. Gonzalez, A. Guarin, **N. Ruiz-Riancho**, A. Garcia, B. Wacker, J. L. Concha, 'Chapter 4. Advances in self-healing bituminous materials: from concept to large-scale application'. Kanellopoulos, A., Norambuena-Contreras, J. (Editors), 'Self-Healing Construction Materials: Fundamentals, Monitoring and Large-Scale Application', Springer., 2022. (Book chapter).

8. **N. Ruiz-Riancho**, L. Traseira Pineiro, M. Abedraba Abdalla, A. Garcia, 'Encapsulated bitumen rejuvenators for reflective cracking and ravelling mitigation'. 11th International Conference on the Bearing Capacity of Roads, Railways and Airfields (BCRRA), Trondheim, Norway, 2022.

Declaration

The research described in this thesis was conducted at the Nottingham Transportation Engineering Centre, the University of Nottingham between October 2017 and September 2021. I declare that the work is my own and has not been submitted for a degree at another university

Nilo Ruiz Riancho

The University of Nottingham

Contents

Abstract ..... **i**

Acknowledgements ..... **iv**

List of Publications ..... **v**

Declaration ..... **vii**

Contents ..... **viii**

List of Tables ..... **xiii**

List of Figures ..... **xiv**

CHAPTER 1 ..... **1**

1. Introduction **1**

1.1. Background 1

1.2. Motivation 3

1.3. Aims and objectives 5

1.4. Research methodology 6

CHAPTER 2 ..... **9**

2. Literature review **9**

2.1. Overview 9

2.2. Asphalt mixtures for pavements 10

2.2.1. Dense graded mixtures 10

2.2.2. Open-graded mixtures 11

2.2.3. Gap-graded mixtures 12

2.2.4. Stone Mastic Asphalt 13

2.3. Failures in pavements....14
2.3.1. Reflective cracking mitigation techniques....15
2.4. Self-healing asphalts....16
2.4.1. Self-healing by encapsulated rejuvenators....17
2.5. Encapsulation techniques....20
2.5.1. Physical/Mechanical techniques....20
2.5.2. Chemical techniques....22
2.5.3. Physicochemical techniques....24
2.6. Capsule characterization....28
2.6.1. Physicochemical methods....32
2.6.2. Structural methods....33
2.6.3. Mechanical characterisation....35
2.7. Release mechanism....40
2.8. Numerical modelling to simulate fluid-solid interactions and solid breakage in capsules....42
2.8.1. Mesh-free models....43
2.8.1. Solid-Fluid interactions....45
2.8.2. Deformable and breakable solids....49
2.8.4. Discrete multi-physics approach....53
CHAPTER 3....57
3. Materials and Methods....57
3.1. Introduction....57
3.2. Encapsulation procedure of the rejuvenator....58
3.3. Dimensions of the capsules....59
3.4. Capsule imaging....60

3.5. Computed Tomography X-ray Scanning 61

3.6. Quantification of ions released by the surface of a capsule's shell by ICP-OES.....61

3.7. Capsule strength to compression load.....62

3.8. Thermogravimetric analysis.....63

3.9. Influence of temperature and/or load on the oil-release from capsules ... .63

3.10. Asphalt mixture materials 64

3.11. Capsules that have been mixed in asphalt.....65

3.12. SMA beams manufacturing 66

3.13. Bulk density and air void content 67

3.14. Reflective cracking repeated loading durability 68

3.15. Quantification of crack self-healing.....69

3.16. Computed Tomography (CT) Scanning of asphalt mixture.....70

3.17. Capsule imaging of capsules after asphalt mixing and compaction 71

3.18. Amount of oil released by the capsules 71

3.19. Effect of capsules on the skidding resistance of asphalt.....72

3.20. Effect of capsules on the permanent deformation (rutting) of asphalt.73

CHAPTER 4 74

4. Properties of Ca-alginate capsules to maximise asphalt self-healing properties 74

4.1. Introduction.....74

4.2. Morphological characterization of Ca-alginate capsules that contain sunflower oil 75

4.3. Capsule components identification 78

4.4. Effect of the capsule's diameter and O/A ratio on the capsule's strength 79

4.5. Thermal degradation of capsules 84

4.6. Oil release due to heating-cooling cycles. Case 1.....85

4.7. Release of oil by the effect of load. Cases 2, 3 and, 4. 87

CHAPTER 5 91

5. Optimisation of self-healing properties for asphalts containing encapsulated oil 91

5.1. Introduction.....91

5.2. Density and air void content of SMA mixtures containing capsules...92

5.3. Reflective cracking repeated loading durability 93

5.4. Optimum resting time to maximize the self-healing of asphalt.....95

5.5. Influence of strength and capsules diameter in fatigue and self-healing properties.....100

5.6. Capsule oil release mechanism in asphalt mixtures.....103

5.7. Effect of the oil released on the skidding resistance.....106

5.8. Effect of the oil released on the rutting effect.....107

CHAPTER 6 109

6. Computational simulation of fluid-structure interaction and breakage of capsules. 109

6.1. Introduction.....109

6.2. Modelling approach 110

6.2.1. Smoothed Particle Hydrodynamics (SPH)..... 110

6.2.2. Lattice Spring Model (LSM)..... 111

6.2.3. Coupling the Two Models..... 113

6.3. Geometry 115

6.4. Main Simulation Parameters 116

6.5. Parametric Study and Influence of k_b and r_{max} 117

6.6. Validation of the Simulation of Capsule Compression between Two Parallel Plates 117

6.7. Influence of the Fluid on the Capsule's Strength 121

6.8. Deformability and Strength of the Capsule (a Parametric Study) 122

CHAPTER 7 125

7. Conclusions and Recommendations for Future Research 125

7.1. Conclusions 125

7.1.1. Capsule characterization to maximize asphalt self-healing properties 126

7.1.2. Optimisation of self-healing properties for asphalts containing encapsulated oil 127

7.1.3. Computational simulation of fluid-structure interaction and breakage of capsules 128

7.2. Recommendations for Future Research 129

REFERENCES 131

List of Tables

Table 1. Capsule characterisation methods.....29

Table 2. O/A ratios and capsule's sizes 60

Table 3. Design properties of the Stone Mastic Asphalt mixture 65

Table 4. Properties of the Ca-alginate capsules manufactured 66

Table 5. Main characteristics analysed of the different capsules tested. 77

Table 6. Pearson correlation coefficients of the relationships between roundness, diameter, pore diameter of the capsules and lose of weight. 78

Table 7. Weight loss (%) for each type of capsule at 160 ºC 85

Table 8. Median number of cycles resisted by the asphalts. Standard deviation is shown in brackets under the number of cycles. 94

Table 9. Parameters needed for Discrete Multi-Physics simulation. 114

List of Figures

Figure 1. Capsules, embedded inside a material, breaking because of a crack formation. Extracted from [1] 18

Figure 2. Encapsulation by co-extrusion 21

Figure 3. Schematic of spray-drying encapsulation technique (extracted from [72]) 22

Figure 4. Polymerisation induced phase separation method (Extracted from [73]) 23

Figure 5. Aqueous core microcapsules by solvent extraction and evaporation. (Extracted from [74]) 23

Figure 6. Interfacial polymerisation general procedure. (Modified from [75]) 24

Figure 7. Fabrication method of colloidosomes 25

Figure 8. Graphical representation of oil encapsulation by (a) external gelation, (b) internal gelation or (c) inverse gelation techniques. (Extracted from [72]) 26

Figure 9. SEM image of a capsule section showing its different layers. (Modified from [50]) 33

Figure 10. CT-Scan images of different capsules. (Extracted from [79]) 34

Figure 11. Membrane reactions for mechanical characterisation tests 35

Figure 12. Breaking force as a function of shell thickness of capsules. (Extracted from [91]) 37

Figure 13. Relation between diameter and wall thickness vs. molar ratio. (Extracted from [91]) 38

Figure 14. Example of a broken capsule after parallel compression test. (Extracted from [53]) 39

Figure 15. Compressive load vs. Displacement plot for one type of capsules and for temperatures. (Extracted from [53]) 40

Figure 16. Internal structure of catsand capsules (Left) and Ca-alginate capsules manufactured by internal ionic gelation (Right). 41

Figure 17. Internal structure for capsules manufactured by inverse ionic gelation. (Modified from [83]).....41

Figure 18. Connection between the numerical simulations, theories, and experiments 43

Figure 19. (a) Conforming mesh, (b) Non-conforming mesh and (c) Mesh-free. (Extracted from [107]) 46

Figure 20. Computational simulation of interface modification due to erosion. (Extracted from [109]) 47

Figure 21. Frames of crack evolution simulation because of hydrofracturing. (Extracted from [110]) 48

Figure 22. Simulation of a coffee cup hitting the ground and breaking into pieces. Meshless Local Petrov-Galerkin (MLPG) model applied. (Extracted from[117]).50

Figure 23. Simulation of a brittle object breaking because of the forces applied by jaws. SPH-biomechanical model applied. (Extracted from [120]) 51

Figure 24. Force-Displacement plot obtained from compression parallel test. (Extracted from [121]) 52

Figure 25. Snapshot of a cell fractured after the simulation of a compression test. (Extracted from [121]) 53

Figure 26. Flowchart for MPM-SPH multiphysics approach 54

Figure 27. Scheme of ionic external gelation of alginate and sunflower oil encapsulation.....59

Figure 28. (a) Compression test setup. (b) Capsule type 2-2.5/1 at the end of the compression test.....62

Figure 29. Aggregates gradation for the SMA mixtures.....65

Figure 30. Scheme of reflective cracking repeated loading test. 68

Figure 31. FTIR curves for the quantification of sunflower oil released by the capsules. Modified from [51].....72

Figure 32. (a) 3D reconstruction of a capsule type 1.3-2/1. (b) Internal structure of a capsule type 1.3-2/1. (c) Internal structure of a capsule type 1.3-3.5/1 obtained by CT scanning. (d) SEM image of the surface of a capsule type 1.3-2/1. (e) SEM image of the internal structure of a capsule type 1.3-2/1. (f) SEM image of the internal structure of a capsule type 1.3-3.5/1. 76

Figure 33. (a) Elemental identifying images. (b) Elemental mapping generated by energy-dispersive X-ray spectroscopy. (c) Calcium and sodium ions concentration after release from the capsule's surface. 79

Figure 34. Different stages in a parallel compression test for a single capsule type 3-2/1 80

Figure 35. Load (N) at Yield point for all the capsules studied, at 20 °C. 81

Figure 36. Yield stress at 20 ºC, 60 ºC, and 160 ºC, of capsules with (a) a range of diameters and (b) O/A ratios.....82

Figure 37. Thermogravimetric analysis curves for the different types of calcium alginate capsules manufactured 83

Figure 38. (a) Capsule's dimension change because of temperature changes. (b) Amount of oil released by the capsules after seven cycles of temperature change, ranging from -10 °C to 60 °C.....86

Figure 39. Percentage of oil released by 1.3 mm capsules at the different stages of a parallel compression test for different O/A ratio values.....88

Figure 40. (a) Percentage of oil released versus pore diameter in Case 4. (b) Load resisted at Yield Point, N, versus pore diameter for the different types of capsules manufactured.....89

Figure 41. (a) Air voids content and (b) bulk density of SMA mixture with and without capsules.....93

Figure 42. Influence of capsule diameter in the fatigue resistance, represented by the median number of cycles resisted by the asphalt.....95

Figure 43. Healing Index at different number of loading cycles applied over the SMA beams. (a) without capsules. (b) With capsules type C.....96

Figure 44. Relationship between healing index and amount of oil released by capsules.....97

Figure 45. X-ray tomography of the internal structure of an asphalt sample a) pre-loaded, b) after 30% of the median number N05 of cyclical loading and c) after applying resting period 98

Figure 46. (a) Healing index for capsules with different diameters but the same O/A ratio. (b) Relationship between the diameter of capsules and the healing index. ...99

Figure 47. Final asphalt lifespan increments for all the capsules studied. 100% in the vertical axis implies that asphalt has its current fatigue life. Values higher than 100 % implies that asphalt improved durability. 101

Figure 48. Healing index and fatigue index for SMA mixtures with different types of capsules.....102

Figure 49. 3D reconstruction and microscope surface's detail of a capsule type H extracted (a) after mixing and compaction and (b) after cyclical loading. SEM microscope images are taken of a capsule type H (c) after mixing and compaction and (d) after cyclical loading 104

Figure 50. Amount of oil released by capsules with different O/A ratio.....105

Figure 51. Skid resistance for the SMA mixtures studied 106

Figure 52. Relationship between the depth of rutting and the amount of oil released by the different types of capsules manufactured.....107

Figure 53. Particle representation and interactions among the computational particles. 112

Figure 54. Representation of two computed particle bonds breaking. 112

Figure 55. Initial simulation geometry.....115

Figure 56. Force–displacement curve obtained from a laboratory parallel plate compression test for a single core–shell capsule, from a simulated single core–shell capsule without fluid inside and from a simulated single core–shell capsule. 119

Figure 57. (a) Comparison between the deformation under coaxial load and (b) the fracture of a simulated elastic single liquid core–shell capsule by the Discrete Multi-Physics (DMP) approach and an elastic capsule of 16–50 μm being ruptured (from [151]).....120

Figure 58. Sequence of the simulation of the parallel compression test of a single liquid core–shell capsule at different stages 121

Figure 59. Simulated force–displacement curves for (a) kb = 1.6 N−1 m and different values of rmax, (b) kb = 4.7 N−1 m and different values of rmax and (c) kb = 1.6 N−1 m and different values of rmax.....123

Figure 60. Capsule fractures (view from the top) at the end of each simulation* 124

CHAPTER 1

1. Introduction

1.1. Background

The development of new materials able to rehabilitate themselves after being damaged by usage has advanced during recent years. Scientific and technological advances in the self-healing field have provided new materials with the ability of autonomous crack reparation. Additionally, other critical factors like reliability and durability should be enhanced for the successful development of a product [1]. Materials with these characteristics can be encompassed in smart materials classification, which have one or more significantly modifiable properties controlled by an external stimulus. Smart materials can be classified depending on the nature of this external stimulus (mechanical stress, temperature, moisture, pH and electrical or magnetic fields). However, self-healing materials can be classified into three groups based on the mechanism used to keep the healing functionality deactivated until triggered by damage (capsule, vascular and intrinsic) [2].

The research on self-healing materials based on encapsulation technology has grown exponentially in recent years, primarily due to the fact that the chemical structure of the matrix is not modified before the self-healing process takes place. The capsules are usually embedded inside other materials and the healing agent contained does not interact with the matrix of the main material until the activation of the capsule occurs. Once the healing agent is released, it interacts with the region of damage.

This mechanism is relatively simple and enhances the commercialisation of this technology.

Moreover, asphalt mixture is the most used material for the construction of pavements in the world [3]. Additionally, it is a natural self-healing material since bitumen can flow and fill the cracks that are generated in an asphalt road [4]. Previous researchers have explained the self-healing mechanism of asphalt through the drainage of bitumen into the cracks [5] and the compaction of the solid skeleton by traffic loads [6], which fills the cracks. In addition to that, the self-healing mechanism of asphalt results from the complex interplay between the chemo-physical properties of the asphalt [7], its geometry, temperature [8] and traffic loads. Two main types of self-healing asphalt technologies have been developed to accelerate the healing of asphalt properties that could mitigate or delay the reflective cracking. The first self-healing method is electromagnetic heating, which consists of adding conductive particles to the asphalt mixture and increasing their temperature by applying an induction or microwave field to heat the conductive materials, melt the bitumen and cause it to flow into the cracks. However, increasing the temperature repeatedly can induce ageing of the bitumen and an external device is required to heat the metals whereas the use of capsules is understood as a more autonomous process. The second self-healing method is based on the use of encapsulated bitumen solvents that reduce the viscosity of the bitumen, making it flow into cracks. This bitumen softening can also be related to the re-allocation of the aggregates in a more adequate disposition, changing the internal structure and generating the healing of some cracks.

The application of one of these automated maintenance techniques in asphalt pavements could generate a significant impact on transport infrastructures. According to the data from European Union [9], around 10 billion euros were invested in European road networks in 2016, to maintain the quality of the roads by applying conventional maintenance techniques. Furthermore, self-healing asphalts could indirectly reduce CO_2 emissions, the bitumen demand and traffic jams caused

by conventional techniques of road maintenance [3]. In addition, the use of self-healing asphalts containing encapsulated bitumen rejuvenators could prolong the lifespan of roads, which would mean a substantial economic saving for European countries. Due to the potential economic (capsule manufacturing process still needs to be optimised) savings and environmental benefits and taking into account that the operational health of the road network acts as an indicator of the economic and social welfare, encapsulating rejuvenators for self-healing asphalt could be considered as a reliable option for the replacement of conventional road maintenance techniques.

1.2. Motivation

Asphalt properties degrade over time through loading, climate conditions (UV rays and oxidation) and forming microcracks [10]. However, reflective cracking can appear after a short period [11] without bitumen oxidation. Reflective cracks in an asphalt layer are induced in a pavement mainly because of (i) thermal changes generating thermal contraction when the asphalt is placed over a hydraulic bounded or concrete base and (ii) excessive traffic loads [12]. To mitigate or delay reflective cracking in asphaltic overlays, researchers have proposed different treatments such as geogrids, fibre grids and steel messes which may cause problems with recycling the asphalt. Other drawbacks were found, particularly in the effectiveness of the application of fibre-glass grids, which is still uncertain and implies a high cost. Although some conventional maintenance techniques presented satisfactory results, they are difficult treatments to implement, as sometimes it is required a thick overlay and adjustments in other parts of the road.

Recent research [6] has indicated relevant potential in the use of encapsulated bitumen rejuvenators as a reflective cracking mitigation technique. However, the main challenge of self-healing asphalts is that the automated healing of cracks tends to be slower than their growth; this self-healing rate is even slower when pavements age due to bitumen oxidation and loss of volatiles [10]. Improving the self-healing

ability of asphalt is of utmost importance to reduce the frequency of maintenance activities that a road may require during its whole life, which, in turn, may save costs [3].

The use of encapsulated bitumen rejuvenators involves mixing encapsulated bitumen solvents in the asphalt [13], [14], such as vegetable oils, which are recyclable and readily available. When cracks appear in the asphalt, the capsules are compressed and they release the solvents, which soften the mixture locally [15]. The bitumen solvent released reduces the viscosity of the bitumen which, together with the effect of external traffic loading, promotes on the "re-compaction" of aggregates and the bitumen flow into the cracks [6]. In consequence, rutting might be promoted by this self-healing mechanism and the stiffness of the asphalt may be reduced [16].

Since this technology relies on the rupture and crushing of capsules to release solvents, it is crucial to determine the optimum strength and diameter of capsules for a timely release of the bitumen rejuvenator. Therefore, a compromised value for capsule strength needs to be found. The capsule strength should allow the capsule to release the bitumen rejuvenator when cracks start to appear, and also, to resist mixing and compaction in asphalt and be impermeable to the solvents [4]. The rupture and strength of the capsules are also expected to be related to the material and the internal structure (which is usually dependant on the encapsulation process). This opens a broad research field about the design of capsules with optimum properties, such as a slow release of the internal liquid, sometimes required by the final application.

Currently, capsules are designed for end-use applications by trial and error. However, in recent years, computer simulations have developed the potential to significantly accelerate their design by providing a method for predicting the capsule's behaviour in advance, based on previous detailed mechanical characterisation. The crucial parameters for the capsule design are the thickness of the capsule walls, the geometry of the internal structure, the Young's modulus of the capsule's matrix material.

1.3. Aims and objectives

The research presented in this thesis sought to achieve the following aims:

- Analyse the influence of the proportions of the capsule materials (oil, water, and alginate) on the strength and diameter of capsules for asphalt self-healing. In addition, it aims to provide a preliminary explanation about the diffusion of oil through the shell materials when the capsules are subjected to changes of temperature or compressive load is applied.
- Optimise capsule size and strength to maximise the self-healing properties of asphalt roads without compromising fatigue durability, skidding resistance and rutting resistance. The validation of the application of encapsulated bitumen rejuvenators as an effective technology for the reflective cracking mitigation is also aimed.
- Develop a three-dimensional numerical model to simulate the failure of liquid-core capsules, by validating experimentally capsule mechanical properties such as the Force-Displacement curve, Young's modulus and the type of fracture.

In order to accomplish these aims, it was necessary to achieve more specific goals such as:

- Develop an encapsulation method able to manufacture capsules with different sizes and strengths.
- Characterise the different capsules in terms of geometry, temperature susceptibility, mechanical resistance and morphology.
- Evaluate the effect of the capsules on the asphalt production process (mixing and compaction).
- Analyse the influence of the capsules' size and strength on the reflective fatigue durability and self-healing properties of asphalt. Cyclical loads were

applied over the samples by a laboratory wheel tracker to generate reflective cracking.

1.4. Research methodology

In order to accomplish the aforementioned objectives, the research methodology was divided into the following phases:

Phase 1: Capsule manufacture and characterisation.

A new set-up was designed which was able to produce capsules with different sizes and strengths. New equipment and materials were acquired for the set-up building and capsule manufacture. It was necessary to design a capsule manufacturing matrix which modified two variables: a) the drop size in the encapsulation process and therefore the capsule size and b) the proportions of the material to produce different types of capsules varying in strength. A preliminary assessment of the capsules manufactured was carried out by performing simple tests were performed, such as crushing the capsule by hand or using a hammer to roughly assess its strength after drying, measuring the capsule diameter using a calliper or visually checking the loss of oil in the capsule drying tray.

After manufacturing the capsules, their characteristics were evaluated and analysed in order to assess the influence of capsules' size and composition on their compressive strength, thermal expansion, thermal resistance, internal structure, and therefore, on the release of the oil within. A scanning electron microscope was used to image the surface of the capsules and their internal structure by cutting the capsules in two halves. The components in the surface of the capsule were determined by applying Inductively Coupled Plasma Optical Emission Spectroscopy (ICP-OES). The amount of oil contained by the capsules was quantified by applying computed tomography X-ray scanning. Finally, the thermal

and mechanical resistance of the capsules were assessed by thermogravimetric analysis and uniaxial parallel plate compression tests, respectively.

Phase 2: Assessment of the effect of the capsules' properties on the asphalt mechanical and self-healing properties

Ten different types of capsules with different sizes and strengths were manufactured. These ten types of capsules were used to generate ten different asphalt mixtures, in addition to the blank one without capsules. Several laboratory tests were carried out in order to assess the effect of the capsules' size and the strength in the mechanical and self-healing properties of asphalt. To reproduce the joints or discontinuities in underlying layers which cause the reflective cracks, cyclical loads were applied over the samples by a laboratory wheel tracker. Following this, the self-healing properties of asphalt were evaluated as the extension of its fatigue durability by comparing the results of asphalt with capsules to those of asphalt without capsules. Moreover, the skid resistance, rutting and the amount of oil released by the capsules were analysed to validate the capsules as an effective solution for reflective cracking. Finally, Computed Tomography (CT) scanning was used to analyse changes in the internal structure of asphalt when cyclical loads were applied.

Phase 3: Modelling and simulation.

The mechanical response of single core-shell capsules under compression, which includes breakage and internal liquid release, was investigated as a first step to develop a tool to design capsules with the properties required by a specific final application. A meshless discrete multi-physics approach was applied, combining Smoothed Particle Hydrodynamics for modelling the fluid and the Lattice Spring Model for the elastic membrane. The simulations replicated a parallel plate compression test of a single core-shell capsule. The inputs of the model were the size of the capsule, the thickness of the shell, the geometry of the internal structure,

the Young's modulus of the shell material, and the density and viscosity of the fluid. The outputs of the model were the fracture type, the maximum force needed for the fracture, and the force-displacement curve. The data were validated by reproducing equivalent experimental tests in the laboratory.

CHAPTER 2

2. Literature review

2.1. Overview

The development of materials able to self-repair the damage generated during their use, or by external factors, could have a positive impact on our society, especially when the material is as widely used as asphalt. It has been proven that encapsulated rejuvenators for self-healing asphalt can significantly prolong the lifespan of the asphalt. Besides being a sustainable and resilient alternative to conventional pavement maintenance methods, it does not require human action to activate the healing process. The self-healing ability of asphalt is potentiated automatically when the material is deteriorated by unfavourable weather conditions or the effect of the loads applied by the traffic.

The main aim of this chapter is to provide a literature review which can give an overview of the recent achievements related to self-healing asphalts, specifically applying encapsulated bitumen rejuvenators. Firstly, the different types of asphalt mixtures are described in this chapter together with their main characteristics. The typical failures that affect asphalt pavements are also reviewed in this section, paying close attention to reflective cracking and the conventional techniques applied to mitigate this pavement distress. Secondly, this chapter also delves into the bitumen rejuvenator encapsulating processes and the types of rejuvenators currently available in the market for self-healing asphalts, the optimisation of the capsules

with respect to capsule size and strength. Additionally, several computational alternatives for modelling capsules were investigated to provide a more complete picture of the different requirements to simulate the mechanical behaviour of a single capsule when it breaks under compressive loads.

2.2. Asphalt mixtures for pavements

Asphalt mixture is composed of coarse and fine aggregates, which size ranges from a few microns up to a few centimetres and give structural stability through particle interlocking, and bitumen, which is a liquid, which viscosity is temperature-dependant, and keeps the aggregates together and seals the pavement from water. Temperatures between 100 °C and 190 °C are required to coat the aggregates with bitumen during the mixing process. Asphalt is the most used material in terms of pavements construction.

An asphalt pavement is composed of several layers. The intensity of stresses is highest at the top layer; hence, it requires higher quality materials [17]. In this top layer is where the capsules could be implemented. The most widely used upper pavement material is hot mix asphalt (HMA). Hot mix asphalts can be mainly divided into three families based on the gradation: dense gradation, open-graded or open or porous mixtures and gap-graded or mixtures of incomplete granulometry.

2.2.1. Dense graded mixtures

Dense gradations are commonly subdivided into continuous gradation or conventional HMA, large-stone mixture, and sand-asphalt mixture. Dense grading HMA are composed of bitumen and aggregate of continuous gradation.

Conventional HMA mixtures consist of aggregates of nominal maximum size in the range from 12.5 mm to 19 mm.

Large-stone mixtures contain coarse aggregates with a nominal maximum size greater than 25 mm. These mixtures have a higher percentage of coarse aggregates (larger than 4.75mm sieve) than conventional mixes. Due to the larger size of the aggregates, the compaction stress applied to the mixture must be monitored to prevent excessive fractures of the major aggregates during the compaction process.

Asphalt-sand mixture is composed of aggregate that passes the 9.5 mm. The bitumen content in the mixture is higher than for conventional HMA mixes because the voids content in the mineral aggregate of the mixture is higher. The nature of the aggregate used in this type of mixture is crushed stones or natural sands with a rough texture, and the resistance to permanent deformation of this type of mixture is typically meagre.

2.2.2. Open-graded mixtures

Open-graded mixtures are divided into open-graded friction courses (OGFC) and permeable bases treated with asphalt.

Open-graded mixtures consist of a relatively uniform mixture. Modified bitumen can be applied for some application. The primary purpose of this type of mixtures is to serve as a drainage layer, both on the pavement surface or within the pavement structure.

As indicated, there are two types of open-graded mixtures. OGFC is used as a coarse surface to provide free drainage on the surface and prevent puddles, reduces tire splashing, and reduces tire noise. On the other side, permeable base treated with asphalt, comprises a uniform gradation of nominal maximum size bigger than those used in OGFC (19 mm to 25 mm) and is used to drain water penetrated into the pavement structure from the surface or the subgrade.

The production of open-graded mixtures is similar to dense-graded mixes. However, lower mixing temperatures are applied to prevent runoff from hot asphalt or drain down during storage or transfer to the project site.

Recently, polymers and fibres have been introduced in open-graded friction course mixtures to reduce the drain down and improve the mixture's durability. In addition, compaction stress is generally less than in dense grading mixtures.

2.2.3. Gap-graded mixtures

The gap-graded type encompasses gap-graded asphalt concrete mixtures and Stone Mastic Asphalt (SMA) mixtures. The function of gap-graded mixtures is similar to dense-graded mixtures because they also provide dense waterproof layers when compaction is appropriate. The aggregates are usually ranged from coarse to fine, with little presence of intermediate sizes.

The production of SMA mixtures requires incorporating significant amounts of mineral filler into the standard aggregate to reach 8 to 10% of material that passes the sieve 0.075 mm. The discharge temperature of the SMA mixtures needs to be controlled to prevent runoff or drain down of the binder during storage or transport. In addition to that, fibres and polymers are typically used with SMA to prevent drain down.

Additionally, some HMA mixtures must be designed for particular application considering factors such as traffic, environment, subgrade, existing pavement conditions and its preparation, and economic evaluation. For example, some open-graded friction course (OGFC) mixtures are designed to improve friction, avoid puddles, and vapour emanations from the pavement, and reduce noise levels.

2.2.4. Stone Mastic Asphalt

Stone mastic asphalt (SMA) is a type of gap-graded bituminous mixture with high contents of stone, filler and bitumen, originally produced in Germany, globally known for its durability and rut resistance [18]. The difference between SMA and the traditional types of hot mix asphalt (HMA) is that SMA is thin and gap-graded. The philosophy of SMA is based on the increasing of durability by incorporating a high asphalt binder content and using aggregates with a high voids content in mineral aggregate in order to be filled with bitumen [19]. As explained [20], gap-graded asphalt mixtures are defined as mixtures that have less mid-sized aggregates, therefore their strength comes from the coarse aggregate skeleton bound created by bitumen, rather than the aggregate interlock formed when the mixture is well-graded.

SMA have been included in mainland as the main asphalt mixture for the construction of heavily trafficked roads, airport taxiways and runways, bridge deck surfacing, container storage areas and bus stops.

The main benefits may be described as follows:

- high resistance to rutting
- high resistance to cracking
- high durability
- wear and ravelling resistance
- insensitivity to water
- good skid resistance
- low surface noise
- superior surface finish

The principal attraction of the material, though, is the unique combination of deformation resistance and durability.

2.3. Failures in pavements

A pavement is assumed to have failed when it can no longer provide any of its functional requirements. Pavement failures can be a result of one, or a combination of the following causes [21]: inadequate bearing capacity, frost damage, fatigue, environmental exposure and poor construction. For each pavement failure mode, there is corresponding physical evidence which develops during pavement deterioration. The physical evidence appears in four different forms: cracking, distortion, disintegration and loss of skid resistance [22].

Cracking failure is a complicated failure mode to be treated, which is caused by the repetition of traffic loading and the tensile stresses produced due to the bending of the asphalt layer, the susceptibility of binder to temperature changes as well as the increasing viscosity at low temperatures that leads to a higher stiffness making cracks appear [23]. Specially, reflective cracking is one of the most common types of cracking which is defined as cracks that are usually covered over but manage to reappear from the underlying layers onto the surface [24].

It was stated that reflective cracking can be caused as a result of traffic loading and temperature changes [25]. These factors cause the discontinuities in the underlying layers of the repaved asphalt, such as cracks or joints, to continuously move and propagate to the surface. Furthermore, traffic loading simultaneously causes tensile stresses at the bottom and shear stresses in the middle of the asphaltic overlay [26]. Also, traffic loading over transverse joints can also induce bending in the overlay. Then, environmental events such as temperature changes cause additional tensile stresses at the bottom or at the top of the overlay. As a result, when the tensile and shear stresses reach specific threshold values, reflective cracking is initiated.

Reflective cracking is a significant challenge to road engineers because if not treated early, it can grow at a rate of 1 inch per year and allow water to infiltrate through the cracks, therefore further damaging the base and the subgrade [11]. As a result,

reflective cracking can lead to premature failure of the asphalt pavements and require significant maintenance works.

2.3.1. Reflective cracking mitigation techniques

Usually, asphalt properties degrade over time through loading and climate conditions (UV rays and oxidation), and therefore, forms microcracks [10]. However, reflective cracking can appear after a short period [11] without bitumen oxidation. As explained before, reflective cracks in an asphalt layer are induced in a pavement mainly because of (i) thermal changes generating thermal contraction, when the asphalt is placed over a hydraulic bounded or concrete base and, (ii) excessive traffic loads [12]. To mitigate or delay reflective cracking in asphaltic overlays, researches have proposed different treatments such as:

- The use of a polymer-modified binder to provide a stiffer mixture, reducing the transfer of stresses, as well as to enhance bonding between layers [27].
- The use of geosynthetics, which consist of polymeric layers added placed in between the pavement layers, to reinforce them or release the stresses caused by traffic [28].
- The placement of a fibreglass grid [29] or steel-reinforcing nettings [30] as reinforcement techniques.
- The application of composite systems [31] and stress absorbing membrane interlayers [32], which work by relieving the stresses in the asphalt.
- "Strata" treatments, which consist of placing a polymer-rich dense fine aggregate mixture layer on top the damaged pavement followed by an asphalt layer [33].

- In the case of an asphalt layer over a concrete base, rubblization is another treatment that consists of transforming the concrete layer into an aggregate base to avoid the movement of the concrete layer [34].

Although all these techniques mitigated reflective cracking more or less effectively, geogrids, fibre grids and steel messes may cause problems to recycle the asphalt [35]. Other drawbacks were found, specifically, regarding to the effectiveness of the application of fibre-glass grids or "Strata" is still uncertain and implies a high cost [36]. Additionally, although rubblization presented satisfactory results, it is a treatment difficult to implement, as it requires a thick overlay and adjustments in other elements part of the road [11], [37], [38]. Regarding the application of stress absorbing membrane interlayers, they could be affected by accelerated rutting due to the interlayer [39].

Furthermore, in previous research, asphalt has been engineered to improve its self-healing properties and close reflective cracks more effectively. For example, in references [5], [6], [40], electromagnetic induction or microwaves [41]–[43] was proposed to reduce the viscosity of bitumen which, in the laboratory, closed reflective cracks in asphalt beams in up to 120 s, rather than in hours or days [44] as it happens in asphalt treated with conventional cracking mitigation techniques. Another way to increase the natural self-healing capability [45] of asphalt is the addition of encapsulated bitumen rejuvenators to the mixture [14], [16], [46], [47] which could represent a potential solution for reflective cracking as shown in Chapter 5.

2.4. Self-healing asphalts

Asphalt itself is a self-healing material, since the bitumen used in its production can flow and fill the cracks generated in the asphalt road because of traffic loads or weather conditions [4]. However, the rate of bitumen flow, hence the rate of self-healing of an asphalt pavement, depends on many factors. As asphalt ages, the

viscosity of bitumen increases due to oxidization, therefore the bitumen becomes stiffer. As a result, aged bitumen flow is very slow and inefficient, so micro-cracks start to appear between the aggregates and the bitumen. Another relevant factor that influences the viscosity of the bitumen is the temperature. Self-healing of asphalt pavements is a viscosity-driven process, which can be slowed down by low ambient temperature.

Historically, researchers have mainly proposed two ways to increase the self-healing capability in asphalt [45]: induction and microwave heating [41] and encapsulated rejuvenating agents [48], [49]. Although using the induction and microwave heating can soften the bitumen to close cracks and repair the damage, they are not a solution for the ageing of binder. To overcome the issues of asphalt ageing by induction and microwave heating, researchers have indicated the use of microcapsules containing rejuvenating agents to promote the autonomic self-healing processes inside the aged asphalt mixtures [4], [13], [46], [50].

2.4.1. Self-healing by encapsulated rejuvenators

The concept of self-healing by encapsulated rejuvenators is to deliver the healing agent to the damaged site and rejuvenate the aged bitumen in a localized way (Figure 1 represents this idea graphically). In addition, the capsules containing rejuvenators will remain inactive in the asphalt road for several years until the road starts cracking due to external damage and aging effect [48]. The cracks generated due to the traffic loads promote the release of the healing agent which contributes to close cracks in the asphalt by accelerating the self-healing property of the bitumen [51], [52]. In reference [6], it was found that the healing agent released caused a decrease in the bitumen viscosity when a load was applied over the asphalt. Due to the bitumen viscosity reduction and the load applied, the asphalt materials were compacted making the bitumen flow into the air voids and cracks.

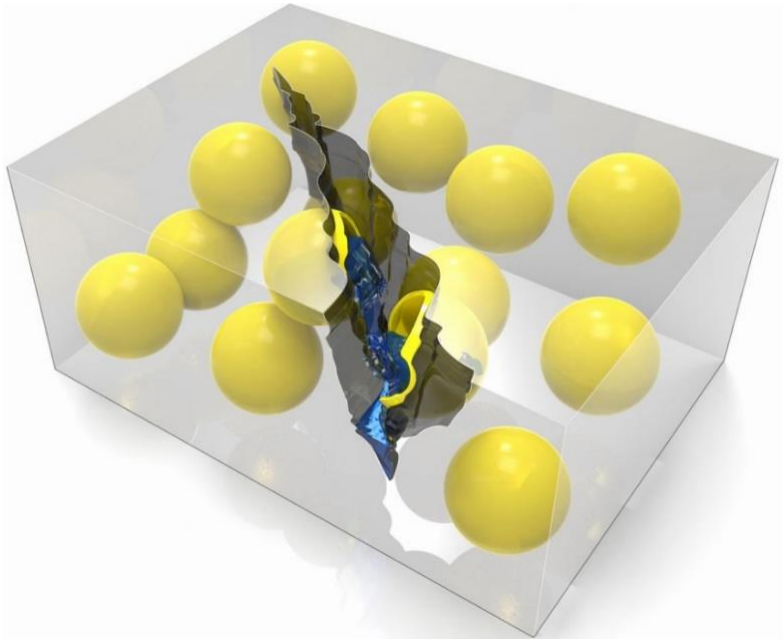


Figure 1. Capsules, embedded inside a material, breaking because of a crack formation. Extracted from [1]

The first capsules for asphalt self-healing developed [49] consisted of four parts: an organic or inorganic oil, such as soft bitumen or sunflower oil, porous sand particles of between 1-1.7mm, and a hard membrane composed of cement and epoxy. Sunflower oil encapsulated in a porous structure made of calcium and alginate (ca-alginate matrix) [48], [52], [53] is one of the most popular types of capsules that are used to improve the self-healing properties of asphalt. However, numerous encapsulation methods have been used to manufacture capsules/microcapsules for asphalt self-healing. For instance, melamine-formaldehyde (MMF) was modified by methanol to encapsulate rejuvenators [54]. The prepared capsules had an average size from 2 to 100μm, controlled by the stirring rate. Another type of capsules were the capsules based on epoxy resin [55] showing a diameter range between 7.2 and 11.4 μm [56]. Additionally, microcapsules made by emulsion polymerization method in which dimethylphenol (DMP) formed the core and urea/formaldehyde (U/F) resin made the shell [57]. It was proved that the asphalt with microcapsules had good mechanical properties. Another type of capsules with average size 50 μm

which membrane was composed of nano-$CaCO_3$ particles and methanol-modified melamine-formaldehyde were manufactured. The main drawback of these types of capsule remains in the level of toxicity of the materials used in the manufacturing process whereas alginate is safer and degradable. In addition, they need longer intervals of curation in order to reach the strength required for an optimum self-healing.

Porous sand capsules, which contains sunflower oil as the healing agent, were manufacture with a hard shell of cement and epoxy resin [58]. The average size of these capsules was 1.6 mm containing on average 20.9% of rejuvenator by the volume of the capsule. The study showed that the hard shell was in fact not necessary, and that the stiffness of the asphalt containing capsules increased by 15% after resting. Also, it was shown that the self-healing ability of asphalt was enhanced by using encapsulated rejuvenators.

Other authors [59] also explored the potential of using alginate as a method of incorporating rejuvenators into the asphalt mixtures, however by encapsulating rejuvenator in fibres and not capsules. It was found that the hollow-fibres could efficiently improve the drainage of bitumen into the cracks, so as the stiffness of dense asphalt. On the other hand, the fibres did not improve the self-healing when the asphalt was subjected to fatigue damage [60].

Finally, other types of calcium-alginate capsules have recently been assessed in asphalt mixtures [48]. These capsules were made by the ionic gelation of sodium-alginate in the presence of a calcium chloride solution. These capsules contain sunflower oil as rejuvenating agent and their sizes were around 2 millimetres. These capsules were strong enough to resist mixing and compaction of asphalt mixture and break when an external damage is applied to the asphalt pavement. Furthermore, results showed that the addition of the capsules had a positive effect on the durability and safety of asphalt mixtures and their ability to self-heal aged bitumen and rejuvenate aged asphalt mixture was proved [4], [46], [48].

2.5. Encapsulation techniques

Encapsulation technologies have always had an enormous impact on the industry. Specifically, the encapsulation of oils is a technology well-developed for several applications such as cosmetics [61], food [62], [63], textiles [64], pharmaceuticals [65], agriculture [66] and finally, construction materials such as self-healing concrete [67], [68] or asphalt [50].

There are numerous encapsulation techniques used in diverse applications. This part of the literature review evaluates the most significant and common encapsulation techniques applied in the industry. The encapsulation techniques can be classified in 3 main categories: physical/mechanical techniques, chemical techniques and physicochemical techniques.

2.5.1. Physical/Mechanical techniques

Usually, the starting materials in the physical/mechanical techniques are polymers [69]. No chemical reactions are involved. Generally, the choice of the encapsulation technique depends on the nature of the polymeric material required.

The main physical/mechanical encapsulation techniques are described in the following subsections.

2.5.1.1. Co-extrusion

Among the physical/mechanical techniques, the most used is co-extrusion because of the ease of implementation. The physical principle is based on a nozzle with two ducts and distinct liquids runs through each. The nozzle releases a liquid drop with a perfectly separated core and shell (Figure 2).

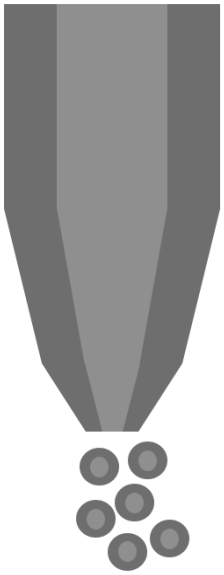


Figure 2. Encapsulation by co-extrusion

The droplets are solidified by chemical cross-linking, cooling or solvent evaporation [70].

2.5.1.2. Spray-drying

The spray-drying encapsulation technique is well-known due to its low-cost commercial process. It is mainly used for the encapsulation of fragrances and oils [69], [71]. Core material is dispersed in a polymer solution and sprayed into a hot chamber. The shell material solidifies, encapsulating the core material as the solvent evaporates so that the capsules obtained are polynuclear or multi-core. The particle size reached with this technique are mainly between 4.1 and 4.7 µm. Figure 3 shows a schematic illustration of the spray-drying encapsulation technique.

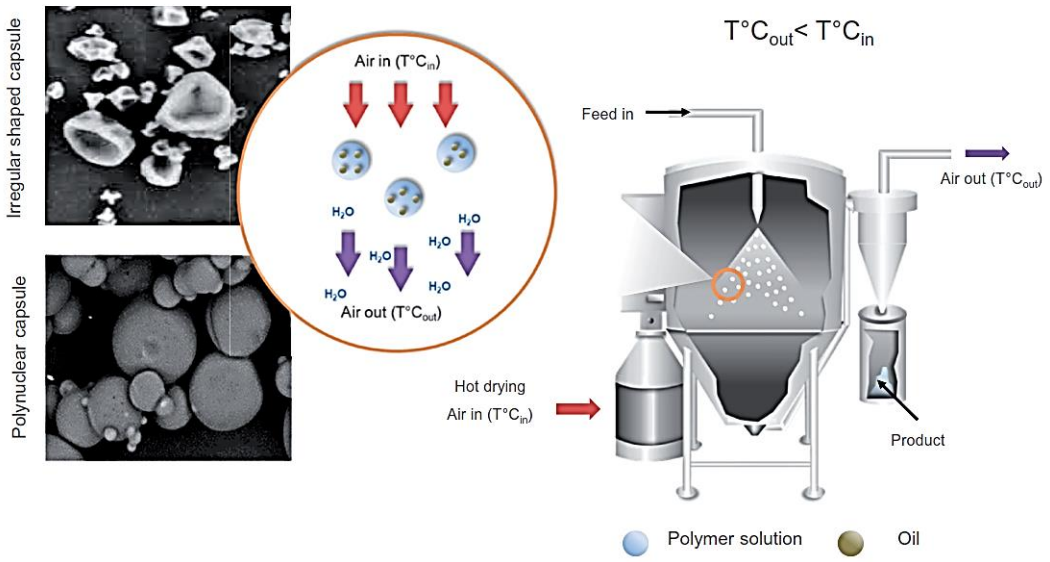


Figure 3. Schematic of spray-drying encapsulation technique (extracted from [72]*)*

2.5.2. Chemical techniques

Chemical encapsulation techniques include methods in which the starting materials are generally monomers/prepolymers. In these methods chemical reactions are involved along the capsule formation.

2.5.2.1. Polymerisation induced phase separation

The polymerisation-induced phase separation method consists of an emulsion droplet containing a dissolved monomer. After the polymerisation starts, the polymeric chains begin growing, becoming immiscible with the dispersed phase creating a polymer shell with a fluid core. This method of capsule manufacturing is very common for oil cores in an aqueous continuous phase. Figure 4 shows this technique.

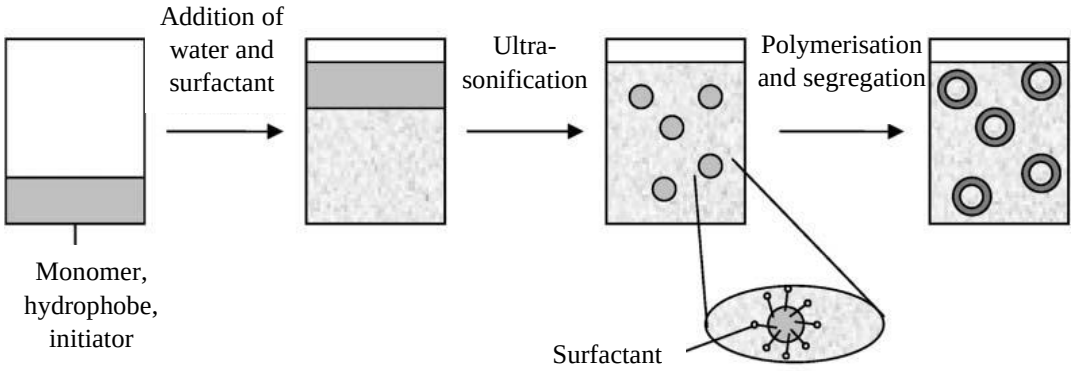


Figure 4. Polymerisation induced phase separation method (Extracted from [73]*)*

2.5.2.2. Polymerisation by solvent extraction and evaporation

The method of solvent extraction and evaporation is also broadly applied to oil-in-water emulsions. As Figure 5 shows, the polymer is completely dissolved in aqueous droplets with excess volatile solvent. When the excess of the volatile solvent evaporates, the polymer starts to precipitate and after that, polymer chains migrate to interface creating a weak shell. When the solvent is completely evaporated, the shell is completely formed with its final mechanical characteristics creating the core-shell capsules.

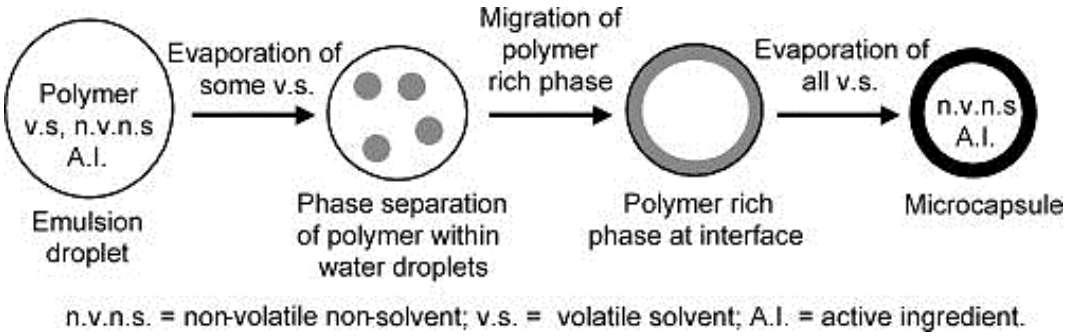


Figure 5. Aqueous core microcapsules by solvent extraction and evaporation. (Extracted from [74]*)*

2.5.2.3. Interfacial polymerisation

This technique implies two monomers and two solvents that are immiscible between them. Each monomer is dissolved in just one solvent (aqueous or organic phase). When the aqueous and organic phases contact each other, the monomers diffuse and meet at the interface. A primary membrane is created when the polymerisation starts, the polymerisation continues and, finally, the capsule is created. Figure 6 shows the different stages of the encapsulation process.

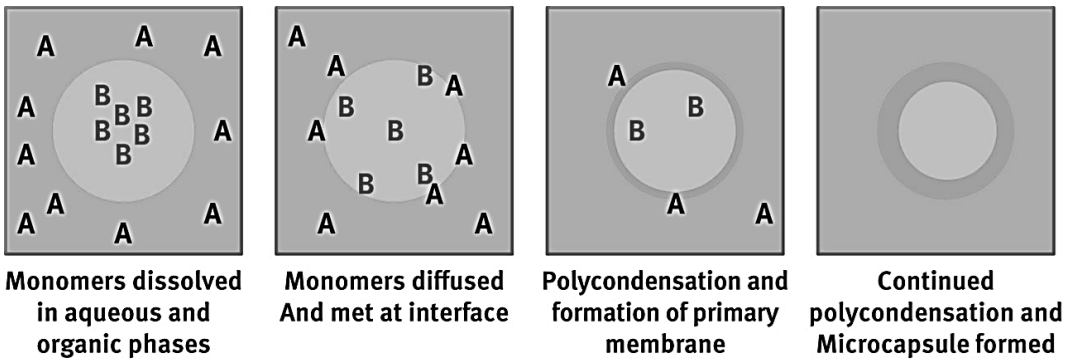


Figure 6. Interfacial polymerisation general procedure. (Modified from [75]*)*

2.5.3. Physicochemical techniques

Physicochemical encapsulation techniques include those techniques in which chemical reactions and other physical phenomena are involved along the capsule formation.

2.5.3.1. Colloidosomes

Colloidosomes are a type of capsule whose manufacturing process consists of mixing a continuous organic phase with an aqueous phase containing dispersed colloidal particles (aqueous colloidal dispersion). The basis of this type of encapsulation technique is to achieve an emulsion where the size of the emulsion

droplets formed is determined by the shear rate of a mixer. The colloidal particles migrate to the oil-water interface to create a barrier between the oil and the water stabilising the emulsion droplets. To improve the mechanical properties of the shell, the colloidosomes are re-dispersed in a fluid with similar properties to the encapsulated fluid. There is a slight variant of this method which consists of adding the colloidal particles to the organic phase at the beginning, instead of the aqueous phase. This method is described in Figure 7, extracted from [76].

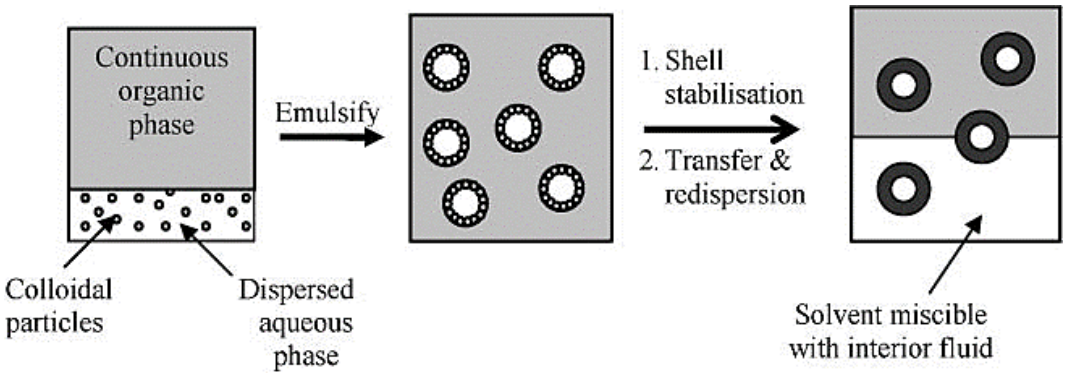


Figure 7. Fabrication method of colloidosomes

2.5.3.2. Ionic gelation

The encapsulation process based on ionic gelation is especially relevant in this literature review since, in recent years, it was an encapsulation technique performed by numerous researchers to manufacture capsules for self-healing asphalts. The most common example of this technique is the oil encapsulation in $Ca2^{+}$-alginate matrix, however, other multivalent ions, such as Al^{+3} or Ba^{2+}, can be used for promoting the polymerisation of alginate (in this case) or another polyelectrolyte able to start the polymerisation rapidly in contact with those multivalent ions [77]. The capsules manufactured by the ionic gelation have been extensively applied to self-healing asphalts obtaining excellent results [52], [53], [78], [79].

As Figure 8 shows, the ionic gelation can be categorised in three distinct groups depending on the way the multivalent ion reaches the alginate chains: (A) external, (B) internal and (C) inverse gelation.

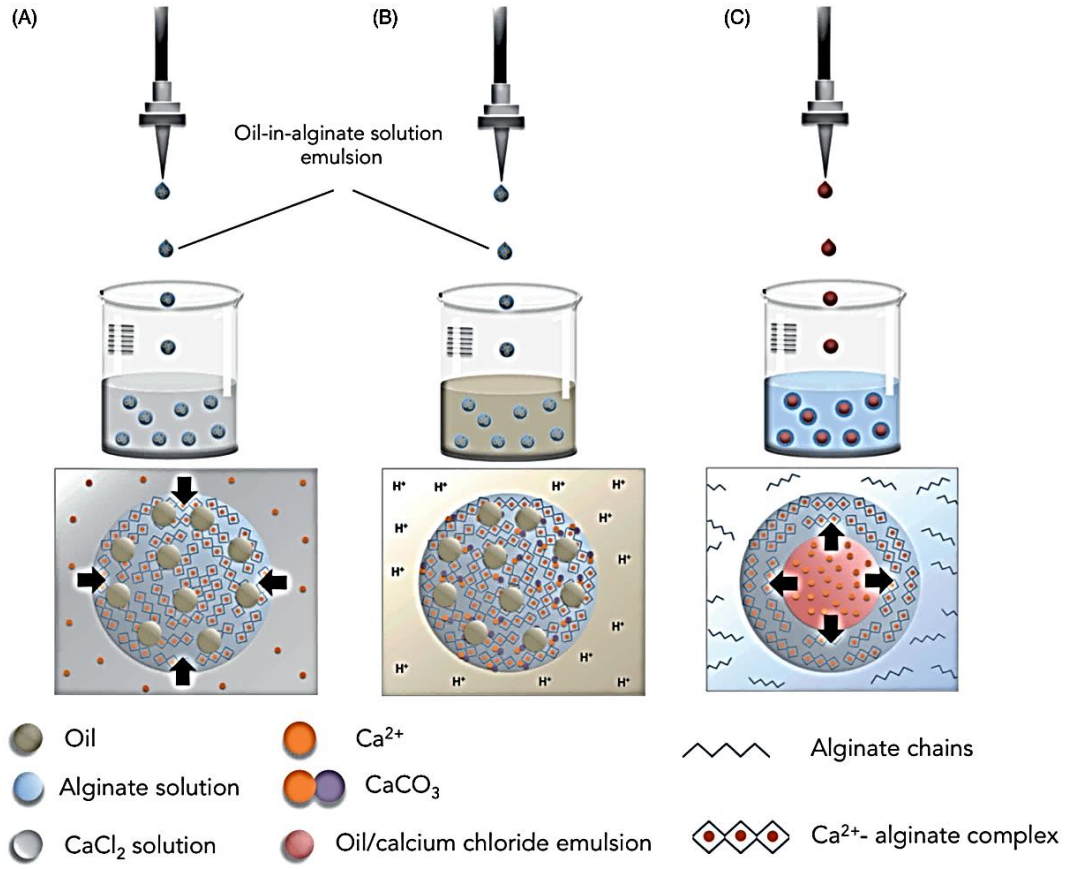


Figure 8. Graphical representation of oil encapsulation by (a) external gelation, (b) internal gelation or (c) inverse gelation techniques. (Extracted from [72]*)*

The external gelation (Figure 8(a)) involves the addition of an oil and sodium alginate emulsion to a calcium chloride solution. Capsules are formed by dropping the oil and sodium alginate emulsion into the calcium chloride solution by means of a syringe and pump. When the emulsion drop is inside the cross-linker solution ($CaCl_2$), the Ca_2^+ ions migrate from the solution to inside to the capsules giving oil multicore capsules as a result. During the dropping process, the calcium chloride solution with the capsules is vigorously agitated by a magnetic stirrer. The size of

the capsules is mainly regulated by the diameter of the nozzle or syringe from where the drops of oil and alginate emulsion are let into the calcium chloride solution. The mechanical properties of capsules are highly influenced by the amount of time they are in the calcium chloride solution and by the level of concentration of this solution.

The resultant capsules manufactured from external ionic gelation are similar in terms of internal structure to the resultant capsules obtained by the internal ionic gelation technique. However, the last ones have a higher level of porosity. This increment in the porosity is because the oil and alginate emulsion also has $CaCO_3$ that is insoluble in water. The significant difference between both techniques is the solution where the drops fall and the reaction takes place. A solution of acetic acid and oil is used in an internal gelation encapsulation, where the ions H^+ coming from acetic acid dissociation migrate to the emulsion drops and react with $CaCO_3$ [72].

$$CaCO_3 + 2H^+ \rightarrow H_2O + CO_2 + Ca_2^+ \quad (1)$$

After obtaining the Ca_2^+ ions inside the emulsion drops, the process is the same as internal gelation, cross-linking alginate chains and resulting in multicore capsules.

Finally, the capsules obtained by inverse gelation or reverse spherification [80] are completely different from the previous ones. These capsules are liquid core-shell type having the core and shell well-differentiated. The production process of this type of capsule consists of adding a calcium chloride and oil emulsion drop by drop into a solution of alginate. The Ca_2^+ ions migrate from the emulsion drop to the alginate chains starting the cross-linking process, and therefore, a membrane is formed containing an oil core [81]. The membrane formed is less dense in the external part of the capsule due to the Ca_2^+ migration from the centre to the outside. To avoid this, the capsules are immersed in a calcium chloride solution where the capsule membrane formation is completely finished. As might be expected, some studies [82] demonstrated that the mechanical properties of this type of capsule are influenced by the concentration of sodium alginate, calcium chloride solution and the gelation time, which is the period of contact between the calcium chloride and

the oil and alginate emulsion and alginate solution. The higher these concentrations are, or the longer the curing time is, the thicker the membrane will be [83]. This procedure is a novel and innovative technique that had not previously been greatly developed. Recently, the inverse gelation technique has been applied in diverse industries such as pharmaceutical [84] or the food industry [85].

2.6. Capsule characterization

The performance needed in the final applications of the capsules determines the significance of their characteristics. To give an example, there are applications where it is required that capsules break in the exact moment under determined strain. In the case of self-healing asphalts, this is a crucial parameter, however, the capsule breakage is not always needed to release the internal rejuvenator. There are capsules that release the liquid phase contained by the solid matrix by porous diffusion. In this case, in contrast to core-shell capsules, parameters such as the diffusion rate of the liquid phase through the porous solid matrix and the load applied over the capsules are more influential. On the other hand, the mechanical strength of the capsule also depends on the solid matrix structure and thickness, as well as the diffusion rate. For this reason, it is believed that different parameters can influence the capsule optimisation in different ways depending on the type of capsule.

Usually, the characterisation of microcapsules techniques is categorised into three groups: physicochemical, structural and mechanical properties [86].

Table 1 summarises the numerous techniques for the characterisation of capsules. The information gathered is divided into the type of property, the specific property analysed, the techniques used and some descriptive and significant data of these techniques.

Table 1. Capsule characterisation methods

Type	Properties	Characterisation methods	Description
Physicochemical	Size and size distribution	DLS (Dynamic light scattering)	• Used for Brownian motion in liquids • Capsule size (1 nm to 1μ)
		Laser diffraction	• For capsule suspension • Average size and size distribution • Capsule size (10 nm to 3 mm) • Refractive index of the shell material needed.
		Microscopy (SEM)	• True image of the capsule in 2D and 3D • For Morphology • Easy but time-consuming method • Capsule size (50 μm to 3000 μm)
	Surface roughness and morphology	Atomic Force Microscopy (AFM)	• Compression test with a normal force • Surface morphology
	Chemical composition	Attenuated Total Reflectance Fourier-Transform Infrared (ATR-FTIR) spectroscopy	• Very little sample preparation and faster • Information about functional groups of membrane until 1μm
		X-ray photoelectron spectroscopy (XPS)	• Qualitative information about surface chemical groups until 100 nm
		Time of flight secondary-ion mass spectrometry (ToF-SIMS)	• Surface information for low depth of penetration (1- 2 nm)
	Surface charge and zeta potential	Streaming potential technique and electrophoresis	• Streaming potential technique for capsules around 30 μm and electrophoresis for capsules larger than 30 μm

Structural	Shell thickness	Microscopy (SEM) and Transmission electron microscopy (TEM)	• Complex sample preparation • Time-consuming post process
		Focused Ion Beam (FIB)	• Invasive process which destroys the samples • It can be combined with SEM
	Pore size	X-ray micro-computed tomography	• Non-destructive technique • Sum of individual cross-sectional slices • Three-dimensional image • Complete structure image of a capsule
	Crystallinity	X-ray diffraction (XRD)	• Degree of crystallinity • Type of materials for amorphous phase
		Differential scanning calorimetry (DSC) and thermo-gravimetric analysis (TGA)	• Glass-transition temperature and melting point are related to the crystallinity degree
	Release of core material	Application of loads	• Strong agitation of capsules inside a liquid medium and the measure of concentration of liquid
Mechanical	Singles capsules	Pressure probe	• Internal pressure manipulation • Volumetric elastic modulus
		Micropipette aspiration	• Capsule diameter (1-10 μm) • Poisson ratio
		Cell poking and atomic force microscopy (AFM)	• Young´s modulus • Small forces measured
		Optical trapping	• Very sensitive method • Very small scale

Diametrical compression	• Very small forces • The capsule is broken • Force-deformation curves • Forces relatively higher • Scale relatively larger

2.6.1. Physicochemical methods

The size and size distribution are properties that can vary depending on the capsule manufacturing method. The capsules produced by means of microfluidics (syringe extrusion) are usually smaller and they have very a narrow size distribution. On the other hand, the capsules produced in a stirred vessel are usually bigger and they have a wider size distribution.

The three methods most commonly used to determine the size and size distribution are: Dynamic Light Scattering (DLS), Scanning Electron Microscopy (SEM) and laser diffraction. DLS is focused on determining capsule size and size distribution for diameters between 1 nm and 1 μm. DLS sample preparation is a complex process which involves a very time-consuming analysis. On the contrary, SEM (Figure 9) is one of the simplest methods regarding the specimen preparation, so it is quicker than the DLS technique. SEM can generate an image with high magnification (>100000x) and it is more commonly used to measure the capsule size than the size distribution. Additionally, SEM offers the possibility of building 3D images from the 2D images obtained by the microscopy. The application range of this technique is for capsules with diameters between 50 and 3000 μm. The main drawback of SEM is the inability to measure the size and size distribution when the samples are black, reflective or transparent, because it uses the refracted light to determine them. Finally, the laser diffraction methods are based on light passing through a suspension of capsules which means it is necessary to know the refractive index of the shell material. The application range is from 10 nm to 3mm in capsule diameter.

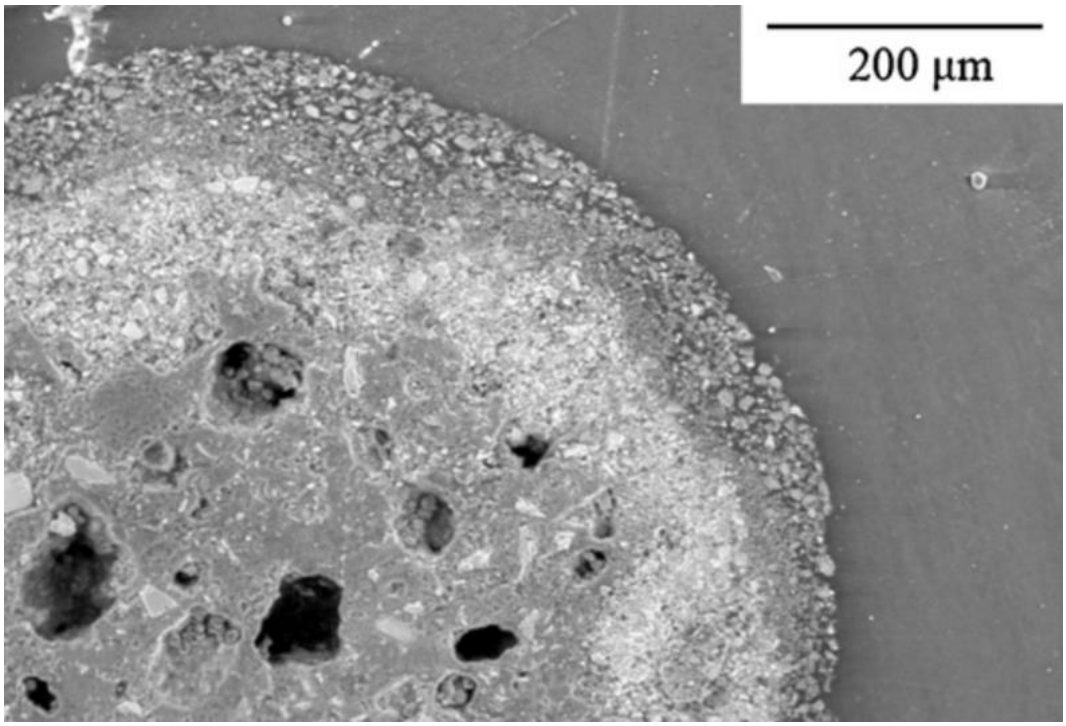


Figure 9. SEM image of a capsule section showing its different layers. (Modified from [50])

2.6.2. Structural methods

The sophistication of the requirements demanded by new final applications is increasing the complexity of the internal structure of the capsules. For instance, there are capsules in which two types of layers are required. This characteristic is common in applications where the internal liquid release needs to be controlled, where capsules have two liquid phases or where they have a very porous internal structure with a significant presence of microchannels.

It is believed that pore size is directly related to other mechanical properties of the capsules such as capsule strength. X-ray computed tomography has been extensively used to examine the inner structure of many types of capsules and for different scales. Figure 10 shows examples of computed tomography scans for 4 different capsules faithfully reproducing the internal structure of the capsule. X-Ray Computed tomography X-Ray is based on the illumination of the capsules by X-ray

and collection of the projection images by an X-ray detector, creating a cross-section of the capsule. This procedure is repeated many times, taking many images of cross sections for different depths while the capsule is rotating on a platform. Finally, computer software merges all the images into one, obtaining a complete three-dimensional image of a capsule.

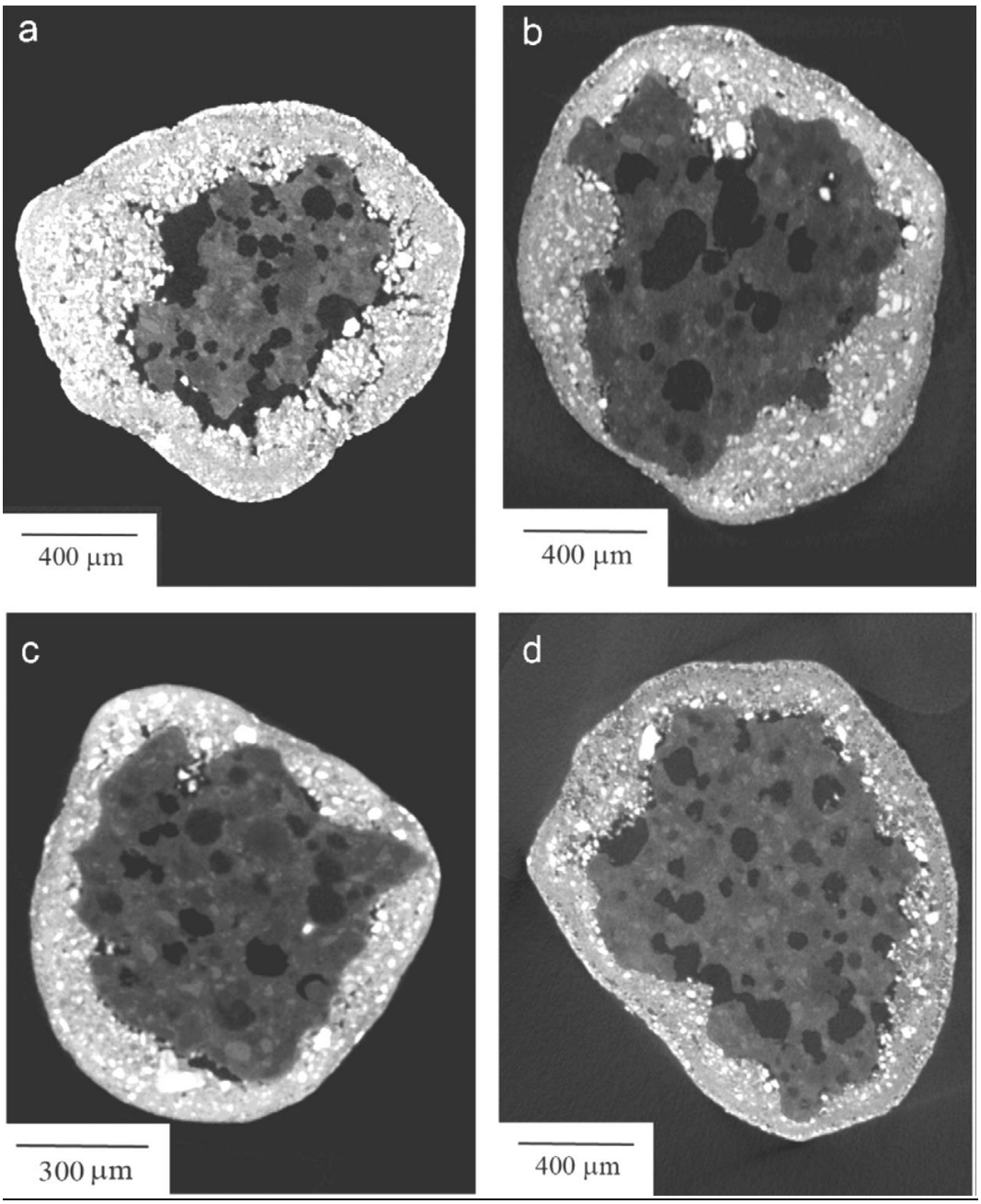


Figure 10. CT-Scan images of different capsules. (Extracted from [79]*)*

2.6.3. Mechanical characterisation

Mechanical characterisation is essential to understanding the capsules' behaviour during their application and use. The mechanical characterisation of microcapsules is usually determined by measuring their deformation under a known mechanical load, allowing key parameters to be calculated for the capsule design such as elastic modulus, yield stress or failure/strain which are crucial to determine if the capsules are suitable for the final applications [87].

The most common techniques to measure the mechanical properties are atomic forces microscopy (AFM) and compression testing. These techniques are based on analysing the forces that cause deformations of capsules and developing theoretical models. In this way, stress-strain relationships and the parameters of their mechanical properties/the mechanical properties of the capsules can be determined [88].

The mechanical characterisation can be mainly divided into elastic regime, plasticity, rupture force and time-dependent effects like viscoelasticity. Figure 11 shows the capsule deformation depending on the type of the mechanical test:

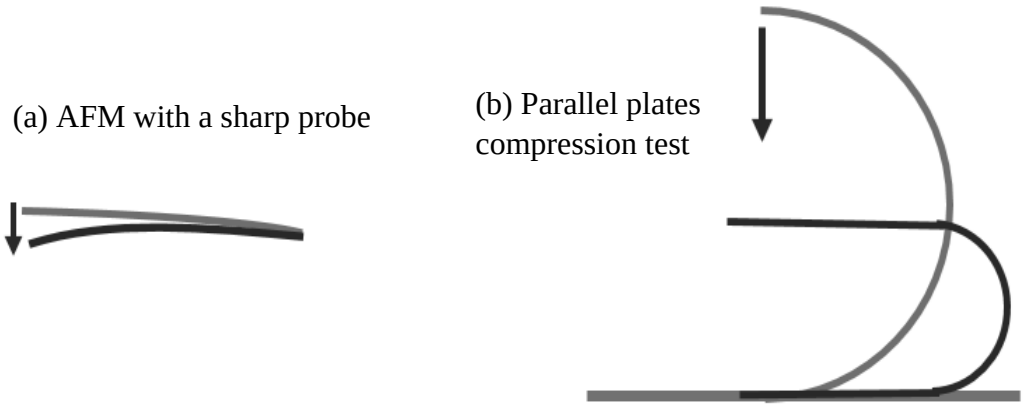


Figure 11. Membrane reactions for mechanical characterisation tests

When rupture occurs using a sharp indenter AFM, only the area which is in contact with the tip is tested, whereas using parallel or diametrical plates, many more ruptures occur in all areas of the capsule, with less stress for each rupture.

AFM with a sharp probe provides data related to failure properties of the membrane at the contact point while compression testing such as parallel plates compression tests provide more information about weak spots of the capsule shell [89]. Both failure types can take place in a real scenario. However, parallel plates compression test is considered to be more realistic in a practical situation of a capsule being embedded inside the asphalt and supported from all sides. There are two main classes of capsule ruptures, ruptures within or close to the elastic regime and ruptures far from it. The first type means a brittle failure while the second one means a ductile failure. Normally, if the capsule breaks close to the elastic regime, the deformation will be very small. On the other hand, there is another type of capsule which breaks after a large deformation in the plasticity zone.

Regarding the capsule manufacturing for self-healing asphalts, the parallel plates compression test obtains more decisive results since it shows the capsule behaviour when it is embedded in the asphalt where the traffic loads usually affect the entire capsule.

The output obtained by means of these techniques are the rupture force (F_B) and the fractional deformation at rupture (ϵ_B). Normally, the fractional deformation at rupture (ϵ_B) is independent of capsule size, medium, osmolality and compression rate, and therefore, the linear increase of compression force and rupture force with the diameter for a given deformation is observed. As it can be observed in Figure 12 [90], it was demonstrated that the rupture force is also linearly related to the wall thickness (in this case capsules with a shell of Silica-shell/oil-core).

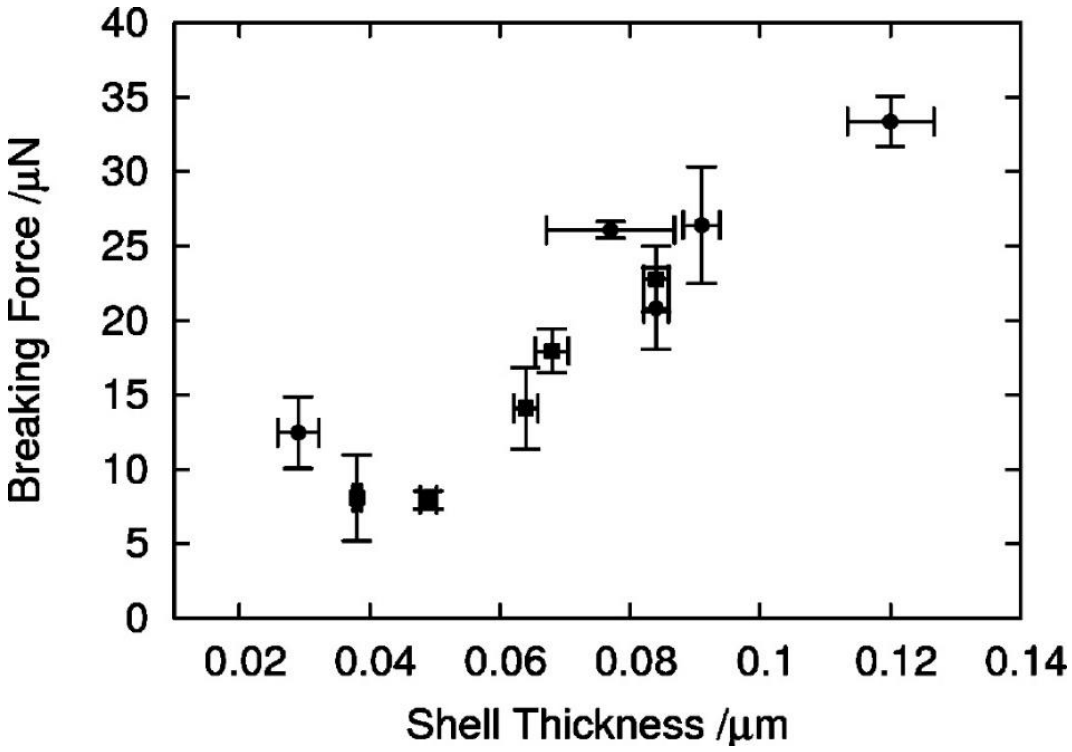


Figure 12. Breaking force as a function of shell thickness of capsules. (Extracted from [91])

Additionally, it was demonstrated that the proportions during the shell formation stage is a key factor in the thickness of the wall and therefore, in the F_B and the ϵ_B [91].

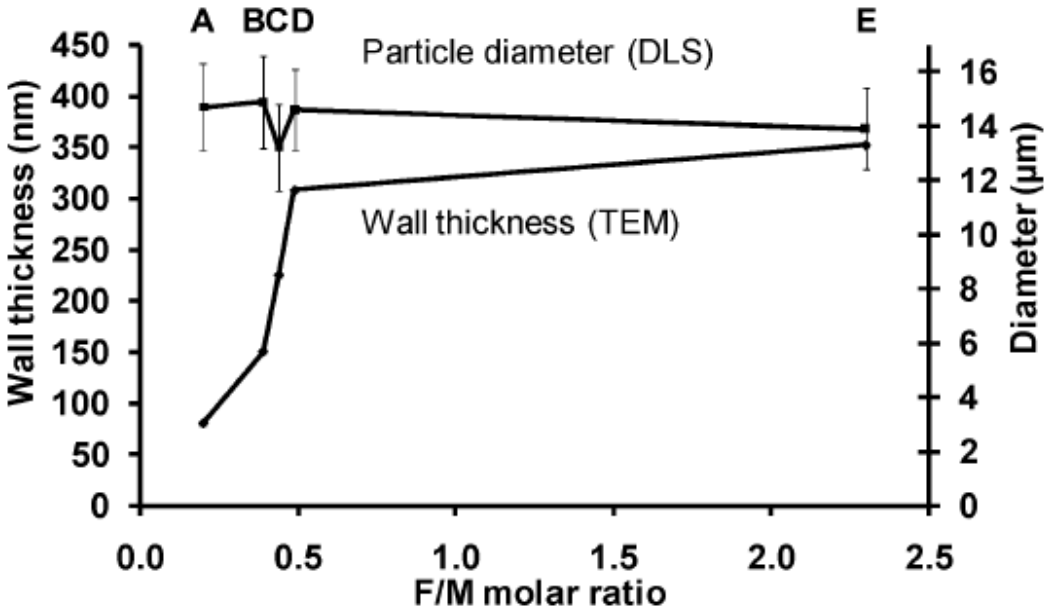


Figure 13. Relation between diameter and wall thickness vs. molar ratio. (Extracted from [91])

Figure 13 shows that whereas the particle diameter does not change significantly regarding the F/M (Formaldehyde/melamine are components of the shell) molar ratio, the shell thickness is strongly influenced by the F/M molar ratio. This example shows that there can be types of capsules where the molar ratio of shell components is determinant to reproduce the same wall thickness and therefore, the mechanical properties for all the capsules. When the molar ratios are low, a small change in the molar ratio of the shell components means a huge change in the shell thickness.

2.6.3.1. Parallel plates compression test or diametrical compression test

The basis of this technique is the compression of a capsule by means of two parallel plates until it breaks. During the test, the force applied by the plates over the capsule is measured and recorded. At the same time, the gap between the plates is measured, obtaining the displacement. The force-deformation data allows to calculate several

parameters such as Young's Modulus, which is directly related to capsule mechanical properties. This compression test can be varied to carry out numerous experiments. For example, compression at different speeds, repeated compression, loading and unloading and compression until fracture.

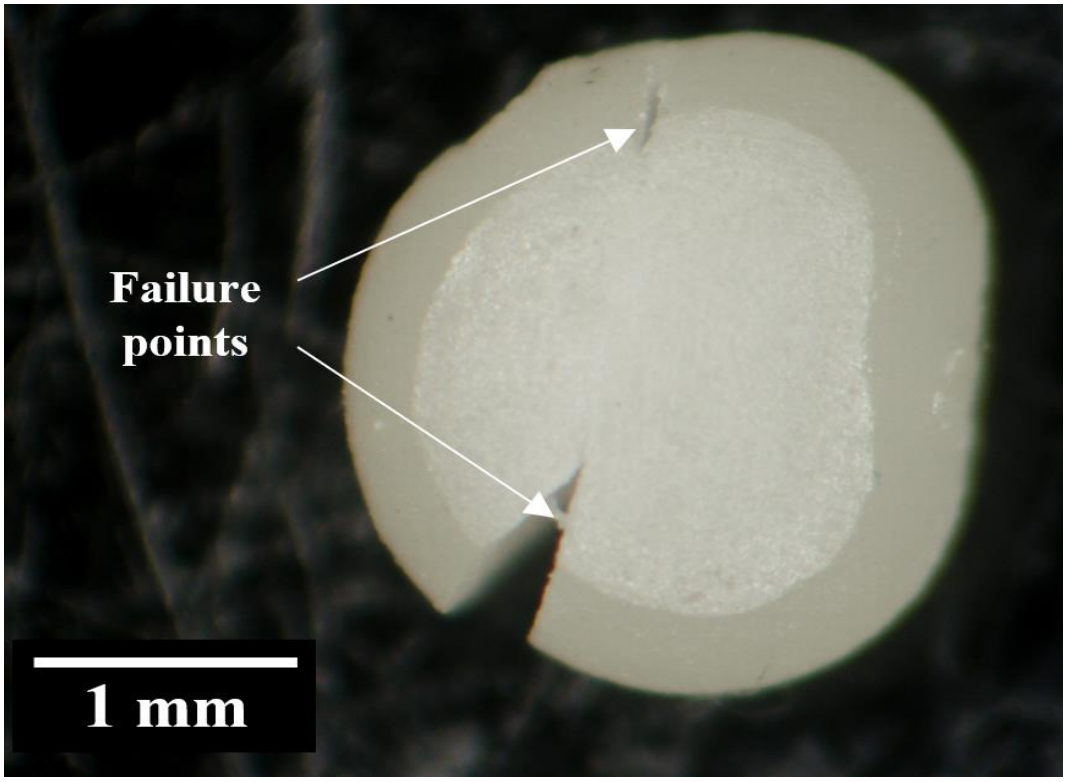


Figure 14. Example of a broken capsule after parallel compression test. (Extracted from [53])

Figure 14 shows the resultant capsule squeezed until failure by the parallel plates compression test. The failure points can be seen in the capsule as result of the pressure applied.

Finally, Figure 15 shows the Force-Displacement output directly obtained from a parallel plate compression test performed at three different temperatures for a calcium-alginate capsule containing sunflower oil.

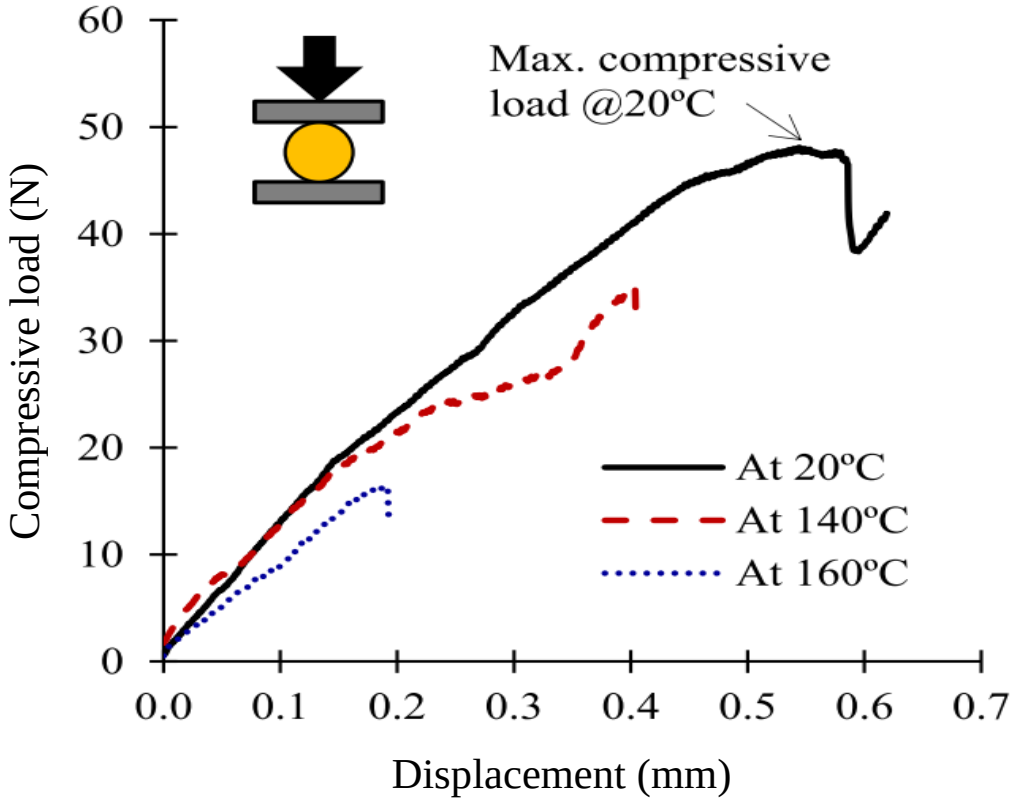


Figure 15. Compressive load vs. Displacement plot for one type of capsules and for temperatures. (Extracted from [53])

2.7. Release mechanism

Generally, the material contained inside a capsule is in the liquid phase. The release mechanisms for any type of capsule are divided into two categories. Depending on the type of changes needed to make the solid matrix or shell release the liquid, the mechanisms can be grouped by chemical stimulus, where the chemical reaction is caused by an external factor, or physical stimulus, where the liquid release is promoted by an increment in the internal pressure of the capsule. An increment of the internal pressure can generate either the capsule breakage or the internal liquid diffusion through the porous matrix. It is believed that the release mechanisms of Ca-alginate capsules containing oil, which are commonly used in self-healing

asphalts (Figure 16), follow both principles. Therefore, the amount of oil released should also be strongly influenced by the level of pressure that the capsule receives before its breakage occurs.

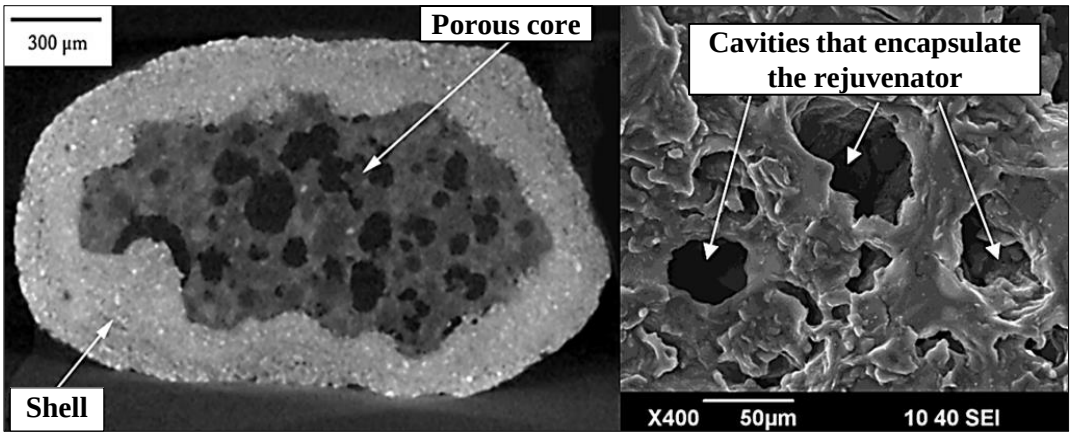


Figure 16. Internal structure of catsand capsules (Left) and Ca-alginate capsules manufactured by internal ionic gelation (Right).

However, capsules produced by an inverse alginate gelation have a core-shell structure (Figure 17) and the release of the liquid core takes place because of the membrane breakage [92]. Shell thickness is the main parameter which governs the internal liquid release.

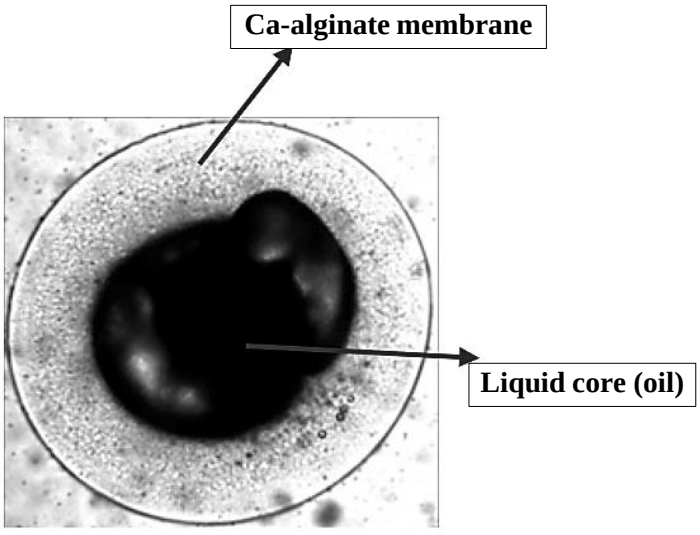


Figure 17. Internal structure for capsules manufactured by inverse ionic gelation. (Modified from [83])

Although the external pressure is the most common stimulus for the release of rejuvenators in capsules for self-healing asphalts, there are many other types of stimulus in other applications such as biological agents, chemical agents, sunlight, temperature, electricity or magnetic agents [93]. The release mechanisms can also differ from the shell breakage due to an external pressure. Dissolution of the capsule shell [94], the presence of a shell with selective permeability [95], the increment of the internal pressure by swelling [96] and stimulation of the shell by external conditions such as pH, ionic strength, light and temperature [97] are other examples of how capsules can release the internal liquid phase.

2.8. Numerical modelling to simulate fluid-solid interactions and solid breakage in capsules

Numerical simulation provides an alternative tool for scientific investigation, instead of carrying out expensive, time-consuming or even dangerous experiments in laboratories. Furthermore, numerical simulation usually provides more information about variables that cannot be analysed by means of scientific experiments otherwise. For this reason, numerical modelling is considered as an important tool in the design of new materials due to the ability of prediction of the material behaviour against potential stimulus. Figure 18 [98] shows why numerical simulation is playing an increasingly important role in scientific investigations.

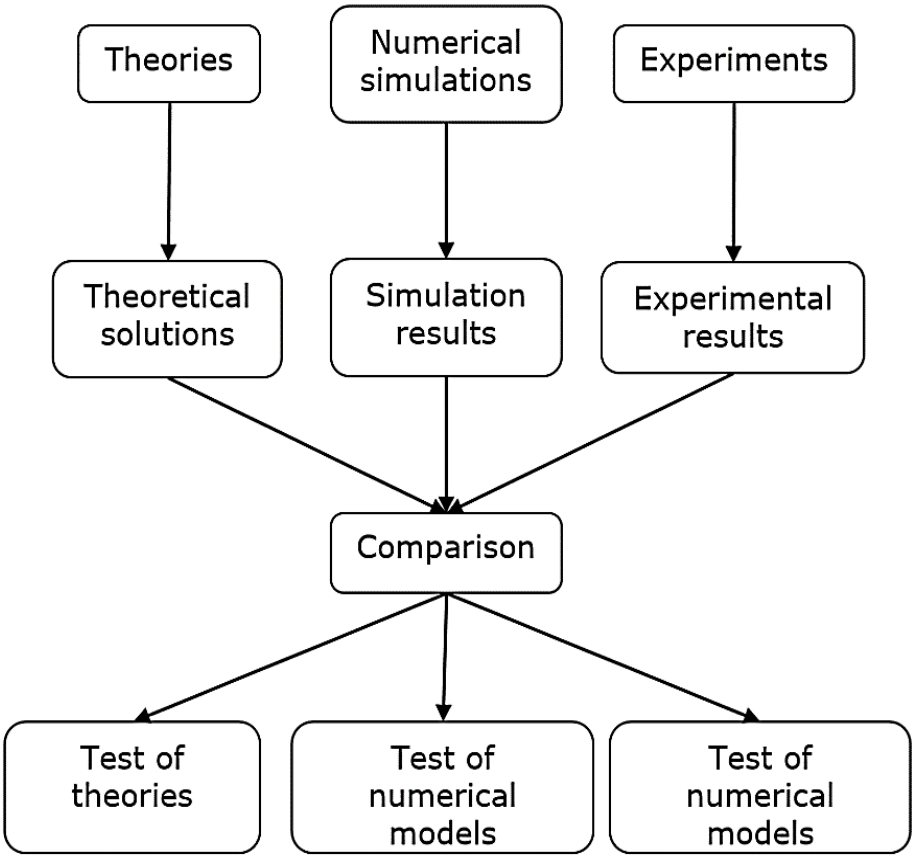


Figure 18. Connection between the numerical simulations, theories, and experiments

2.8.1. Mesh-free models

Although technological developments have provided society with powerful computers in recent years, the conventional mesh numerical simulation is limited by different aspects such as time-consumption or data storage, which are difficult problems to solve maintaining the numerical model used. The most important mesh numerical simulation is the Finite Element Method (FEM), which is based on the division of complicated shapes into smaller elements; these elements are called finite elements. Until now, most problems related to engineering were solved by using FEM because of the high capabilities of commercial software and the developed knowledge of applying this method to solids and structures [99]. However, the complexity of new engineering problems starts to limit the use of this

type of computational method. The necessary mesh creation for FEM methods may become the most time-consuming process before starting the simulation. Additionally, a small error in the mesh creation will strongly condition the result of simulation, specifically for complex three-dimensional domains.

To overcome these barriers, new numerical methodologies have been developed in recent years such as Mesh-free (or Meshless) models. A Mesh-free method is a a computational technique used to establish system algebraic equations for the whole problem domain without the use of a predefined mesh for domain discretisation [100].

The Mesh-free models show important advantages regarding conventional mesh numerical simulation. Some of these advantages regarding conventional mesh numerical methods are mentioned in the following list [101]:

- No need for elements in the gaps between nodes
- No need to define the connectivity between nodes to obtain the discrete equations
- No need to redefine the mesh or the connectivity between nodes in intermediate stages of the process to achieve the final solution
- Able to simulate crack propagation
- Able to monitor fluid particles
- Able to simulate big deformations
- Able to simulate phase changes

The emerging mesh-free particle methods (MPMs) offer computationally efficient alternatives to solve the problems encountered by the Finite Element Models (FEMs) [102]. One of these problems is found in dynamic common computer vision problems such as a segmentation and motion analysis. The accuracy and efficiency of FEM decrease when the mesh geometry is extremely skewed or compressed. To avoid these problems, geometry re-meshing can be carried out [103]**.** However, for large three-dimensional problems or situations where a high definition is needed,

the computational cost of re-meshing at each step is too expensive, and therefore, the simulation is slowed down.

A mesh-free particle method (MPM) in general refers to the class of mesh-free methods that employ a finite set of discrete particles to represent the state of a system and to record the movement of the system. The advantages of mesh-free particle methods are the following [100]**:**

- Very large deformations can be simulated accurately because their computation involves the connectivity among the nodes, and hence, it can change with time.
- They are able to model damage of the components, such as the fracture.
- It is a highly accurate model as it is a simple task to add nodes in areas where more refinement is needed.
- Complex geometric object shapes can be achieved accurately with mesh-free discretisation.

2.8.1. Solid-Fluid interactions

The solid-fluid interactions are found when the simulation includes one or more solid structures interacting with an internal or surrounding fluid flow. Several models based on meshing used in the past are mainly divided into two groups [104]: Conforming-mesh methods and non-conforming methods.

As can be observed in Figure 19, when applying the conforming mesh methods the interface conditions are represented as physical boundary conditions, therefore re-meshing is needed if the solid deformation or movement are simulated. On the other hand, when applying the non-conforming mesh methods [105], the boundaries are defined as constraints in the fluid and solid equations systems and they are solved independently, therefore re-meshing is not necessary. Finally, Figure 19(c) shows a

solid-fluid simulation by applying a mesh-free particle-based method. This method calculates one by one all of the interactions among all types of particle.

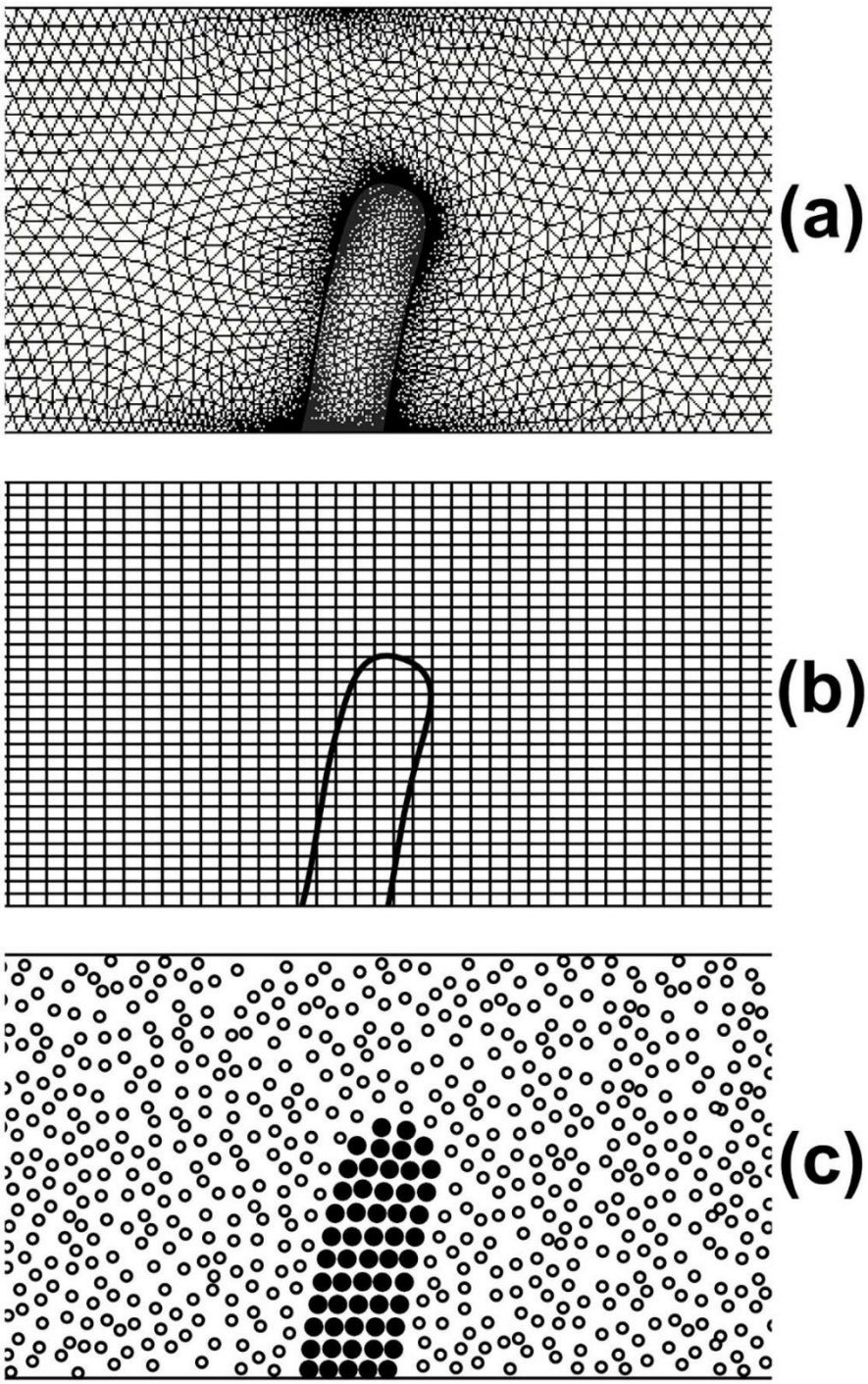


Figure 19. (a) Conforming mesh, (b) Non-conforming mesh and (c) Mesh-free. (Extracted from [107])

The solid-fluid interaction is another drawback of FEM. Although some scientific studies [107] presented a simulated method of fluid-solid interactions based on coupling Smoothed Particle Hydrodynamics (SPH) and FEM and notable results were obtained, it would be extremely difficult to simulate other physical phenomena with that approach. Many other computational techniques have been used for simulating solid-fluid flows, some of them are Computational Fluid Dynamics (CFD), Lattice-Boltzmann (LB) and Boundary Integral Methods (BIM). However, none of them were able to simulate breakable particles. The MPM models present the possibility of reproducing the breakable particles in an accurate way. As an example [108], a multiphysics method based on the SPH method was applied to simulate a biofilm evolution and predict it spatially and temporally. The biofilm growth is driven by a biological reaction and the diffusion of nutrients can be analysed. Additionally, the fluid flow forces can cause deformations and erosion in the biofilm as deformable solid. Figure 20 represents these processes. The blue particles represent the fluid particles which contact the biofilm surface and start to erode the interface biofilm particles (shown in red), however at the same time the solid particles (shown in black) start to become interface biofilm particles. Therefore, both phenomena, biofilm erosion and biofilm growth, can be assessed by the simulation.

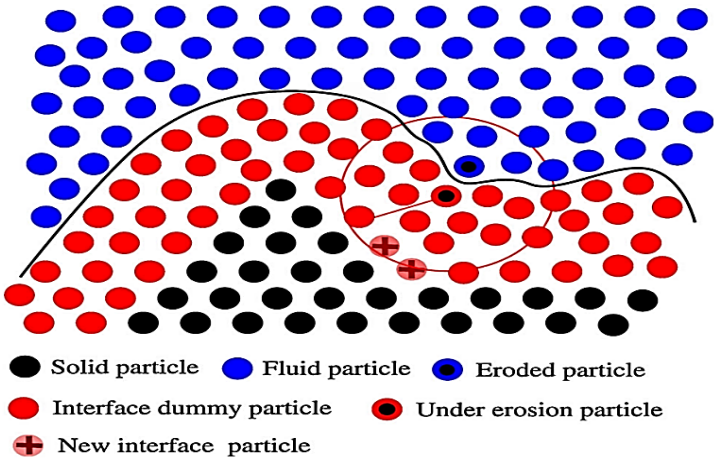


Figure 20. Computational simulation of interface modification due to erosion. (Extracted from [109])

An hybrid model to simulate solid-fluid interactions, coupling Discrete Element Method (DEM) and Smoothed Particle Hydrodynamics (SPH), was used to reproduce the hydrofracturing. Soil solid particles were represented by DEM particles while the liquid was represented by SPH particles. Through this work, hydrofracturing simulations demonstrated the relation between liquid viscosity and the crack formation. The lower the viscosity is, the faster the crack propagates and the wider the crack is [109]. Figure 21 shows three frames of the simulation of soil hydrofracturing due to the water action.

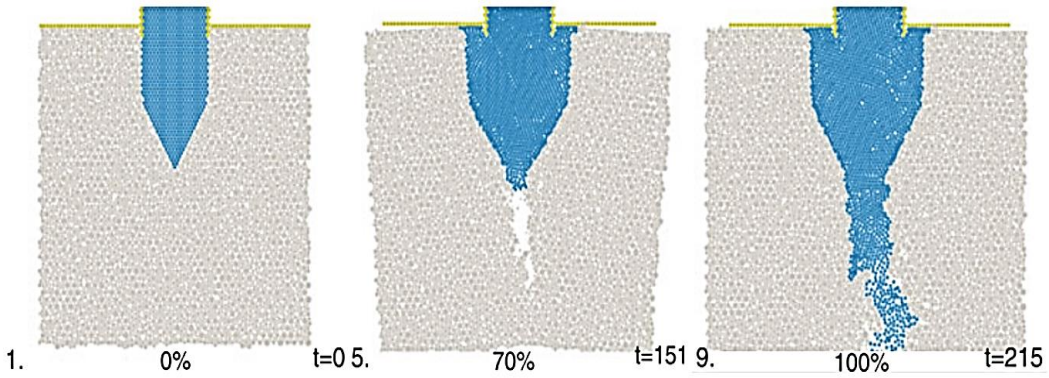


Figure 21. Frames of crack evolution simulation because of hydrofracturing. (Extracted from [110])

The SPH model has also been applied to represent both types of particles (solids and fluid). The SPH model was applied to simulate processes like melting and solidification, which include liquids and deformable or rigid solids [110]. Applying just SPH as the numerical model, it was not necessary to define a common framework for both models. Besides the solid-fluid interactions, three-dimensional simulations were carried out to accurately replicate the surface tension on water and, in this way, to model the interactions between immiscible liquids [110]. Furthermore, this model presents the capability of simulating the mixing of two or more types of liquids applying similar inter-particle potential function to both.

Fluid-fluid interaction were successfully simulated in processes like boiling water, and hence, gas-liquid interactions, diffusion of partially miscible liquids, phase

changes and interactions between completely immiscible liquids [111]. The particle-based mesh-free software model SPH was applied to simulate the immiscibility between liquids. These examples showed the great importance of the SPH model for the computational simulation of the behaviour of fluids.

Finally, a mesh-free approach based on SPH model was proposed to simulate liquid-solid interactions in 3D porous media [112]. Computational Tomography technology is the key factor in this work. The 3D geometry of the porous system is obtained by the CT-Scan images accurately representing the internal connectivity between different pores. This scientific work gives us the possibility of creating the internal geometry of porous capsules by applying Computational Tomography technologies. At the same time, the Smoothed Particle Hydrodynamics model could be implemented to simulate the rejuvenator release from the capsule core through the porous shell of the capsules. This also opens more possibilities such as the simulation of porous asphalt with capsules for self-healing and numerous applications in many other research fields.

2.8.2. Deformable and breakable solids

FEM does not allow highly accurate simulations of large deformations, much less the simulation of breakable solids in contrast to multiphysics mesh-free models [113]. This limitation is very significant for many industrial processes.

There are some scientific studies based on Finite Element Method (FEM), which modelled the fluid-solid interactions and even the deformation of solids. As in example, the interaction of a microcapsule and the external liquid flow was analysed by coupling FEM and a boundary integral method to solve the Stokes flows [114]. Although large deformations were accurately modelled, the fracture of solids is a pending issue for this type of approach. For this reason, many other solutions were developed, the main solution being to use the mesh-free particle methods for these purposes. One of the models proposed was the Material Point Method, which is able

to simulate fractures in solids. The issue with the Material Point Method is the need to define a pre-fracture [115], meaning there is no prediction of the fracture since where it appears is predefined before the simulation starts. Similar methodology is followed where the Meshless Local Petrov-Galerkin (MLPG) method is proposed to simulate the fracture of brittle solids [116]. The solids are treated as completely rigid bodies, and for this reason, it is also necessary to generate the fractured fragments by means of a damage-based fracture model, defining the particles as damaged or not depending on their state in the simulation. Figure 22 represents an example of a simulation of a brittle object by MLPG model.

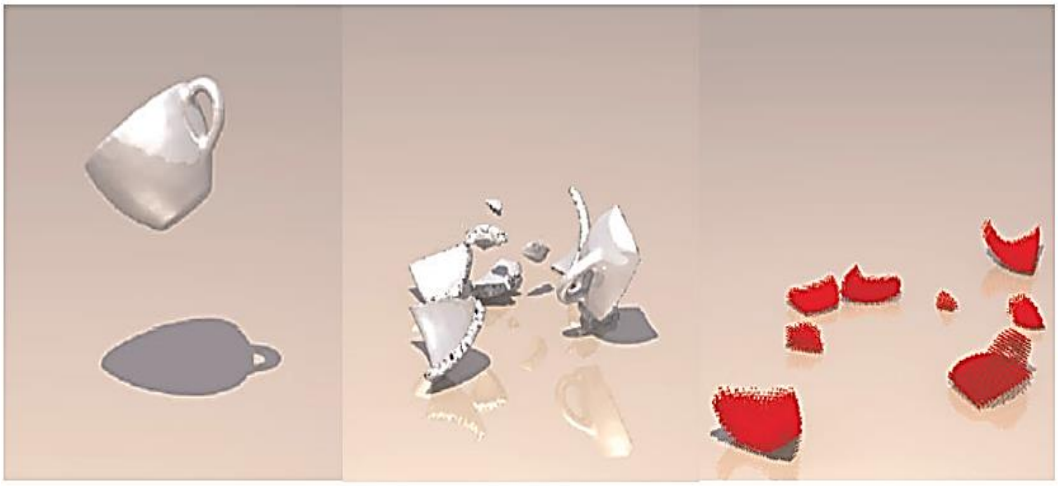


Figure 22. Simulation of a coffee cup hitting the ground and breaking into pieces. Meshless Local Petrov-Galerkin (MLPG) model applied. (Extracted from[117])

On the other hand, another different but still mesh-free approach was implemented [117] to demonstrate how coupling several meshfree particle methods (DEM and SPH) could become a very relevant numerical simulation tool for designing structures. They simulated the behaviour of breakable granite material under pressure. In this case, the DEM particles are connected by stiff elastic bonds that can break due to small deformations, such as brittle solids. For ductile materials that imply more plasticity and larger deformations, the bonds will be more elastic. SPH method was also analysed for cutting processes where the breakage was included.

Based on the same modelling principle, the crack propagation and crack branching of a brittle biopolymer material were modelled by using the Discrete Element Method (DEM) [118]. Taking into account medical applications, It was developed a coupled biomechanical-SPH model to simulate the behaviour of food in the oral cavity including the food breaking because of the teeth [119]. The simulations which were carried out considered the fluid flowing and the movements of biting and chewing food besides the interactions among the gums, teeth and tongue. Saliva, the liquid inside the mouth, was represented by a Newtonian fluid and solid food was represented by either elastoplastic or brittle elastic solids. The SPH model was selected for these simulations because its Lagrangian nature allows the modelling of fluid-free surfaces or solid fractures and interactions with complicated deforming boundaries. The oral cavity was truthfully reproduced by a biomechanical model.

Figure 23 shows three frame shots of the brittle food biting simulation.

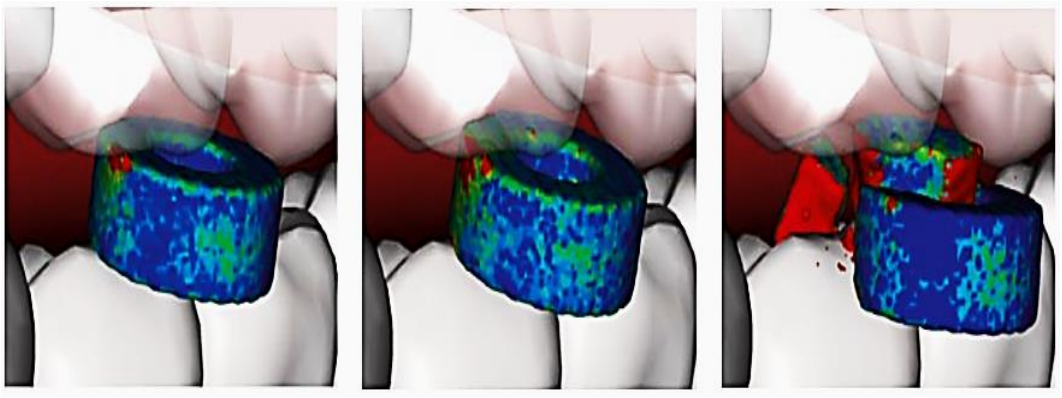


Figure 23. Simulation of a brittle object breaking because of the forces applied by jaws. SPH-biomechanical model applied. (Extracted from [120])

Finally, It was implemented a particle-based model, coupling DEM and SPH, to simulate the micromechanics of liquid core cells [120]. As in the previous models described where SPH and DEM are coupled, the liquid particles (liquid core) are represented by SPH model while the solid particles (viscoelastic cell membrane) are represented by DEM. The behaviour of the capsules is analysed for several

situations such as cell compression, relaxation after compression, impact and fracture of the cell membrane.

Figure 24 shows the modelled curve by SPH-DEM hybrid model is fitted to experimental data [121]. The Young Modulus of the capsule is also calculated on account of the Force-Displacement data obtained.

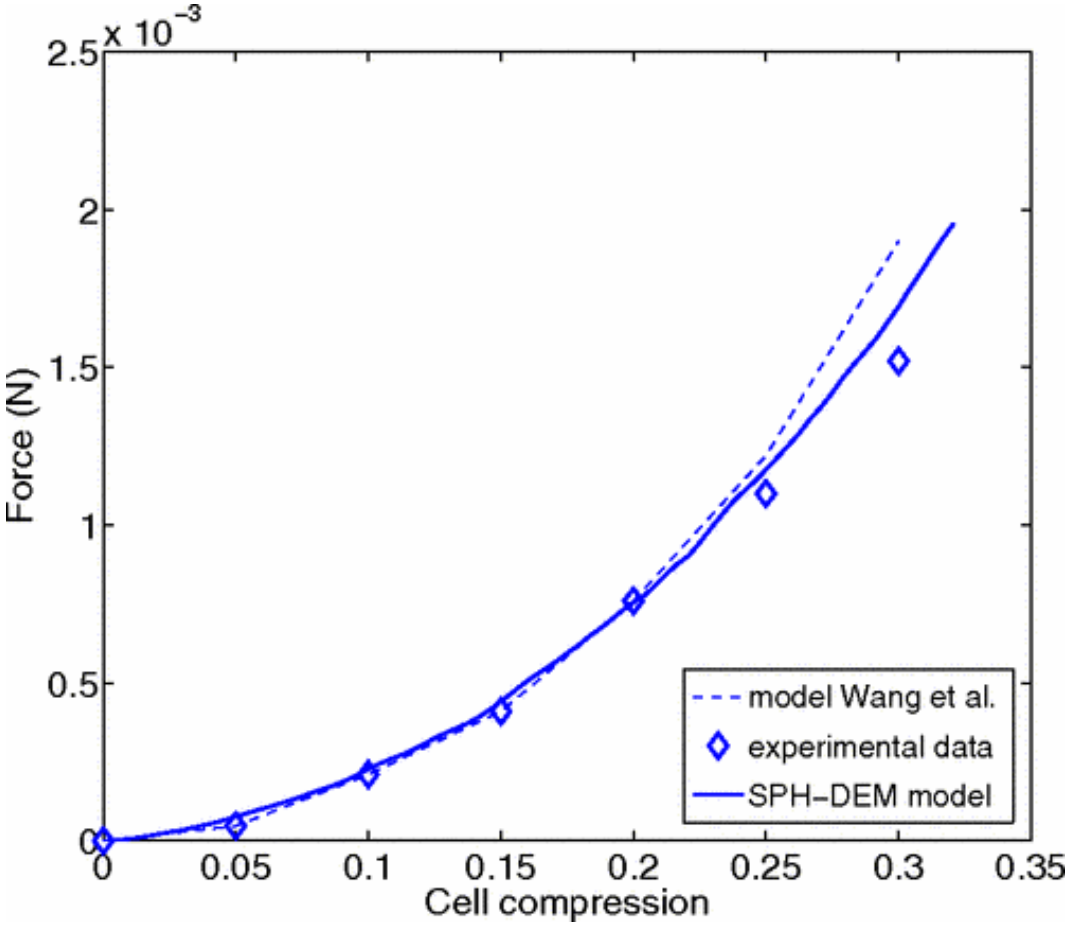


Figure 24. Force-Displacement plot obtained from compression parallel test. (Extracted from [121])

Figure 25 shows a snapshot of the fractured capsule after the simulation of the compression test by applying the DEM-SPH hybrid model. The possibility of predicting the force needed for the capsule failure and the type of failure depending on the type of capsule are very promising outcomes.

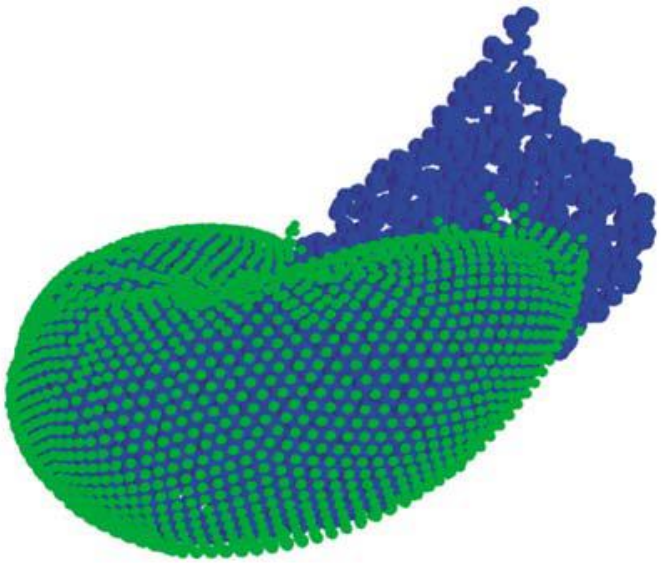


Figure 25. Snapshot of a cell fractured after the simulation of a compression test. (Extracted from [121])

2.8.4. Discrete multi-physics approach

The discrete multi-physics approach presented below has been validated for many processes where solid-fluid interactions take place, such as the hydrodynamics in an in vitro colon system [122], mass transfer in motile cilia in lungs [123], the study of emboli in flexible venous valves [124], the flow and agglomeration in deep veins valves [125] and phase-change materials in circular pipes [126]. After analysing the extensive number of applications of this multi-physics approach, it was considered a very valid option for the simulation of fluid-solid interactions and the mechanics of the capsules.

2.8.4.1. Methodology of multi-physics approach

The flowchart to develop DEM-SPH model is applicable to the discrete multi-physics approaches (Figure 26) [127].

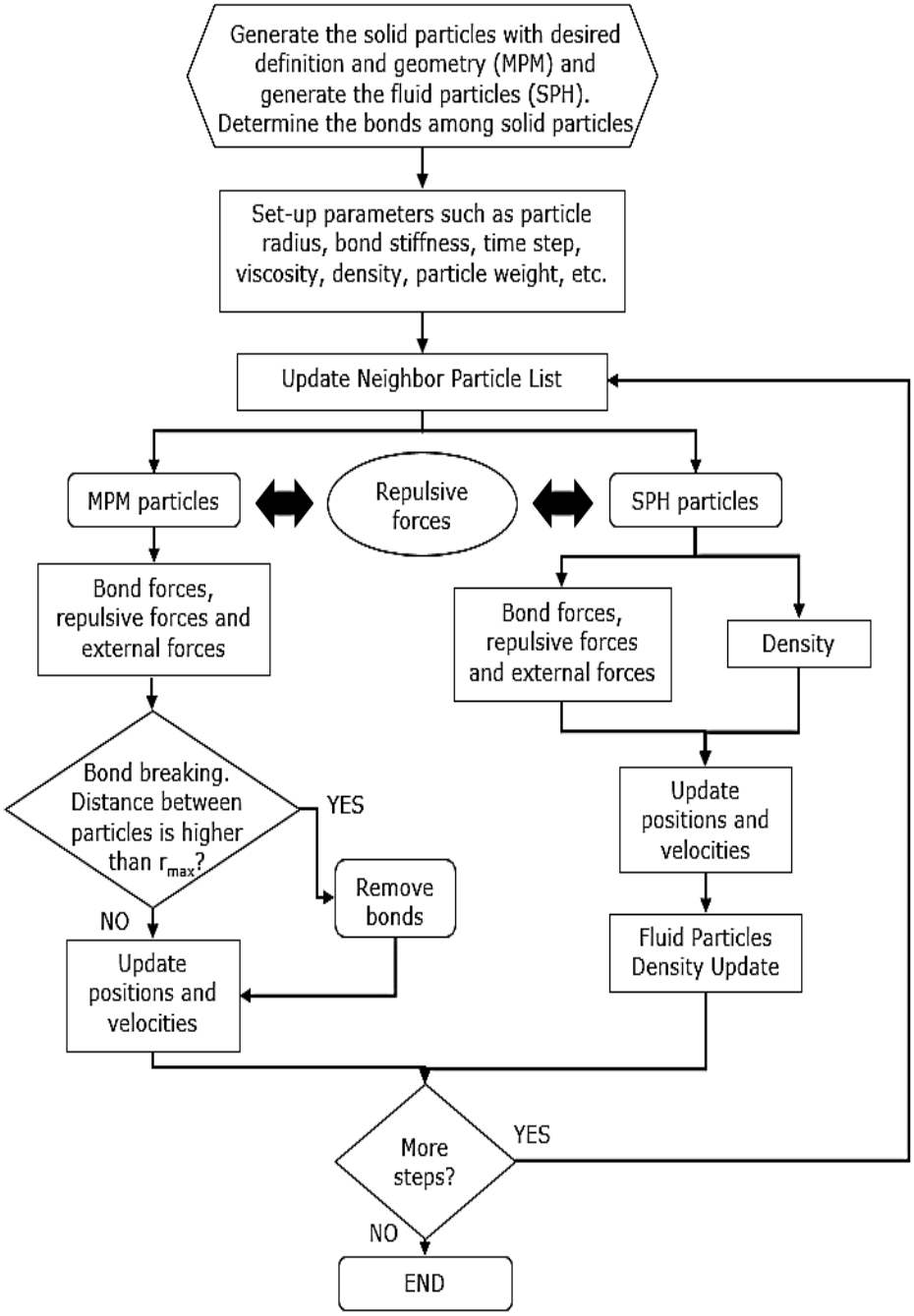


Figure 26. Flowchart for MPM-SPH multiphysics approach

2.8.4.2. Smoothed Particle Hydrodynamics (SPH) and Lattice Spring Model (LSM) for mechanics modelling

Mechanical characterisation is essential to understand the capsules behaviour during their manufacturing and use. The mechanical characterisation of capsules also allows us to estimate the value of elastic modulus and failure/strain. These are very important to determine the final applications of the capsules [88]. In addition, obtaining the value of these parameters is the computational starting point to address the control of the number of broken capsules because of the loads that are applied over the asphalt.

Recently, a Discrete Multi-Physics (DMP) approach has been used to validate the interactions between fluid and solid particles on several occasions [128]. In this study, DMP has been implemented to model the hydrodynamics and solid structure deformation. The hybrid model (DMP), based on a particle framework, includes Smoothed Particle Hydrodynamics (SPH) to simulate the hydrodynamics of liquid inside the capsule and the Mass and Spring Model (LSM) to simulate the mechanical properties of the shell. The SPH model and LSM share the common particle-based paradigm and the flowchart. Although each one is focused on different types of internal forces (SPH on hydrodynamics forces and LSM in deformation forces), the algorithm is very similar in both cases.

$$m_i \frac{dv_i}{dt} = m_i \frac{d^2 r_i}{dt^2} = \sum_{i \neq j} F_{i,j} + \sum F_E \qquad (2)$$

Where m is the mass, v the velocity, r the position, F_E the external forces and $F_{i,j}$ the internal forces. All of them refer to each particle. The particles are considered to be Lagrangian nodes (interpolation method) and at the same time, their position is updated by this equation which is the basis to link both models by means of the mathematical term of internal forces.

Smoothed Particle Hydrodynamics (SPH)

The idea of the SPH model is to build a set of disordered particles in the space-time without grid or mesh [129]. Each particle has an associated mass, momentum and energy and the motion of the particle is calculated from integration of Newton's second law. A property for each particle within the flow, such as density, velocity, energy per unit of mass, pressure and heat flux, is obtained from an interpolation of the neighbouring particles.

Lattice and Spring Model (LSM)

LSM is a model where the motion and the interaction of particles are studied. This model is based on Newtonian equations of motion. It it is crucial to define the type of interaction that occurs at the solid-liquid interface when linking the two models. The most common interactions occurring at the solid-liquid interface: no penetration, no slip and continuity of stresses [128].

Finally, the breakage can be also simulated by assuming that if the distance between two particles exceeds a certain maximum value (r_{max}), the bond is broken, and the two particles separated

CHAPTER 3

3. Materials and Methods

3.1. Introduction

The materials and methodologies applied in this research in order to find the optimum size and strength of C-alginate capsules are described in this chapter. This includes the characteristics of the materials used on the capsule manufacturing process and the encapsulation procedure performed to produce capsules with different diameters and strengths. The characteristics of the asphalt mixtures assessed in this research such as content of bitumen, air void content, aggregate gradation, and the type of bitumen and aggregates used are also detailed. Additionally, this chapter involves the different laboratory tests carried out to characterise the properties of the capsules and assess their performance once are added to the asphalt mixture. The wide laboratory testing programme performed was defined based on the experience from other authors and applicable to achieve the objectives of this research. In addition to that, new methodologies were implemented in this research such as the use a wheel tracker machine to evaluate the fatigue resistance and the self-healing properties of asphalt mixtures with and without capsules. Xray tomography was applied to visualise the evolution of the damage generated on the asphalt samples and the capsules after the fatigue loading.

3.2. Encapsulation procedure of the rejuvenator

The healing agent used was sunflower oil, with density, smoke point and flash point, 0.91 g/cm^3, 227 °C and 315 °C, respectively [6]. The matrix that contained the oil in the capsules was made from low viscosity sodium alginate ($C_6H_7O_6Na$) and calcium chloride ($CaCl_2$), provided with 95 % purity in powder and granular pellets, respectively, by Sigma-Aldrich.

The calcium alginate capsules were produced through ionically cross-linking of sodium alginate in the presence of calcium ions (ionic external gelation) [72].

First, at 25 ºC, a mixture of water and sunflower oil was prepared with volume ratio 10/1 by agitating both materials at 800 rpm for 5 minutes. After, sodium alginate was added and agitated for 15 minutes, which produced a homogenous suspension. Emulsions with oil-sodium alginate (O/A) mass ratios 2/1, 2.5/1, 3/1 and 3.5/1 were made.

Second, at 25 º C, emulsion droplets of four different diameters were created using syringes connected to a needle of 0.81 mm, a dropping funnel of 5 mm of internal diameter and a PVC pipe of 5 mm of internal diameter, see Figure 27 (a). By using the needle of 0.81 mm capsules of 0.7 mm and 1.3 mm of diameter where manufactured. The difference in the size was reached by changing the pressure in the syringe, by means of a peristatic pump. The dropping funnel generated the capsules with 2 mm of diameter. The 3 mm capsules were obtained by connecting a PVC pipe with 5 mm of internal diameter to the syringes. The PVC pipe was placed creating a 45 º angle to increase the size of the drop. The droplets were introduced into a calcium chloride solution at 2 %$_w$, which induced the polymerization of the calcium and alginate. When the emulsion droplet was inside the calcium chloride solution, the $Ca2^+$ ions migrated from the solution to the capsules replacing Na^+ ions, see Figure 27 (b and c). During the capsules' formation process, the calcium chloride solution was agitated with a magnetic stirrer, to avoid that the capsules

would stick to each other, see Figure 27(a).

Third, two hours after the last capsule had been formed, the capsules were removed from the calcium solution and, dried at 40 ºC for 24 hours, see Figure 27(d).

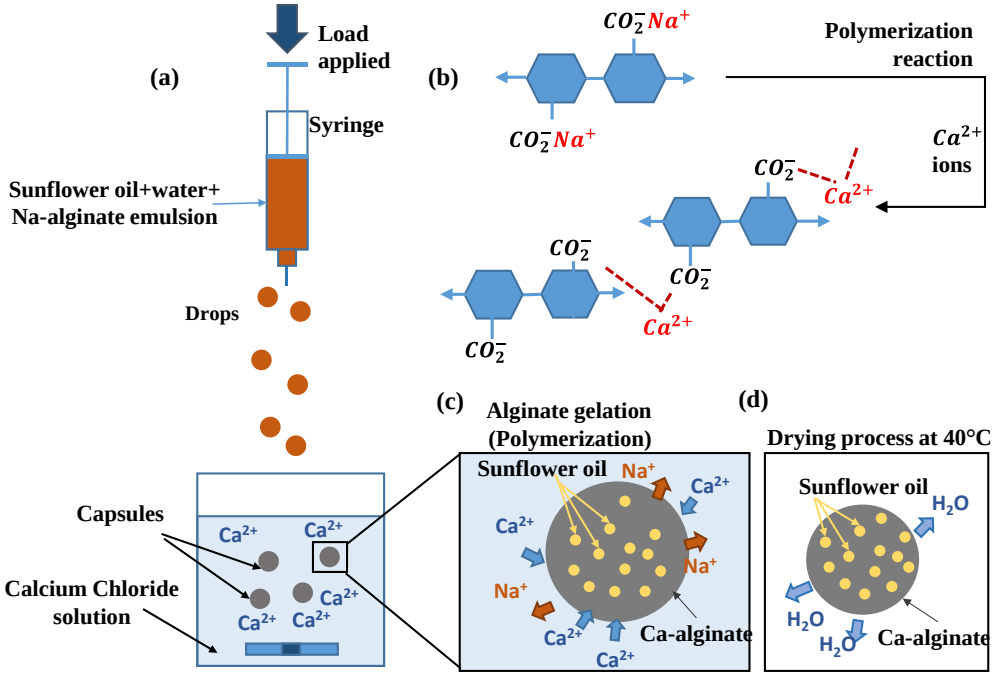


Figure 27. Scheme of ionic external gelation of alginate and sunflower oil encapsulation

Capsules having a diameter smaller than 0.7 mm were not assessed in this research due to the issues encountered during the manufacturing process to get smaller sizes. Additionally, it was considered that the activation efficiency could be reduced for capsules with that size.

3.3. Dimensions of the capsules

15 different types of capsules with a range of diameters and O/A ratios were manufactured with a density of 1.13±0.03 g/cm^3. The dimensions in the three perpendicular directions were determined by means of an electronic calliper. The

values represented in Table 2 were calculated as the average of 10 capsules for each type. The standard deviations are included in the measurements.

Table 2. O/A ratios and capsule's sizes

O/A Ratio	Diameter (mm)			
	3	**2**	**1.3**	**0.7**
2 / 1	3.07±0.01	2.00±0.16	1.29±0.07	--
2.5 / 1	3.14±0.01	2.05±0.09	1.28±0.05	0.71±0.09
3 / 1	3.05±0.01	1.92±0.06	1.32±0.08	0.74±0.12
3.5 / 1	3.02±0.01	2.04±0.16	1.24±0.14	0.67±0.13

From now on, capsules will be named as follows, Diameter-O/A ratio; for example, 3-2/1 means capsules of 3 mm and oil-alginate ratio 2/1.

3.4. Capsule imaging

A scanning electron microscope was used to image the shell of the capsules and its internal morphology including the pore's diameter. For the internal morphology, capsules were cut in halves, cleaned with paper and acetone to remove oil over capsule surfaces and fixed on a sample holder with adhesive after 1 hour in order to avoid disturbance in the imaging process. Capsule images were taken on a Q650 SEM (FEI) at a pressure of 80 Pa to 100 Pa. Additionally, an elemental mapping was performed through energy-dispersive X-ray spectroscopy to identify the distribution of expected elements in the capsules. This technique consists of taking a high-resolution image of the interesting area by the energy-dispersive X-ray spectroscope, and has been widely applied for the elemental identification of composite materials [130]–[132]. Each pixel in the image is correlated with the EDS

data. Depending on the intensity of this correlation, the image is coloured in different layers which is related to the elemental compositional information of the sample.

3.5. Computed Tomography X-ray Scanning

A Phoenix Nanotom S with a 180kV nano focus Computed Tomography X-ray scan and equipped with high precision rotation-unit, with air bearing for higher accurate CT images, was used to examine capsules with 4 different oil/alginate (O/A) ratios (2; 2.5; 3; 3.5) and diameter, 1.3 mm. These capsules were scanned with a resolution of 1.25 µm and 3D images were generated. Approximately one thousand 2D transversal images were processed and analysed for each capsule by the free software "Image J". The noise was filtered, and the imperfections of the images were removed. The images were turned into binary to differentiate between the calcium alginate shell and the space inside the capsule filled by sunflower oil. The software counted each type of pixel and the porosity, ε, was calculated as:

$$\varepsilon = \frac{A_{pores}}{A_{total}} \quad (3)$$

where A_{total} is the total area of the capsule and A_{pores} is the area of the pores inside the capsule.

3.6. Quantification of ions released by the surface of a capsule's shell by ICP-OES

The salt formation in the capsule´s shell could have an influence in the bitumen adhesion to the capsules because of the change in the alkalinity. In order to understand the crystallization of sodium and calcium at the capsules' surface, the capsules were submerged in tap water and, an analysis of the ion concentration of

water was made. Ten 1.3-3/1 dry capsules were placed inside a test tube with 5 ml of deionized water. After 10 days, 4 ml of water was extracted, and 1 ml of a 10% nitric acid solution was added to the extracted water. This procedure was repeated with a blank sample of tap water to compare the results. The solutions were measured by an Inductively Coupled Plasma Optical Emission Spectroscopy (ICP-OES) equipment capable of measuring ion concentration up to parts-per-million levels. The ion concentration of calcium and sodium in the water were obtained.

3.7. Capsule strength to compression load

The mechanical behaviour of single capsules was measured through a uniaxial parallel plate compression test on an Instron 5969 dual column testing system with a 5 kN loading cell (see Figure 28). The test was displacement controlled with a loading speed of 0.3 mm/min. Capsules were tested until a vertical displacement equivalent to the capsule's radius was reached. This process was performed for three capsules per capsule type. In order to analyse the strength of the capsules at temperatures equivalent to those during asphalt mixing and compaction, the compression test was performed at 160 ºC, 60 ºC and 20 ºC.

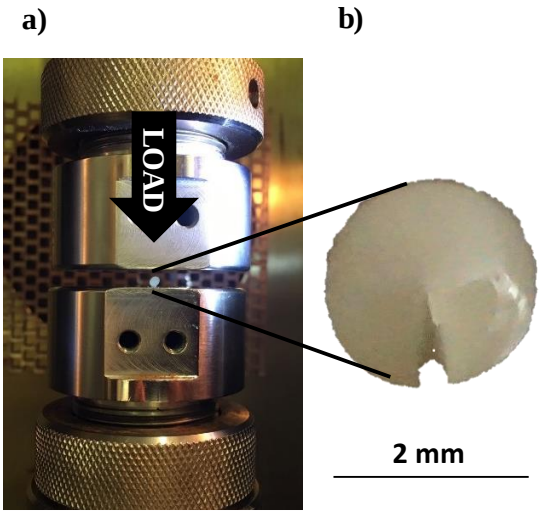


Figure 28. (a) Compression test setup. (b) Capsule type 2-2.5/1 at the end of the compression test

3.8. Thermogravimetric analysis

The thermal stability and resistance of the capsules manufactured were investigated by means of a thermogravimetric analysis performed on a SDT Q600 (TA Instruments). The mass loss over time was determined for a temperature ramp from 25 ℃ to 250 ℃ with a heating rate of 10 ℃/min. In order to analyse the influence of the O/A ratio on the thermal stability, capsules type 1.3-2/1, 1.3-2.5/1, 1.3-3/1 and 1.3-3.5/1 were tested. Additionally, in order to analyse the influence of size on the thermal stability, capsules type 0.7-2.5/1 and 3-2.5/1 were tested. Furthermore, the thermal stability of the individual capsules' components (calcium alginate and sunflower oil) was analysed. In addition, the change in the capsule's dimension caused by temperature changes was determined by a thermomechanical analysis performed on a Q400 TMA (TA Instruments). Two heating profiles were applied to measure the one direction dimensional change of a capsule. The first heating profile was a temperature ramp, heating a capsule from 25 ℃ to 250 ℃ at a heating rate of 10 ºC/min. The second profile consisted of 7 cycles of heating and cooling in the temperature range of -10 ℃ to 60 ℃, at a rate of 10 ºC/min. To ensure contact between probe and capsule, a force of 0.2 N was applied.

3.9. Influence of temperature and/or load on the oil-release from capsules

The oil release from the calcium-alginate capsules was analysed, to relate it to the potential self-healing properties of asphalt. The amount of oil released was determined by the weight difference of the capsules before and after exposing them to a range of temperatures and loads. The oil released was removed by rinsing the capsules with acetone after testing. Four different testing cases were done, which were repeated 5 times for each type of capsule analysed.

Case 1. Heating-cooling cycles: the amount of oil released from all the capsules in Table 2 was quantified after seven 1 hour heating/cooling cycles, where the temperature was changed from -10 °C (time 0 minutes) to 60 °C (time 30 minutes) to -10 °C (time 60 minutes). These ranges of temperatures were selected to simulate extreme day/night cycles.

Case 2. Load below the yield point: a 3 N static load was applied over capsules 1.3-2/1, 1.3-2.5/, 1.3-3/1 and, 1.3-3.5/1. This load was below the yield point of the capsules, as it will be shown in the next sections of the report. This test was repeated in 20 capsules of each type.

Case 3. Load at the yield point: the amount of oil released from the capsules was measured at the yield point of the capsules type 1.3-2/1, 1.3-2.5/, 1.3-3/1 and, 1.3-3.5/1.

Case 4. Extreme deformation of the capsules: the amount of oil released from the capsules was measured when their deformation was higher than 50% their original diameter in a compression test. This test was done for capsules 1.3-2/1, 1.3-2.5/, 1.3-3/1, 1.3-3.5/1, 0.7-2.5/1, 2.3-2.5/1 and, 3-2.5/1.

3.10. Asphalt mixture materials

This research has been done using Stone Mastic Asphalt (SMA) in accordance with EN 13108 Part 5, which is a material that is commonly used to build surface courses of roads in the UK.

SMA mixtures were manufactured with bitumen 40/60 pen, with a density of 1.030 g/cm^3 and, graded Tunstead limestone aggregate, with density of 2.700 g/cm^3. Aggregate gradation and SMA design properties are shown in Figure 29 and Table 3, respectively. The standard limits were extracted from BS EN 13108-5.

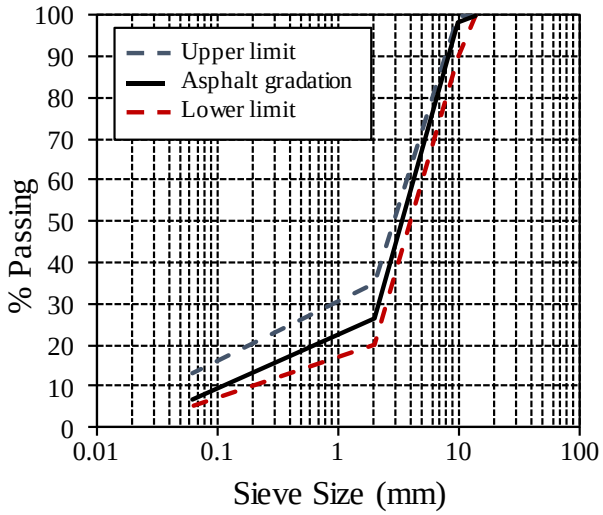


Figure 29. Aggregates gradation for the SMA mixtures

Table 3. Design properties of the Stone Mastic Asphalt mixture

Property	Value	Standard limits
Binder content (%M)	5.6	>5
Bulk density (g/cm^3)	2.446	-
Maximum density (g/cm^3)	2.575	-
Air void content (%)	5	1.5-14
Voids in mineral aggregate (%)	14	-

3.11. Capsules that have been mixed in asphalt

The selected polymeric capsules to be added to the asphalt mixture had a density of 1.13 ± 0.03 g/cm^3 and ten different sizes were prepared (see Table 4). As explained in previous sections, the rejuvenator used was sunflower oil with density, 0.91 g/cm^3, smoke point, 227 °C, and flashpoint, 315 °C [15]. As it was reported in [6],

[14], [51], the shell of the capsules, which contained the oil was made of low viscosity sodium alginate, 95 % purity, (C6H7O6Na in powder) and calcium chloride (CaCl2 in granular pellets) provided by Sigma-Aldrich, UK.

Table 4. Properties of the Ca-alginate capsules manufactured

Capsule	**A**	**B**	**C**	**D**	**E**	**F**	**G**	**H**	**I**	**J**
Capsule Diameter, CD (mm)	1.29± 0.07	1.28± 0.05	1.32± 0.08	1.24± 0.14	3.07± 0.01	3.14± 0.01	2± 0.16	2.05± 0.09	0.71± 0.09	0.74± 0.12
Oil/Sodium Alginate ratio, O/A	2	2.5	3	3.5	2	2.5	2	2.5	2.5	3
Compressive force (N)	25.45	11.62	11.36	6.57	88.03	62.59	61.2	43.44	6.65	3.4

3.12. SMA beams manufacturing

Prismatic SMA test specimens were prepared in this study. Mixing and compaction were carried out according to the standard BS EN 12697-33. The weight of capsules added to the SMA mixtures was 0.5 % over the total mass of the mixture as previous researchers established that this quantity was the optimum amount to maximize the self-healing properties of the asphalt. SMA mixtures with different types of Ca-alginate capsules and without capsules were manufactured in batches of 8.13 kg. The bitumen and aggregates were pre-heated at 160 °C for 4 and 12 hours, respectively. Then, the raw materials were mixed for 3 min at 125 rpm at 160 °C.

Before mixing, the capsules were preconditioned at 25 °C for 24 hours. Aggregates and bitumen were mixed for 3 minutes at 125 rpm at 160 °C and then, the capsules were uniformly added to the laboratory mixer and mixed for 20 additional seconds, ensuring a good distribution of the capsules (BS EN 12697-35)

Finally, the SMA mixtures were transferred to steel moulds with dimensions 305 x 305 x 35 mm^3 for their compaction and cutting. SMA slabs were compacted using a roller compactor at 145±3 °C, to reach a target density of 2446 kg/m^3 and 5 % of air voids. Then, prismatic samples with dimensions 305 x 48 x 35 mm^3 were extracted from the asphalt slabs. These beam dimensions are the dimensions required by the fatigue test in the laboratory wheel tracker [6].

3.13. Bulk density and air void content

The British standard BS EN 12697, Part 6 (2012) was used to measure the bulk density, ρ_b, of the asphalt mixtures manufactured with and without capsules. ρ_b was calculated by dividing the mass of the dry specimen in the air between the difference of the masses of the specimen in air and water and multiplied by water density at the ambient temperature.

ρ_b was used to measure the air void content, V_a, of the asphalt mixtures studied according to BS EN 12697-8:2018, as follows:

$$V_a = \frac{\rho_m - \rho_b}{\rho_m} \cdot 100 \quad (4)$$

The maximum density of the test specimens was determined according to BS EN 12697, part 5 (2009) by dividing the dry mass by the measured volume of test samples.

Each bulk density and air void content result presented in this report is the average density of 5 specimens.

3.14. Reflective cracking repeated loading durability

The reflective cracking was generated by using a wheel tracker machine [6]. It consists of a wheel passing repeatedly and applying a determined load over the asphalt beam. This test counts the number of cycles needed to generate a crack equivalent to 50% of the thickness of the asphalt beam. The asphalt beams were placed over two concrete plates, which created a gap of 30 mm. To induce bending during the fatigue test, a flexible neoprene layer was placed under the concrete plates (see Figure 30). Additionally, the asphalt beams were painted in white to facilitate visual crack detection due to the colour contrast.

Each cycle lasted 2.4 seconds and the forces applied over the sample were 621 N, 723 N, 825 N, 930 N and, 1032 N. The tests were carried out at 20 ^{o}C. Each test was repeated using 8 specimens, to obtain the median of the number of cycles resisted [133], $N_{0.5}$. Eleven different asphalt mixtures were tested, including asphalts with all the types of capsules in Table 4 and, the asphalt mixture without capsules.

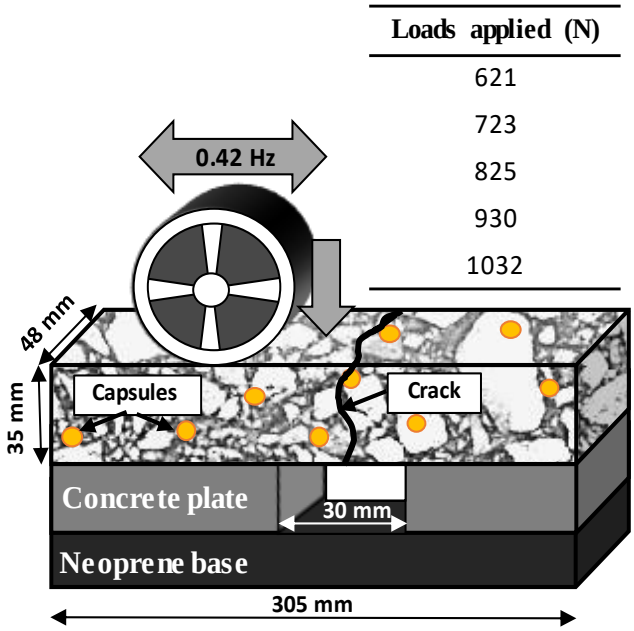


Figure 30. Scheme of reflective cracking repeated loading test.

To analyse the fatigue resistance results, a Fatigue resistance Index, FI, was created by relating the number of cycles until the complete failure of the different asphalt samples with capsules to the number of cycles of asphalt without capsules, see Equation 5:

$$FI = \frac{Nº\ cycles\ (asphalt\ with\ capsules)}{Nº\ cycles\ (without\ capsules)} \quad (5)$$

3.15. Quantification of crack self-healing

Previous researchers found that a resting time may be important to maximize the healing effect by capsules containing a bitumen rejuvenator. This resting time is needed by the sunflower oil to reduce the viscosity of the bitumen and allow it to flow into the cracks [134]. Also, [134] demonstrated that the maximum healing level is reached at 24 hours of resting time and remains constant after this period. Hence, a resting period of 24 hours at 20 °C has been chosen for the materials studied in this report.

To determine the optimum number of cycles during the wheel track test where the resting time is more effective, reflective cracking fatigue tests were carried out with beams of asphalt mixture without capsules and with capsules type C (see Table 4). The number of loading cycles corresponded to 25%, 30%, 35%, 40% and 50% of N0.5 [6]. After, the beams were allowed to rest for 24 hours at 20 °C. Finally, the beams were subjected to cyclic loading until failure and the total number of cycles that they resisted was measured (N_t). The self-healing was calculated according to the following equation:

$$HI = \frac{N_t - N_{0.5}}{N_{0.5}} \quad (6)$$

where HI is the healing index, N_t is the total number of cycles quantified and $N_{0.5}$ is the median number of cycles to fracture.

This procedure was repeated for asphalt mixtures with all the capsule types shown in Table 4 applying the resting time at the optimum percentage of the median number of cycles (N0.5) obtained in the previous tests.

3.16. Computed Tomography (CT) Scanning of asphalt mixture

Reflective cracks and their healing were visualized using X-ray CT scanning. Using a GE Sensing and Inspection Technologies GMBH VTomeX M X-ray scanner [52]. An asphalt beam with capsules type H was scanned (i) before loading, (ii) after loading until 30 % of the median number of cyclic loads in the wheel track test and, (iii) after resting for 24 h, at 20 °C. The CT Scan took 40 minutes for each sample to be analized. Only the central part of the beam, which is prone to develop reflective cracking, and has a volume of 60x48x35 mm^3, was analysed. Finally, 2D image slices were obtained and reconstructed into 3D images using the ImageJ software package.

Additionally, another scanner, Phoenix Nanotom S with a 180kV nano focus Computed Tomography X-ray scanner, equipped with a high precision rotation-unit and higher accuracy, was used to examine the structure of capsules type H when they were extracted from the asphalt mixture after mixing and compaction and also capsules extracted from a specimen after testing cyclical reflective loading in the laboratory wheel tracker. The capsules were carefully extracted with the help of spatula. These capsules were scanned at 20. °C using a resolution of 1.25 µm and 3D images were generated. Approximately one thousand 2D transversal images were processed and analysed for each capsule using Image J.

3.17. Capsule imaging of capsules after asphalt mixing and compaction

A scanning electron microscope was used to image the shell of the capsules type H when they were extracted from the asphalt mixture after mixing and compaction and, also capsules extracted from a specimen after testing cyclical reflective loading in the laboratory wheel tracker. Capsule images were taken on a Q650 SEM (FEI) at a pressure of 80 Pa to 100 Pa.

3.18. Amount of oil released by the capsules

The volume of sunflower oil released from the capsules into the asphalt mixture beams during fatigue tests was analysed using Fourier Transform Infrared Spectroscopy (FTIR), following the methodology described by [52]. Small bitumen samples were randomly taken from five spots of the surface of the asphalt mixture beam with capsules and then homogenised in order to have a representative sample of the overall amount of oil released. The process was repeated (i) after mixing and compaction and, (ii) after cyclical reflective loading, at a load of 930 N, in the wheel tracker. To have reference values, samples of virgin bitumen and sunflower oil were prepared and their FTIR spectra were obtained.

The volume of sunflower oil was evaluated from the changes in the absorbance peak between the wavenumbers 1700 cm^{-1} to 1800 cm^{-1} [4]. Therefore, FTIR absorbance spectrum was normalized in the selected wavelength range and, the absorbance area under the spectrum was measured using the trapezoidal rule of numerical integration [14], see Figure 31. Finally, the volume of oil released, OR as quantified as a percentage of the total oil encapsulated in the asphalt:

$$OR\ (\%) = \left(\frac{A_{1745} - C_i,F_i}{A_{1745} - 100\%}\right) \times 100 \qquad (7)$$

Where, $A_{1745\text{-}Ci,\ Fi}$ is the absorbance area at the peak 1745 cm^{-1} for the asphalt with capsules at the different number of cycles (C_i) and forces (F_i), and $A_{1745\text{-}100\%}$ is the absorbance area at peak 1745 cm^{-1} for the asphalt samples with 100% of capsules broken. This procedure was repeated for asphalt samples with all the types of capsules shown in Table 4.

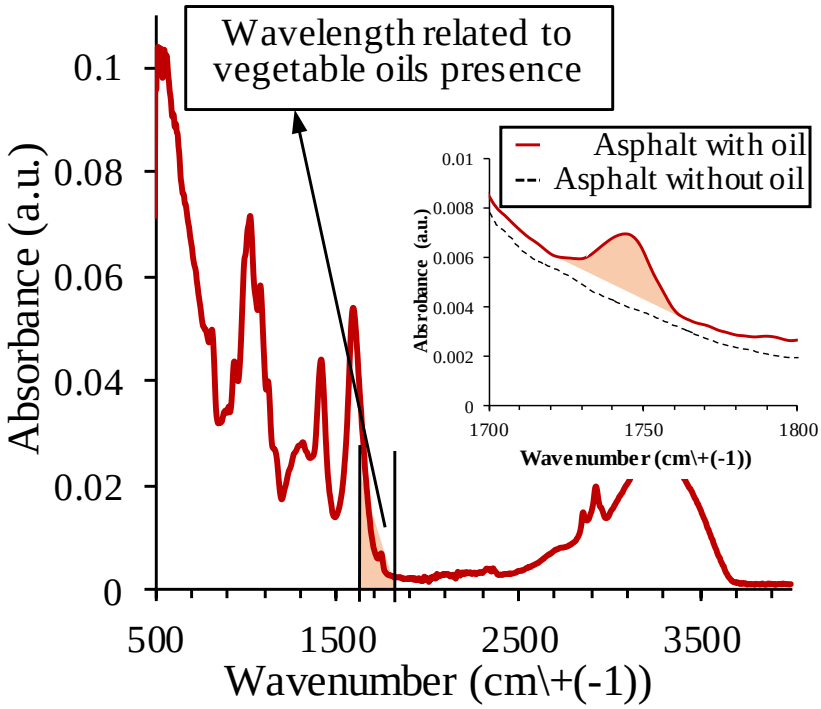


Figure 31. FTIR curves for the quantification of sunflower oil released by the capsules. Modified from [51].

3.19. Effect of capsules on the skidding resistance of asphalt

In order to evaluate the effect of the oil release on the skid resistance of SMA slabs, dynamic pendulum test measurements were done during the wheel tracking test according to BS EN 13036-4 (BSI 2011). In this test, the values measured represent the friction properties of the surface given by the British Pendulum Number (BPN).

All the tests were done at 20°C and the BPN value was calculated using the average of five tests. This procedure was repeated for different asphalt samples with all the capsule types shown in Table 4.

3.20. Effect of capsules on the permanent deformation (rutting) of asphalt

In order to understand if the oil released by the capsules, which may reduce the viscosity of bitumen, influenced the permanent deformation of asphalt, rutting was analysed following the EN 12697-22 standard. A BM585 wheel tracker was used and the asphalt slabs were dry during the test.

The tests were carried out at 20 °C, with a rate of 26.5 passes/min, applying a repetitive load of 700 N. The test will be continued until the wheel reached 10000 passes or the depth of the wheel reaches 20 mm. This procedure was repeated for asphalt mixtures with 0.5% of capsules over the total asphalt mixture slab mass. All the capsules shown in Table 4 were tested.

CHAPTER 4

4. Properties of Ca-alginate capsules to maximise asphalt self-healing properties

4.1. Introduction

Ten different Ca-alginate capsules were manufactured modifying the proportions of the materials in this initial emulsion mix (Na-alginate, sunflower oil and water) to generate different capsule's sizes and strengths. This chapter provides findings about the influence of the variation of the strength and diameter of the capsules on their internal structure and thermal and mechanical properties. In addition, it provides preliminary explanation about the diffusion of the bitumen rejuvenator (sunflower oil) through the shell materials when the capsules are subjected to changes of temperature or compressive load applied. Promising results were also obtained regarding the stability of the capsules at the high temperatures reached on the asphalt manufacturing process.

4.2. Morphological characterization of Ca-alginate capsules that contain sunflower oil

The oil encapsulation by the ionic external gelation of sodium alginate consists of the migration of $Ca2^{+}$ ions from an aqueous bath to the emulsion drop [72]. This results in a Ca-alginate matrix with a highly cross-linked surface and a bit less cross-linked internal part. Figure 32 (a) shows a 3D reconstruction from the CT scanning images of the surface of a capsule type 1.3-2/1, where a rough surface can be observed. The capsule is composed of small deposits containing oil. These are reflected in the surface, as it can be seen in the SEM image of the capsule's surface, shown Figure 32 (d), which could release small amounts of oil if the surface is damaged during mixing and compaction. Due to the multi-cavity structure of the capsule, see Figure 32 (e), if a section of the capsule is damaged, for example the surface, not all the oil is lost. This could imply that, since capsules may not release all their payload when they are damaged, they could be used to heal cracks formed in different stages around the same capsule location. In addition, this could support the results found in [16], which found that oil is released gradually, at the same time that the damage of the asphalt increases.

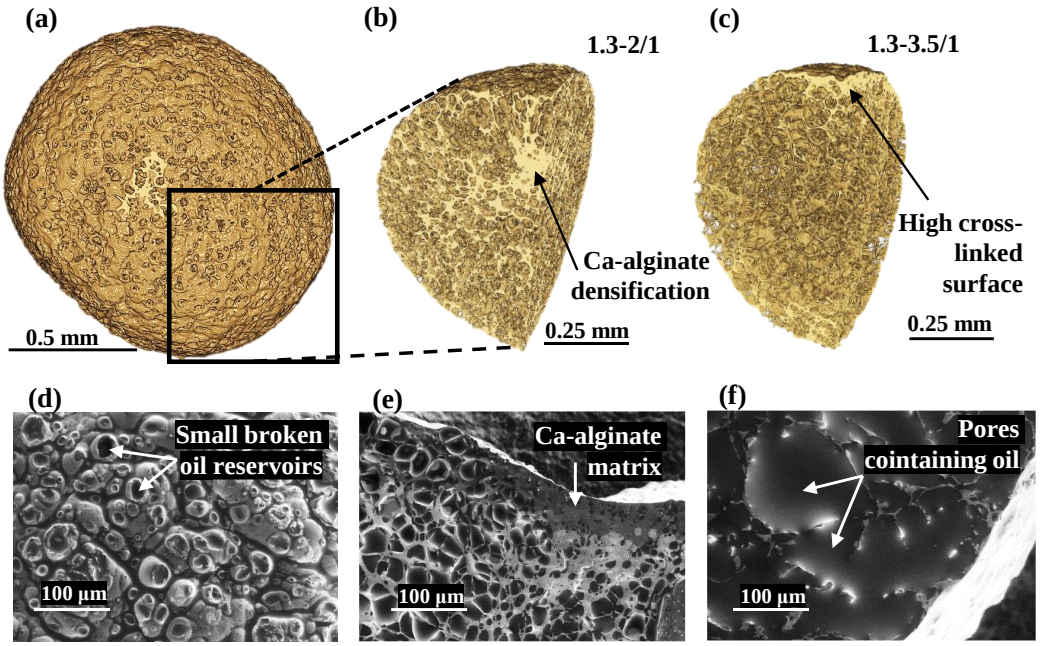


Figure 32. (a) 3D reconstruction of a capsule type 1.3-2/1. (b) Internal structure of a capsule type 1.3-2/1. (c) Internal structure of a capsule type 1.3-3.5/1 obtained by CT scanning. (d) SEM image of the surface of a capsule type 1.3-2/1. (e) SEM image of the internal structure of a capsule type 1.3-2/1. (f) SEM image of the internal structure of a capsule type 1.3-3.5/1.

Figure 32 (b) and Figure 32 (c) show 3D reconstructions from CT scan images of capsules type 1.3-2/1 and 1.3-3.5/1, respectively. The internal structure of these capsules is also shown in Figure 32 (e) and Figure 32 (f), which are SEM images of transversal cuts of capsules type 1.3-2/1 and 1.3-3.5/1. The capsule with a higher concentration of alginate is 1.3-2/1, which shows a denser internal skeleton internal structure and a smaller pore size than the capsule type 1.3-3.5/1. These figures indicate that adding higher amounts of alginate will produce stronger capsules.

Table 5. Main characteristics analysed of the different capsules tested.

Capsule type	1.3-2/1	1.3-2.5/1	1.3-3/1	1.3-3.5/1	3-2.5/1	2-2.5/1	0.7-2.5/1
Capsule Diameter, CD (mm)	1.29± 0.07	1.28± 0.05	1.32± 0.08	1.24± 0.14	3.14± 0.01	2.05± 0.09	0.71± 0.09
Oil/Sodium Alginate ratio, O/A	2	2.5	3	3.5	2.5	2.5	2.5
Pore Size, PS (µm)	11.38 ±3.07	15.44 ±4.28	16.75 ±8	18.84 ±5	12.27 ±0.8	12.03 ±1.3	11.31 ±2.9
Roundness, R (Dimensionless)	0.63± 0.19	0.72± 0.14	0.63± 0.18	0.68± 0.16	0.64± 0.21	0.65± 0.2	0.68± 0.19

Table 5 shows the main properties of capsules 1.3-2/1, 1.3-2.5/1, 1.3-3/1, 1.3-3.5/1, 3-2.5/1, 2-2.5/1 and 0.7-2.5/1. In addition, Table 6 shows Pearson correlation coefficient of the main manufacturing parameters influencing the properties of the capsules, such as Capsule Diameter, CD, Oil/Sodium Alginate ratio, O/A, Pore Size, PS, and Roundness, R, which allows to show the relationship between the variables.

Table 6 shows that there is high Pearson correlation coefficient between the O/A ratio and PS. As it was observed in Figure 32, the higher the oil/alginate ratio during manufacturing, the bigger the pore size of the capsules. This result could have a significant influence on the amount of oil released by the capsules. It can be assumed that the bigger the pore size, the bigger would be the amount of oil released. Based on this, it could be possible to heal cracks of different sizes by controlling the O/A ratio.

It was not possible to establish more relationships between the other variables. Since the diameter is not influenced by the oil and alginate relationship, it has to be controlled mainly by the size of the droplet. Finally, the capsule's roundness seems to be constant and non-dependant of any of the factors studied.

Table 6. Pearson correlation coefficients of the relationships between roundness, diameter, pore diameter of the capsules and lose of weight.

	CD	**O/A**	**PS**	**R**	**LW**
CD	1	-0.135	-0.236	-0.379	-0.466
O/A		1	0.878	0.194	-0.896
PS			1	0.299	-0.926
R				1	-0.053
LW					1

4.3. Capsule components identification

During the imaging process by SEM microscopy, crystals were observed over the capsule surface. In order to identify the components of these crystals, an elemental mapping was performed by means of energy-dispersive X-ray spectroscopy, see Figure 33 (a) and Figure 33 (b). Based on the intensity of the coloured images obtained for Na and Cl elements, see Figure 33 (a), the crystals were identified as a sodium chloride salt, excluding other elements such as Ca in its formation. The formation of sodium chloride salts may be related to the end of the ions exchange process, which takes place in the ionic external gelation [132]. The sodium ions (Na^+) come from the sodium alginate, whereas the calcium ions (Ca^{2+}) come from the saturated $CaCl_2$ solution, which works as a hardener in the capsule formation.

In order to confirm these points, the capsules were placed in tap water to dissolve the salts and, the concentration of sodium and calcium ions were measured by means of Inductively Coupled Plasma Optical Emission Spectroscopy. Figure 33 (c) shows that the concentration of $Ca2^+$ and Na^+ ions in the tap water where the capsules were placed previously was 71.69 ppm and 228.08 ppm, respectively, while it was 523.79 ppm and 320.89 ppm, respectively, after dissolving the salts from the capsule´s

surfaces. This result supports the theory of the end of ions exchange and the chemical reaction finalised indicated by the increment of Na^+ ions whereas the increment of Ca^{2+} was due to the oversaturated $CaCl_2$ solution used as hardener in the capsules production.

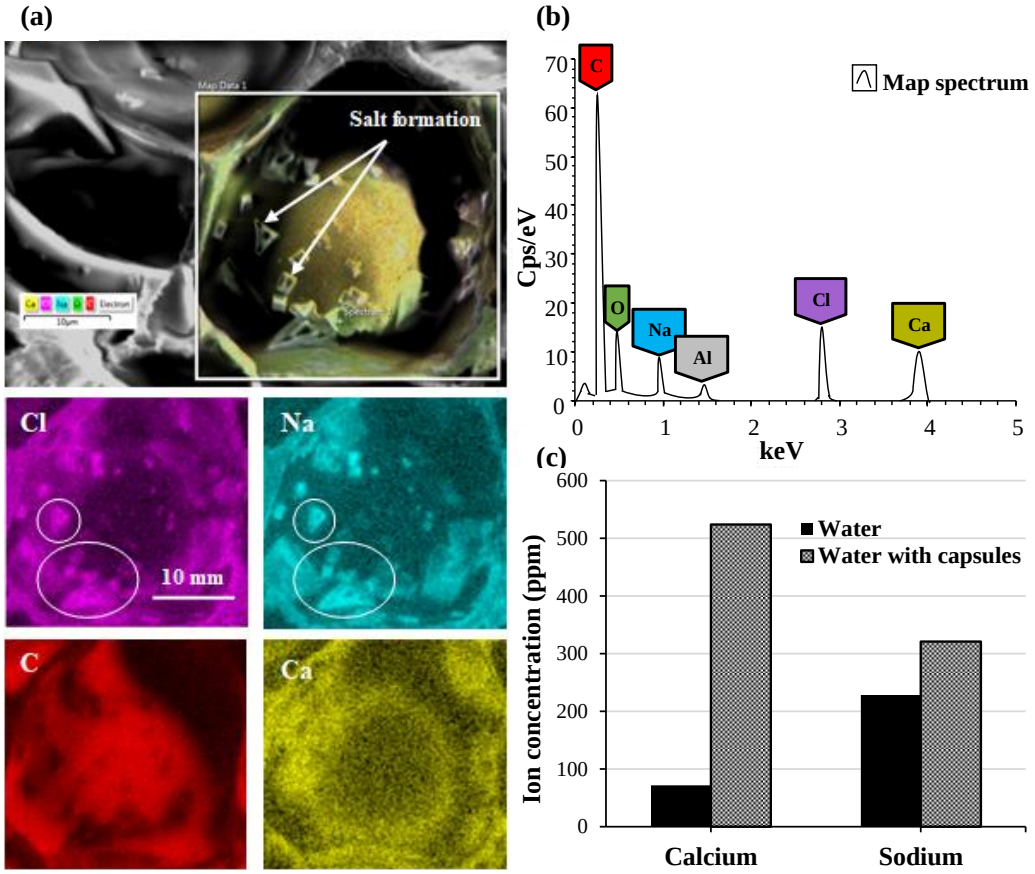


Figure 33. (a) Elemental identifying images. (b) Elemental mapping generated by energy-dispersive X-ray spectroscopy. (c) Calcium and sodium ions concentration after release from the capsule's surface.

4.4. Effect of the capsule's diameter and O/A ratio on the capsule's strength

Figure 34 shows the example of a stress-strain curve of a single capsule (3-2/1), tested under parallel compression. All the capsules studied showed a similar profile

in the compression tests. The yield point was taken as the reference strength to compare the strength of the different capsules. It has been defined as the point where the capsules ruptured. Below this yield point the capsules showed an elastic behaviour and they star to release small amounts of oil. When the load was higher, permanent deformations started to appear and the capsule starts to show fractures at the same time that the sunflower oil is released gradually. In a practical case scenario where asphalt with capsules received traffic loading, there were capsules receiving loads under and over the yield point.

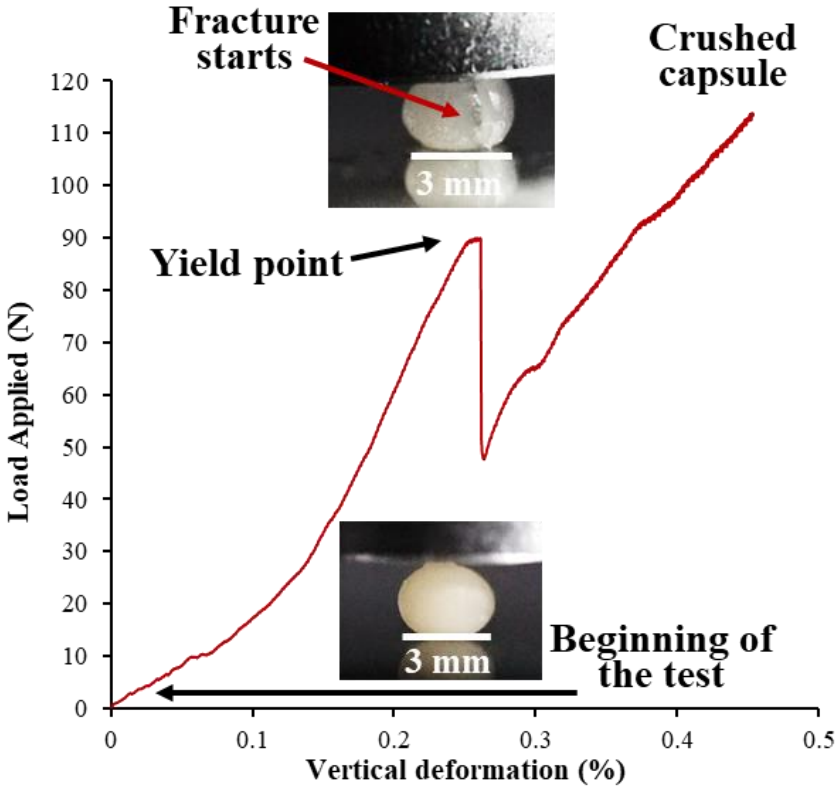


Figure 34. Different stages in a parallel compression test for a single capsule type 3-2/1

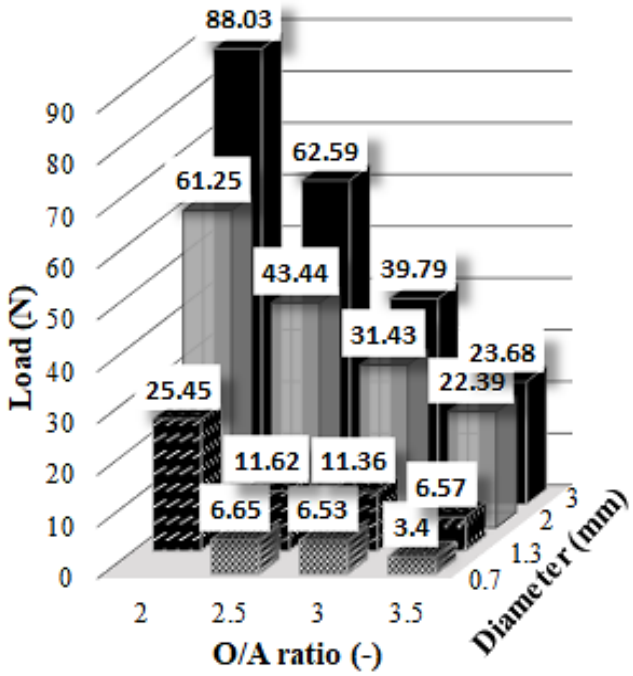


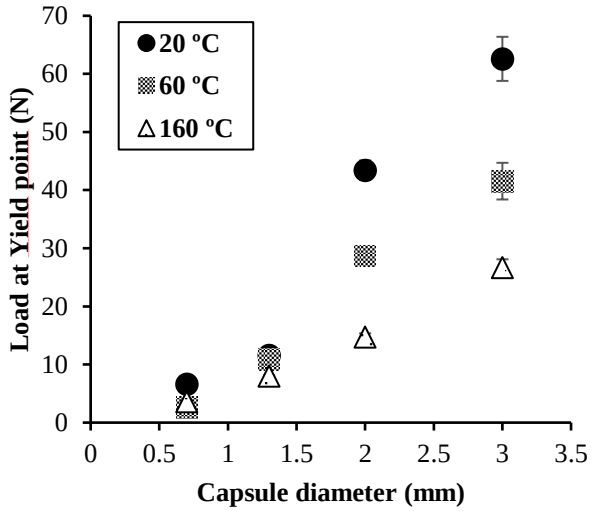
Figure 35. Load (N) at Yield point for all the capsules studied, at 20 °C.

Figure 35 shows the loads at the yield point reached by all the capsules studied. It can be observed that the capsule's strength increased with the diameter and, when the O/A ratio reduced. The strongest capsule manufactured (3-2/1) resisted 88.03 N at the yield point whereas the weakest capsule (0.7-3.5/1) resisted 3.4 N at the yield point. Based on these results, it can be expected that the capsules with a higher O/A ratio will release a higher amount of oil during the mixing and compaction process because of the stresses that these processes entail. Note that from this study it is still unclear which the optimised capsule strength will be to maximise the self-healing, since that will probably depend on the gradation of the asphalt and therefore on the capsule´s diameter. Further laboratory tests were needed to provide the type of capsule able to maximize the self-healing properties (Chapter 5).

Furthermore, Figure 36 (a) shows the results of parallel compression tests of capsules carried out at 20 °C, 60 °C and, 160 °C. The force resisted by the capsules reduces when the temperature increases, which is more evident in capsules with

higher diameter. This may be due to lower viscosity of oil at higher temperatures as there is a higher amount of oil in capsules with higher diameter, and also due to the softening of calcium alginate at higher temperatures. For example, in capsules with 3 mm diameter, the load resisted at Yield point decreased from 62.59 N at 20 °C to 26.69 N at 160 °C, 42.6 % reduction, while in capsules with 2 mm diameter, the load resisted at Yield point decreased from 43.44 N at 20 °C to 14.77 N at 160 °C, 34 %.

(a)



(b)

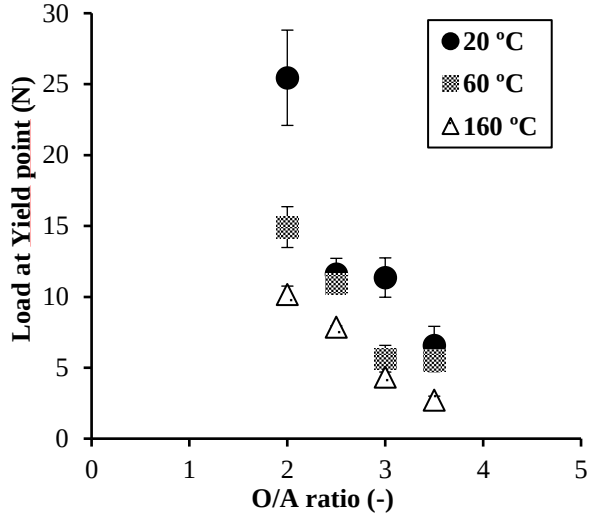


Figure 36. Yield stress at 20 °C, 60 °C, and 160 °C, of capsules with (a) a range of diameters and (b) O/A ratios.

In addition, Figure 36 (b) shows the influence of temperature in the capsules type 1.3-2/1, 1.3-2.5/1, 1.3-3/1 and 1.3-3.5/1 at the Yield point reached in the parallel plate compression test. As it is expected, the value at the Yield point of the capsules reduced when their payload or temperature increased, which may be due to the degradation of calcium-alginate, see Figure 37, or to reduced viscosities of the oil. As it was stablished in [46], the mixing and compaction generates a 10 N load over the capsules. Therefore, capsules with 0.7 mm diameter or capsules with high amount of alginate could cause and a high amount of oil released during the mixing and compaction because of their fracture. This is something to analyse by quantifying the amount of oil after the asphalt manufacturing.

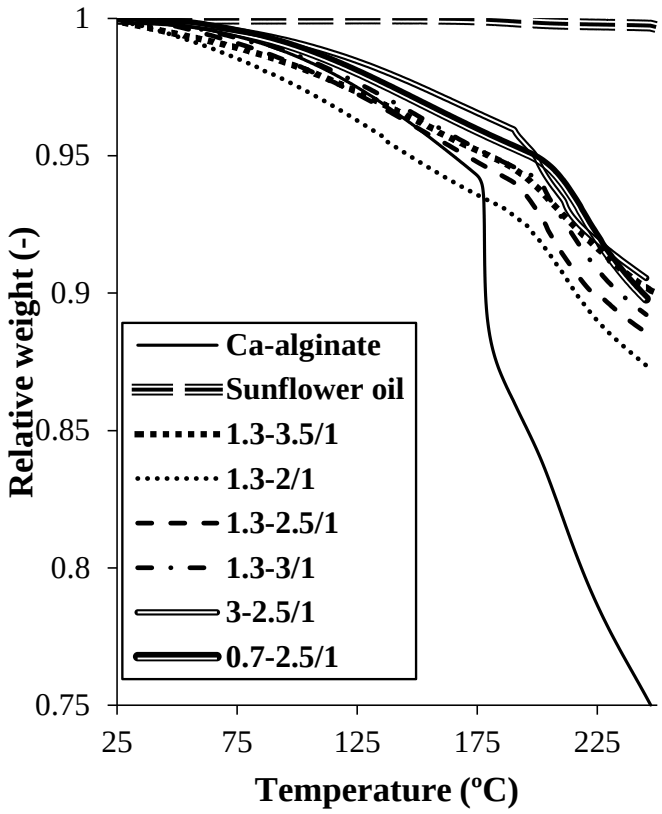


Figure 37. Thermogravimetric analysis curves for the different types of calcium alginate capsules manufactured

4.5. Thermal degradation of capsules

Figure 37 shows the thermogravimetric analysis of Ca-alginate capsules with a range of diameters and O/A ratios, in addition to the Ca-alginate and sunflower oil. It can be observed that sunflower oil showed a loss of 0.009 % of weight when the temperature was 160 °C, which is the common temperature for asphalt mixing. However, the calcium alginate showed a progressive weight loss until 6% of the total weight when the temperature is 180 °C. According to reference [13] and, as it can be observed in Figure 37, this may occur because of the evaporation of water in the mixture, which would not affect the integrity of the capsule. Above 180 °C, there is a pronounced drop in the weight loss [4]. For this reason, 180 °C can be considered the maximum temperature before the capsule's degradation. These results confirm those previously reported in [52].

Table 7 shows the weight loss at 160 °C for different types of capsules manufactured and their ingredients, Ca-alginate and sunflower oil. Regarding the influence of the diameter on the degradation, the coefficient of Pearson (Table 6) shows a slight trend between the diameter of the capsules and the degradation of the capsules at 160 °C. However, the weight loss for capsules with the lowest O/A ratio is 5.441 % whereas the weight loss for capsules with highest O/A ratio is 3.944 %. This indicates that capsules with more payload are not susceptible to thermal damage.

Table 7. Weight loss (%) for each type of capsule at 160 ^{o}C

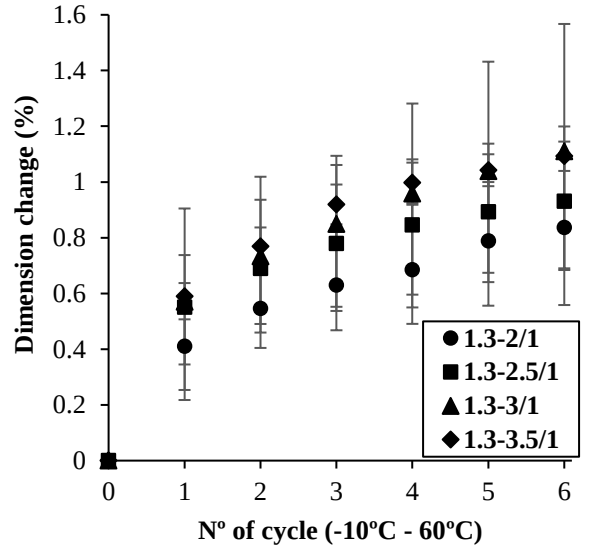
Capsule type	Weight loss (%)	O/A ratio (v%)
Sunflower oil	0.009	-
Ca-alginate	4.321	-
1.3-2/1	5.441	55.6
1.3-2.5/1	4.238	66.4
1.3-3/1	3.785	78.8
1.3-3.5/1	3.944	84.9
3-2.5/1	2.634	66.4
0.7-2.5/1	3.239	66.4

4.6. Oil release due to heating-cooling cycles. Case 1

It has been observed that the capsules may change their diameter in a permanent way due to heating and cooling cycles. For example, Figure 38 (a) shows the percentage of change in the diameter of capsules with a range of O/A ratios due to the thermal expansion. The size alteration of capsules due to temperature changes is higher in capsules with higher O/A ratio, such as 1.3-3.5/1, when the diameter may increase in about 1.09 %, or 0.0134 mm.

In addition, Figure 38 (b) shows the amount of oil released by capsules type 1.3-2/1, 1.3-2.5/1, 1.3-3/1 and 1.3-3.5/1 after the seven cycles of heating and cooling. The capsules with O/A ratio 3.5 released 12.4 % of their payload, which means 0.151 g of oil whereas the capsule with O/A ratio 2 released 2.81 % amount of their payload, which means 0.0293 g of oil. The amount of oil released is proportional to the

amount of oil in the capsules; this implies that capsules with higher oil content get more easily damaged by changes in temperature (see Table 6). On the other hand, it is clear that the capsules with higher pore size suffer more damage so, the oil released may come from the oil pockets at the surface of the capsules (see Figure 32(d)).



(b)

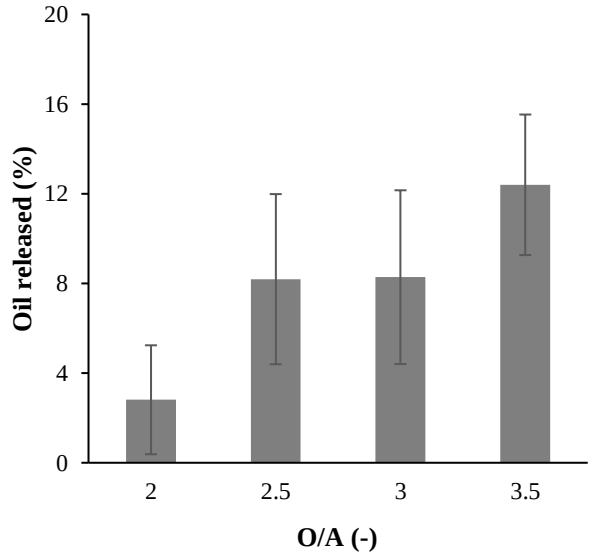


Figure 38. (a) Capsule's dimension change because of temperature changes. (b) Amount of oil released by the capsules after seven cycles of temperature change, ranging from -10 °C to 60 °C.

4.7. Release of oil by the effect of load. Cases 2, 3 and, 4.

Figure 39 shows the percentage of sunflower oil released by the 1.3 mm diameter capsules, with different O/A ratios and Cases 2, 3 and, 4. This Figure shows a clear trend between the percentage of oil released by the capsules and the O/A ratio. Those capsules that contain more oil release more oil.

The amount of oil released in Case 2 was always less than 10 % of the total amount of oil contained by the capsules. Regarding Case 3, the amount of oil released by the capsules was approximately 30 %, 30 %, 33 % and 46 % for capsules with O/A 2, 2.5, 3 and, 3.5, respectively. This is relevant, since previous research has shown that capsules may not break during the lifetime of asphalt [15] and, it could imply that less than 50 % of the oil is being used for self-healing. These results are like those obtained from the literature [51] where the percentage of sunflower oil in the bitumen was quantified after performing fatigue tests in asphalt mixtures with capsules. These results show that capsules reach the yield point when they are embedded in the asphalt and it breaks due to cyclic loading. Additionally, these results could indicate that capsules are able to heal cracks in different times of the lifespan of the road because of their progressive oil release.

Furthermore, the amounts of oil released in Case 4 were 88 %, 83 %, 93 %, 97 % for capsules with O/A 2, 2.5, 3 and, 3.5, respectively. Based on the amount of oil that capsules embedded in asphalt release at the asphalt breaking point [51], they do not get crushed. This is consistent with results shown in [6] where it was observed that the capsules looked intact after cyclic loading.

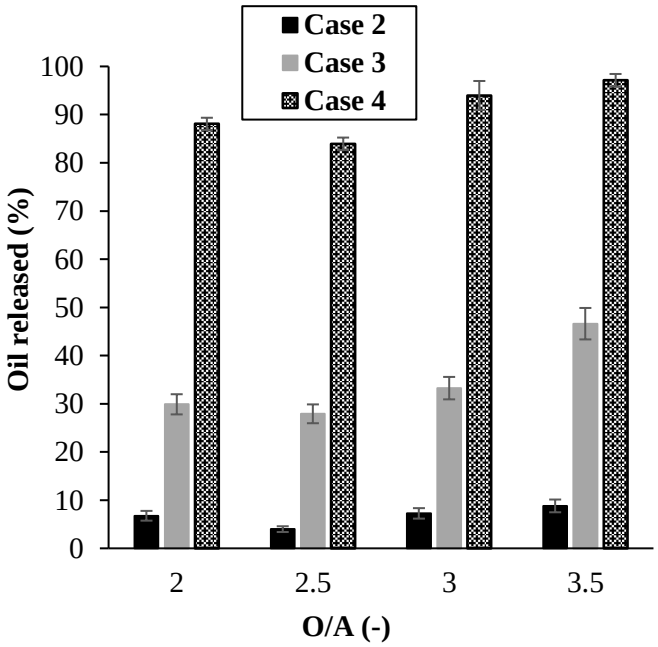
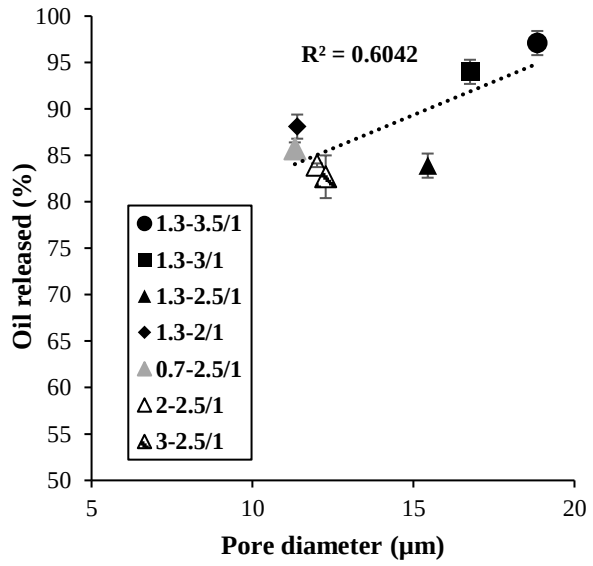


Figure 39. Percentage of oil released by 1.3 mm capsules at the different stages of a parallel compression test for different O/A ratio values

In addition, Figure 40 (a) shows the percentage of oil released by the capsules in the parallel compression test versus the pore diameter in Case 4. In general, it can be observed that the oil released is higher if the air voids are bigger. Based on the results obtained in [14], when a higher amount of capsules was broken when they were embedded in the asphalt, and therefore, a bigger amount of oil was released, the self-healing ability of the asphalt is increased. This implies that in order to get higher self-healing efficiency from the capsules, bigger pore size will be needed. This can be controlled during the emulsification phase and, will be the matter of further investigations.

(a)



(b)

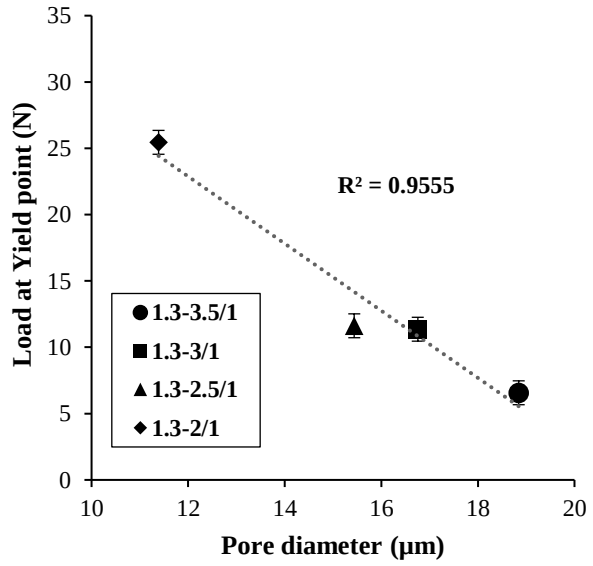


Figure 40. (a) Percentage of oil released versus pore diameter in Case 4. (b) Load resisted at Yield Point, N, versus pore diameter for the different types of capsules manufactured

Finally, Figure 40 (b) shows the relation between the pore size and the load resisted by the capsules at Yield point. Capsule type 1.3-2/1, which represents the capsule

with smallest pore size, 11.387 μm, reached 25.45 N in the parallel plates compression test whereas capsule type 1.3-3.5/1 which represents the capsules with biggest pore size, 18.845 μm, reached 6.57 N. This means a decrement in the capsule strength of 25.81 %. As it has been observed in Figure 32, the crosslinked internal structure of the capsule with bigger pore size shows lower solid structure and higher payload, which reduces its strength. Based on these results, it is expected that capsules with a high value in pore diameter, like 1.3-3/1, will show a better performance in asphalt self-healing properties due to the amount of oil released by them. At the same time capsules 1.3-3/1 showed a value for the load resisted at Yield point enough to resist the compaction and mixing processes.

CHAPTER 5

5. Optimisation of self-healing properties for asphalts containing encapsulated oil

5.1. Introduction

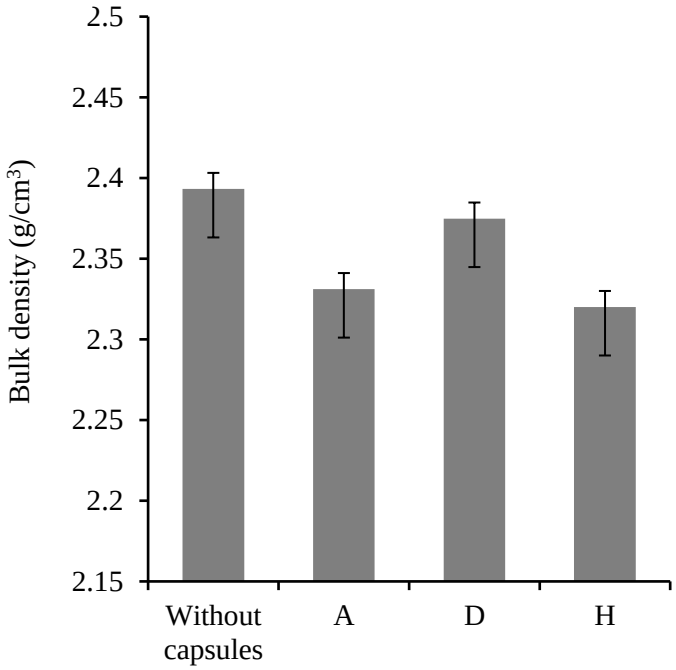
This chapter presents the results of a multivariable experimental study that aims to evaluate the influence of the capsules' size and the strength in the fatigue durability and self-healing properties of asphalt. As explained in materials and methods section, in order to reproduce the joints or discontinuities in underlying layers, which cause the reflective cracks, cyclical loads were applied over the samples by a laboratory wheel tracker. The self-healing properties of asphalt were evaluated as the extension of its fatigue durability by comparing the results of asphalt samples with capsules to those of asphalt without capsules. Moreover, the skid resistance, rutting and the amount of oil released by the capsules were analysed to validate the capsules as an effective solution for reflective cracking. Computed Tomography scanning was used to analysed changes in the internal structure of asphalt when cyclical loads are applied and, to propose a oil release mechanism. Finally, Fourier-transform infrared spectrometry was applied to measure the amount of oil released by the capsules. Promising results were obtained providing enhanced fatigue durability using capsules. Additionally, no signs of increment of the skid resistance were found and rutting increased moderately with the oil released.

5.2. Density and air void content of SMA mixtures containing capsules

Figure 41 shows the influence of the addition of capsules in the bulk density and air voids content of SMA. Three different types of capsules were analysed with different diameters and O/A (Oil / Alginate) ratios (capsule type A, D, and H, see in Table 4). The bulk density of asphalt decreased because of the addition of capsules, which have a lower density of 1.13 g/cm^3, than the aggregates 2.7 g/cm^3.

Additionally, it was already hypothesized in [52] that a reduction in the air voids content was observed when the capsules were added. This reduction could be related to the small amount of oil released by the capsules during the asphalt mixing and compaction (see Figure 50, [52]). The relation between the oil released and the rutting could indicate this effect produces higher compaction by the roller compactor used (see Figure 52, [52]).

(a)



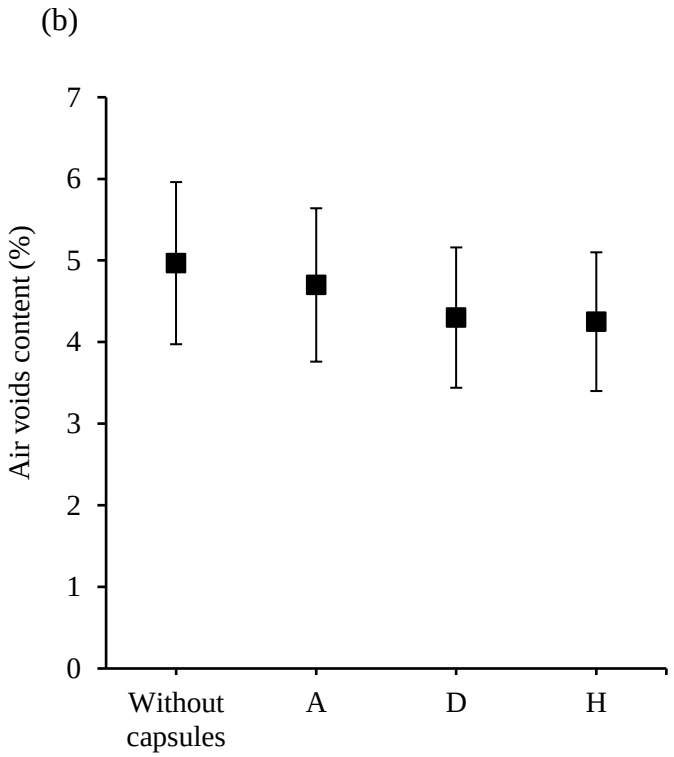


Figure 41. (a) Air voids content and (b) bulk density of SMA mixture with and without capsules

5.3. Reflective cracking repeated loading durability

Table 8 shows the median number of cycles resisted by the asphalts with all the capsules studied whereas Figure 42 shows the relation between the median number of cycles resisted by the asphalt mixtures with capsules type B, F, H and I and the diameter of these types of capsules (see Table 8).

Table 8. Median number of cycles resisted by the asphalts. Standard deviation is shown in brackets under the number of cycles.

Load (N)	Without capsules	A	B	C	D	E	F	G	H	I	J
621	5800 (24)	-	6300 (1820)	4410 (934)	-	4150 (850)	3900 (609)	5400 (773)	5310 (723)	5000 (705)	4190 (417)
723	3800 (927)	-	3660 (555)	2400 (457)	-	3000 (498)	2910 (659)	3600 (694)	3420 (246)	2600 (378)	2450 (549)
825	2600 (408)	-	2600 (530)	2250 (280)	-	1800 (399)	1600 (311)	2300 (331)	2100 (302)	2300 (241)	1600 (370)
930	1420 (371)	1565 (485)	1590 (209)	1270 (258)	1045 (264)	1249 (182)	1070 (115)	1260 (163)	1200 (163)	1400 (204)	1000 (157)
1032	670 (118)	-	820 (118)	730 (126)	-	600 (109)	600 (89)	780 (65)	600 (92)	800 (98)	720 (103)

The results shown by Table 8 refers to the fatigue durability test carried out without applying rest period in order to calculate the median number of cycles ($N_{0.5}$) for each asphalt mixture. It can be observed and enhanced performance of the capsules when the load applied is higher. These higher loads might break more capsules in early stages of the test promoting the release of the sunflower oil that could accelerate the short-term healing.

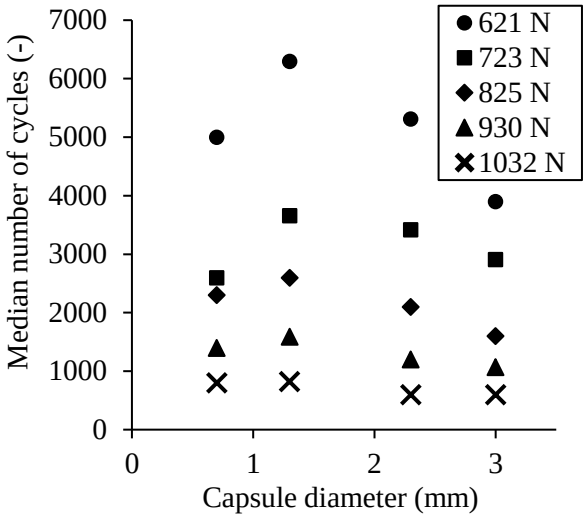


Figure 42. Influence of capsule diameter in the fatigue resistance, represented by the median number of cycles resisted by the asphalt.

Figure 42 shows that, regarding the fatigue resistance, 1.3 mm is the optimum diameter among the other diameter values of the capsules manufactured for this study. The test was performed for 5 different loads applied over the asphalt beam by the wheel of the wheel tracker, and the same trend in the relation between the median number of cycles and the diameter of the capsules was found. This indicates that 1.3 mm diameter capsules have better integration in the internal structure of the asphalt.

5.4. Optimum resting time to maximize the self-healing of asphalt

Figure 43 shows the healing index of SMA without capsules, see Figure 43 (a), and SMA mixture with capsules type C, see Figure 43 (b). These tests have been done at (i) different percentages of the median life of asphalt and, (ii) at different forces.

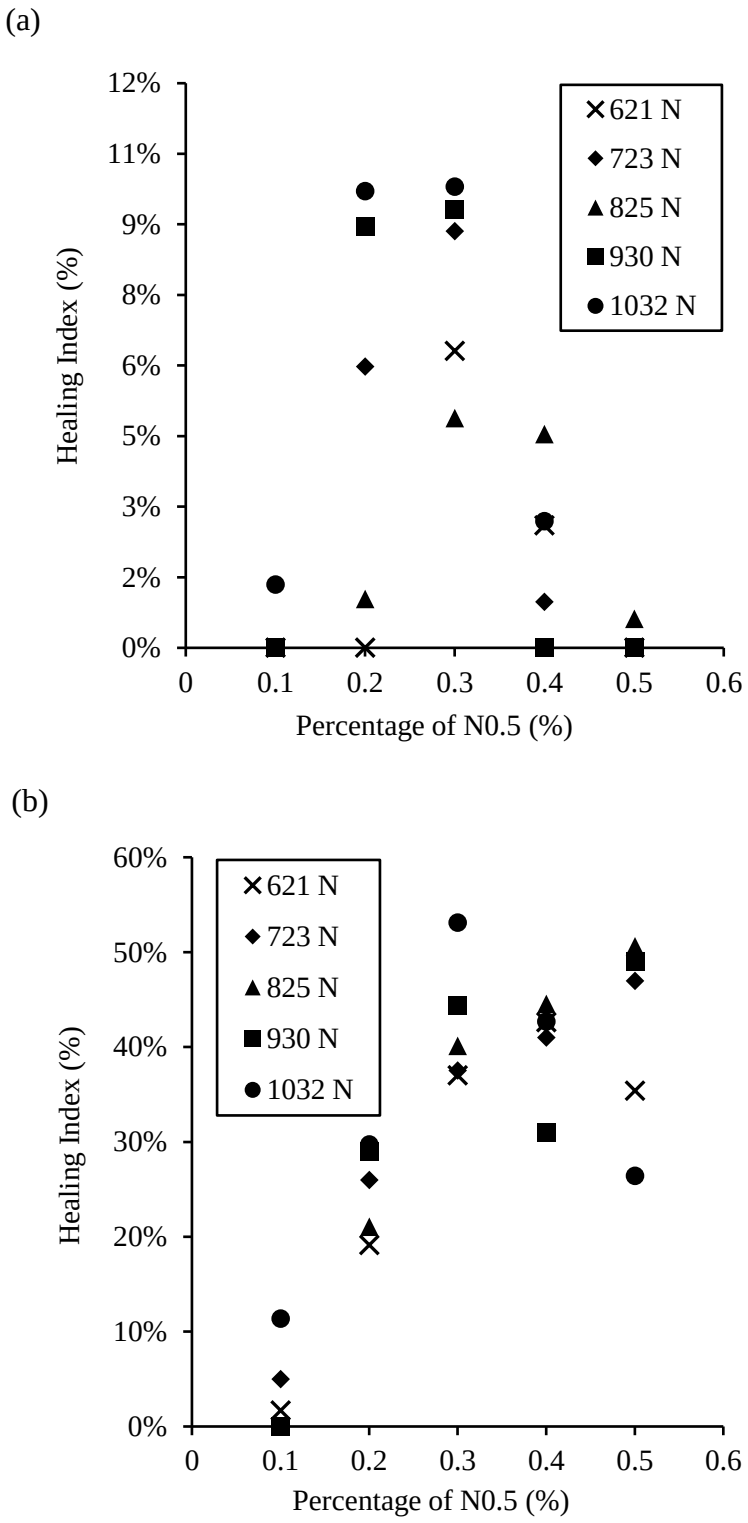


Figure 43. Healing Index at different number of loading cycles applied over the SMA beams. (a) without capsules. (b) With capsules type C

It can be observed that the highest healing index was obtained when the resting period was applied at 30% of the median number of cycles resisted for both SMA mixtures, which is independent of the load applied over the asphalt. These values are coincident with those in [5], [15], [51].

Figure 44 shows a clear relationship between the healing index and the amount of sunflower oil released by the capsules. However, a higher amount of oil released does not mean always better performance of the asphalt because it could reduce the fatigue durability.

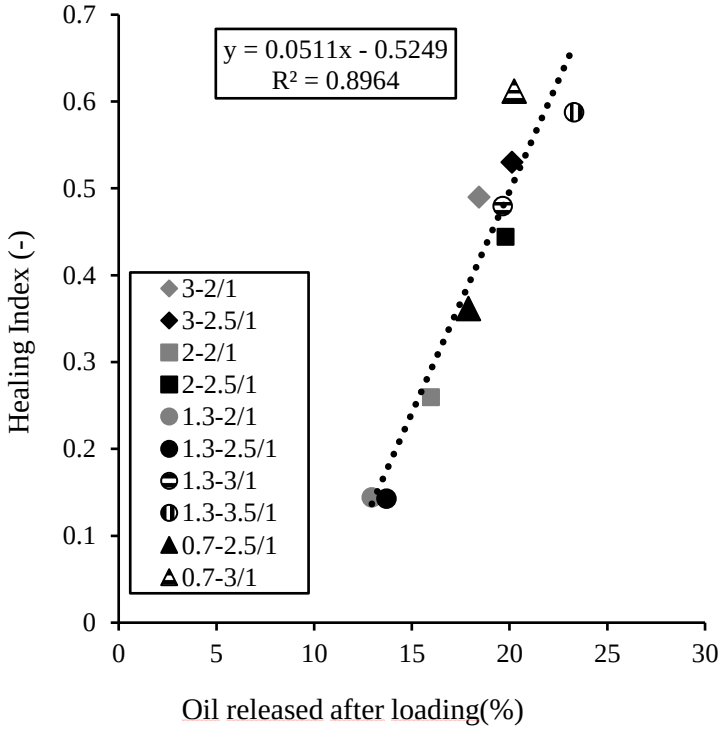
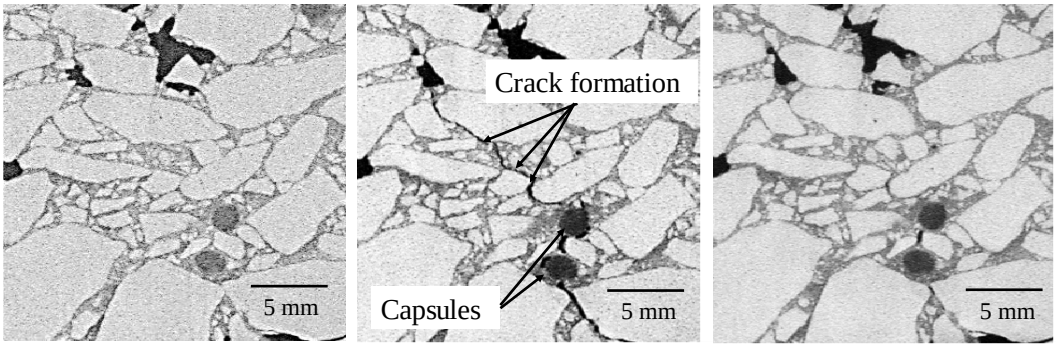


Figure 44. Relationship between healing index and amount of oil released by capsules

As it has been seen in Figure 52 and Figure 44, there is a direct relationship between the oil released, the rutting, and the increase of durability of the asphalt. Hence, it can be concluded that capsules promote rutting, which re-accommodate the aggregates and, because of this localised compaction, the cracks close. The information presented in this report does not allow to discern if the increase of

internal pressure in the mixture promotes the healing of cracks or, the movement of the wheel simply brings the faces of the cracks together. However, Figure 45 shows that a crack closes after testing and resting, without the aggregates moving, which suggests that mastic has drained from the asphalt into the crack.



(a) (b) (c)

Figure 45. X-ray tomography of the internal structure of an asphalt sample a) pre-loaded, b) after 30% of the median number N05 of cyclical loading and c) after applying resting period

If the self-healing by the effect of wheel tracking is due to the additional compaction of aggregates and the subsequent re-accommodation of mastic. 30 % of the median life is the moment when the cracks size or density allows the highest re-accommodation of aggregates, which contributed to close the cracks [6]. Besides, capsules increased the scale of the distribution. A feasible hypothesis is that capsules start release small amounts of sunflower oil at very low cycles, which promotes the re-accommodation of stones and closing of cracks. Studying the localised movement of aggregates during wheel tracking and self-healing will be a matter for future research.

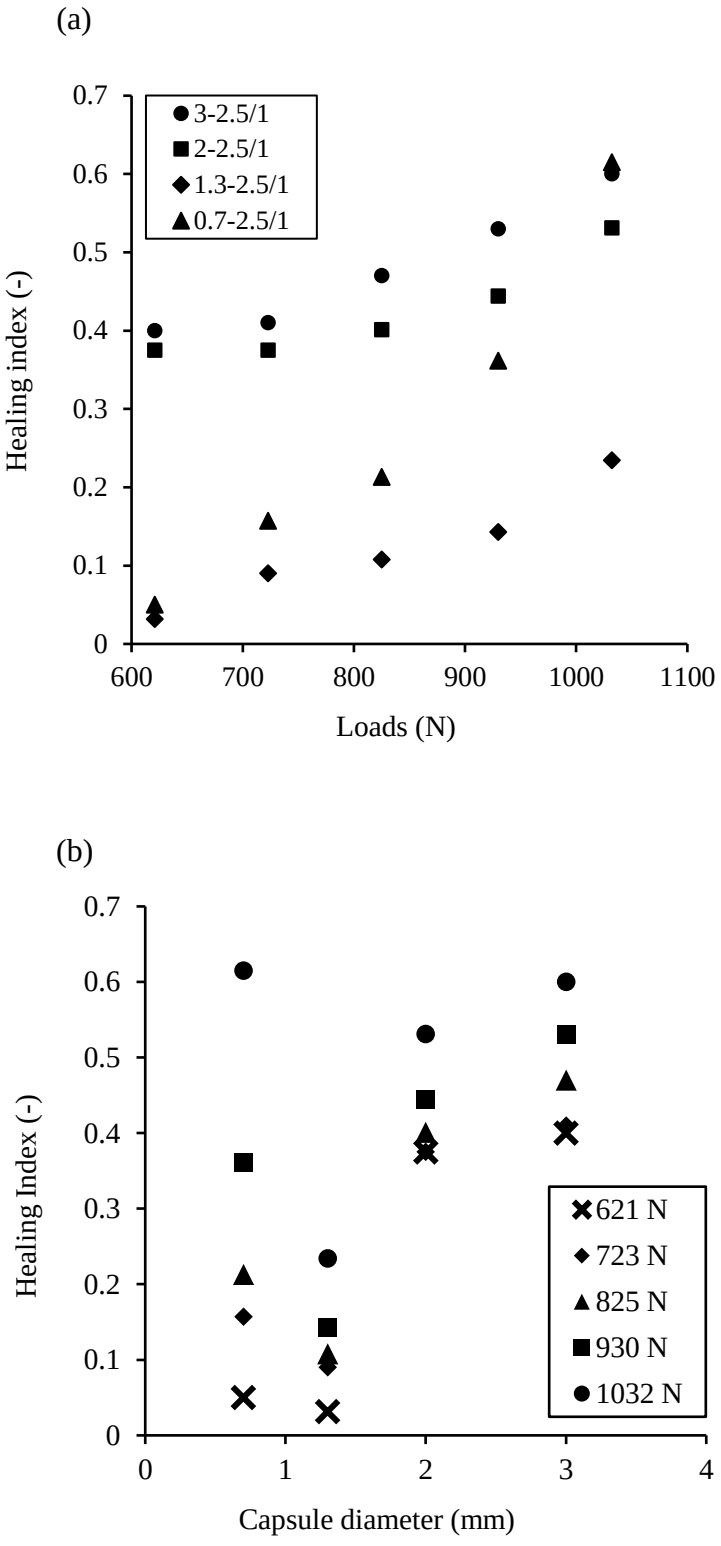


Figure 46. (a) Healing index for capsules with different diameters but the same O/A ratio. (b) Relationship between the diameter of capsules and the healing index.

Figure 46 (a) shows the healing index obtained for 4 asphalt mixtures with different a range of diameters and the same O/A ratio. The load applied by the wheel tracker influences the self-healing properties. One can easily imagine that higher load implies higher damage to the capsules, more oil released, more rutting and, improved healing index. Besides, Figure 46 (b) shows the relation between the diameter and the healing index. The bigger capsules showed the highest healing index. This can only be explained if the biggest capsules suffered more damage, and release more sunflower oil in a localised way, which could also affect the stability of the solid skeleton more. Additionally, Figure 47 also shows that smaller capsules with very low resistance can present high healing index values in comparison to the asphalt samples without capsules (for examples capsules types C and J for a load applied of 930 N). This could be related to a lower load needed to release a high percentage of oil contained by the capsules.

5.5. Influence of strength and capsules diameter in fatigue and self-healing properties

The capsules promote the self-healing of asphalt. However, they also influence the maximum number of cycles that the asphalt may resist loading, see Table 8. Hence, we must compare the total number of cycles that asphalts with and without capsules endure.

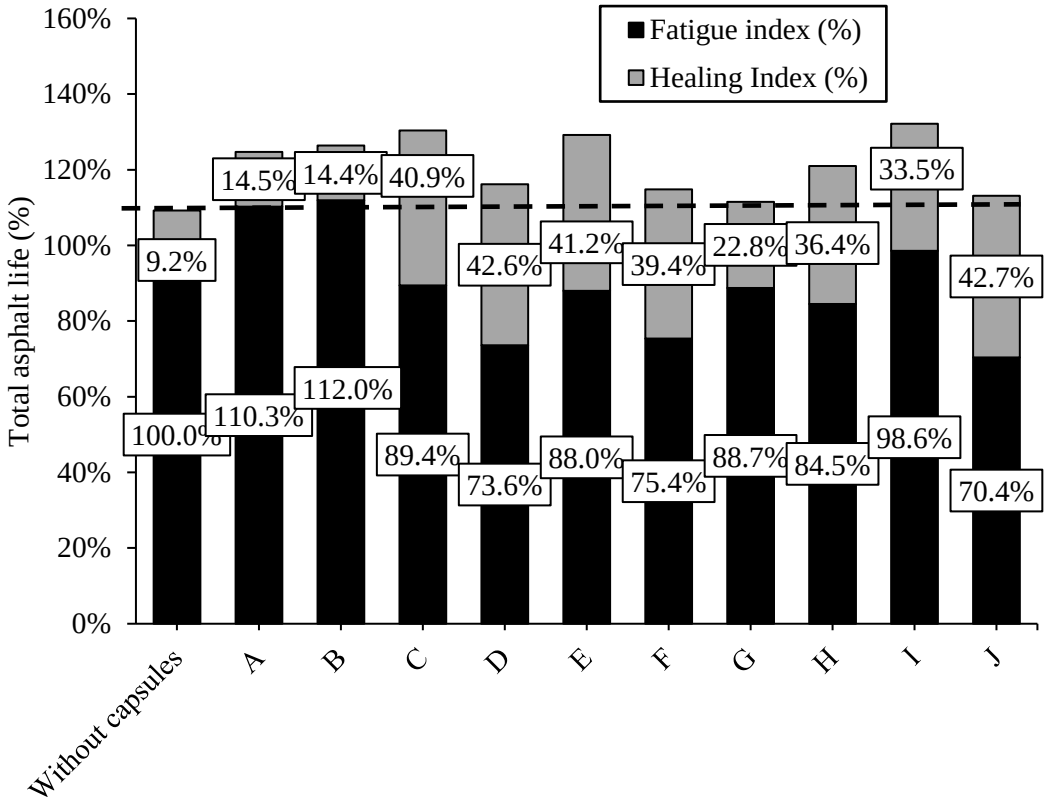


Figure 47. Final asphalt lifespan increments for all the capsules studied. 100% in the vertical axis implies that asphalt has its current fatigue life. Values higher than 100 % implies that asphalt improved durability.

Figure 47 shows the final increment in the total lifespan of the SMA mixture for each type of capsule taking into consideration the fatigue durability and the self-healing properties. It can be observed that the capsules with better performance in terms of reflective cracking durability were the capsules type 0.7 mm capsules type I, and the 1.3 mm diameter capsules, specifically type A and B which promoted self-healing and improved slightly the fatigue durability of the asphalt samples in 10.3 % and 12 %, respectively. Besides, capsules types I and C showed equivalent rutting, see Figure 52. Hence, capsules type C were selected for the asphalts since these are easier to manufacture.

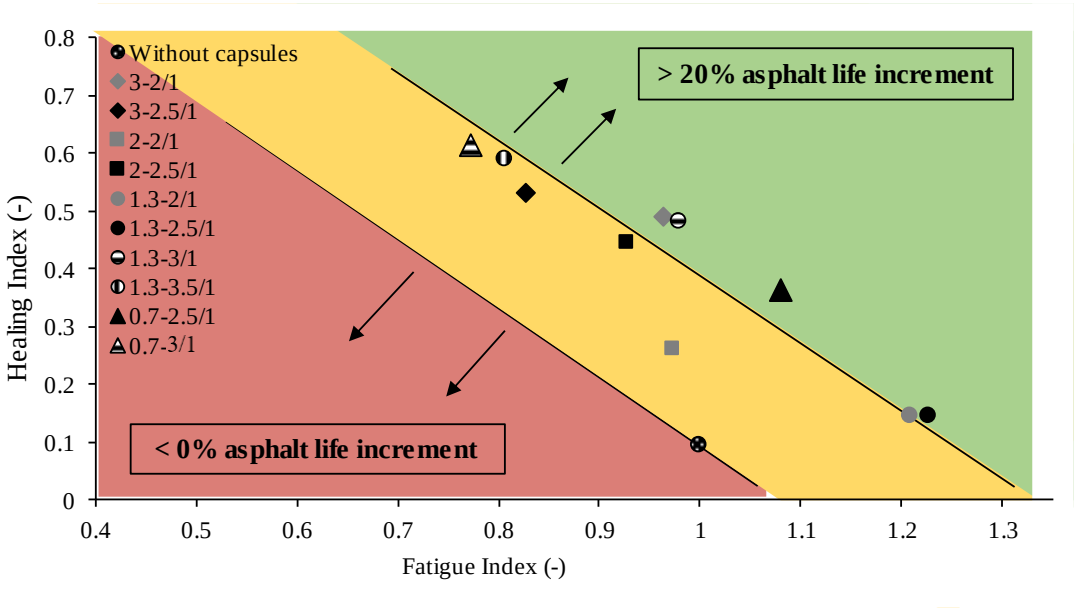


Figure 48. Healing index and fatigue index for SMA mixtures with different types of capsules

Finally, Figure 48 shows that, in general, the capsules that increase the total resistance of the asphalt to repeated loading by the wheel track, the median number of cycles (N05) show poor performance increasing the self-healing of asphalt. On the contrary, the capsules that reduce the fatigue resistance of the asphalt to repeated loading have excellent performance increasing the self-healing of asphalt. Weaker capsules release more oil, which causes rutting and helps to close cracks. However, they represent weaker areas and make the asphalt more prone to cracking. For example, in Figure 48, the capsules represented in the upper right green area increased the total durability of SMA more than 20%. The capsules in the intermediate yellow band increased the durability of the asphalt to reflective cracking between 0% and 20%. The capsules in the red area would accelerate reflective cracking of the asphalt. However, none of the capsules studied promoted cracking. The highest increment of durability was approximately 23% by capsules type I and C, in comparison to the asphalts without capsules.

5.6. Capsule oil release mechanism in asphalt mixtures

The authors have investigated the percentage of oil released by the capsules, since this may influence the crack self-healing, increase rutting and reduce skidding resistance.

Figure 49 shows the details of the structure of the capsules that have been used. Figure 49 (a) presents a 3D reconstruction of a cut from capsule type H extracted from an asphalt mixture just after the mixing and compaction processes. It can be seen that the oil is contained in a continuous porous matrix. The capsule that is shown in Figure 49 (b) is another capsule type H extracted from an asphalt sample which was cyclically loaded. It can be observed a large void inside the capsule in comparison to the pores presented by the capsule in Figure 49 (a). This could indicate the fracture of some internal alginate matrix walls during the asphalt loading.

Figure 49 (c) is the image of the surface of another capsule type H extracted from an asphalt mixture after mixing and compaction processes. As it was mentioned in [135] the surface of the capsules after mixing and compaction presents some small oil reservoirs broken which is related to the amount of oil found in the bitumen presented in Figure 50. Figure 49 (d) presents the image of another capsule type H extracted from and asphalt beam after applying cyclical loading. It was observed some damage at the capsule surface which seems to indicate it was compressed by the aggregates presented in the asphalt beam during the cyclical loading. This could be related to the higher amounts of oil released by the capsules after applying cyclical loading presented in Figure 50.

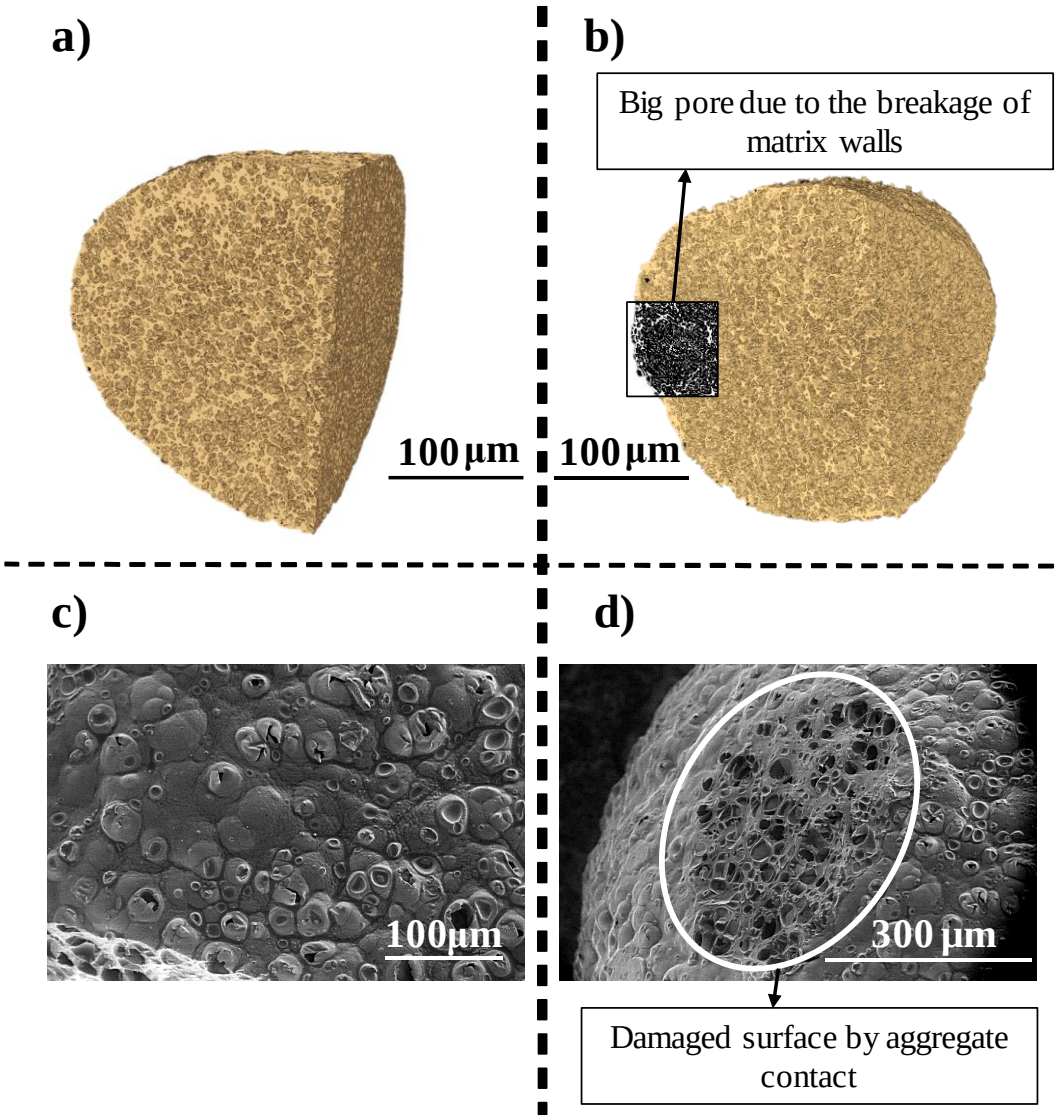


Figure 49. 3D reconstruction and microscope surface's detail of a capsule type H extracted (a) after mixing and compaction and (b) after cyclical loading. SEM microscope images are taken of a capsule type H (c) after mixing and compaction and (d) after cyclical loading

Figure 50 shows the percentage of sunflower oil released by different capsules (types A, B, C and D), with an equivalent diameter (1.3 mm) but different O/A ratio after (i) asphalt mixing and compaction, (ii) 930 N cyclical loading to 30% of N0.5 by the laboratory wheel tracker and, (iii) at the yield point of the capsule in a parallel compression test. It can be observed that the amount of oil released by the capsules during the mixing and compaction of asphalt is less than 1 % [52]. The measurement

of the amount released for each one of the cases was described in Chapter 3. This amount of oil can be released by small reservoirs of oil in the surface of the capsules, seen in the detail of Figure 49 or by capsules that have been damaged during mixing and compaction [15].

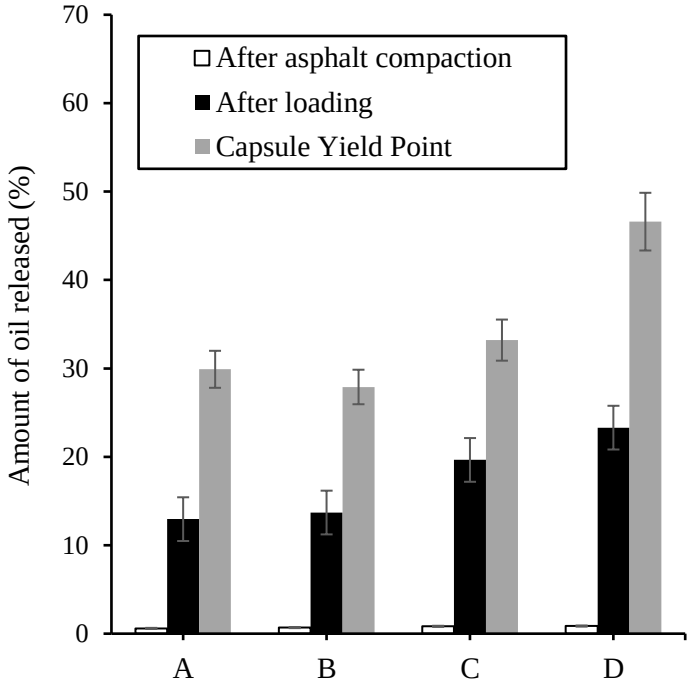


Figure 50. Amount of oil released by capsules with different O/A ratio

Furthermore, the amount of sunflower oil released just before the resting period, 30 % of the median number of cycles to reflective cracking, was 15-20 % lower than the amount of oil released by the capsules when they reach the yield point. This indicates that the capsules are not reaching the yield point at 30 % of N0.5. Besides, capsules type D, which are those that contained more oil; they released 23.3% of the total contained. For the first time, the effectiveness of a capsule for self-healing asphalt was quantified obtaining a maximum of 23.3% of efficiency. As an illustration, Figure 49 (b) shows the internal structure and surface of a capsule type H, extracted from the asphalt after 30 % of N0.5 cycles. In the 3D reconstruction, it can be observed that pores burst and generated bigger cavities. It can also be seen

that the surface of the capsules became damaged, possibly due to the cyclic wearing against the aggregates. This implies that the oil was released in the contact points with aggregates.

5.7. Effect of the oil released on the skidding resistance

The loss of the skidding resistance due to consequence of the sunflower oil released by the capsules is one of the main worries of road owners concerning asphalts with encapsulated rejuvenators. To answer this question, skid resistance tests were carried out for SMA mixtures with each type of capsule manufactured.

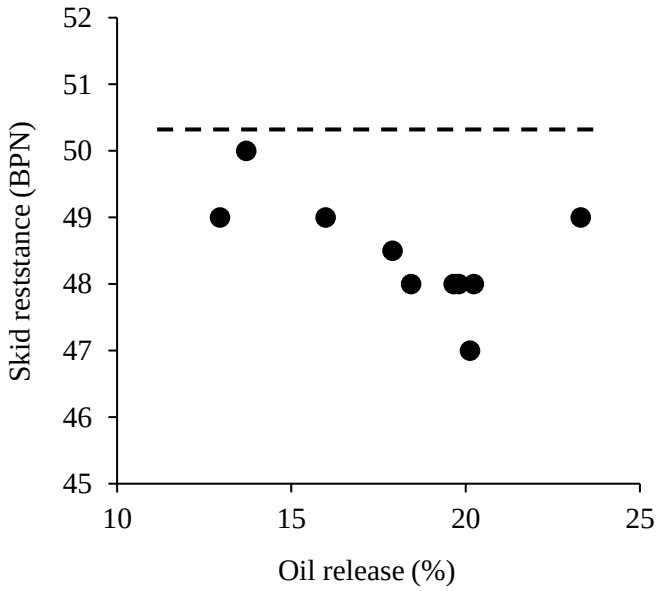


Figure 51. Skid resistance for the SMA mixtures studied

Figure 51 shows the skid resistance obtained from SMA samples with and without capsules, after testing the asphalt at 30 % of the median number of cycles to reflective cracking. There is not a clear trend between the amount of oil released and the skidding resistance. The skid resistance showed by the asphalt without capsules was 50 BPN whereas the average skid resistance value was 47 BPN, with a standard

deviation of 2.37. Similar values were obtained in [51], concluding that a difference of 3.4 BPN between the skid resistance of an asphalt mixture with capsules and without capsules was not significant to produce a real risk of skidding on the surface of the asphalt.

5.8. Effect of the oil released on the rutting effect

Higher temperatures or the addition of bitumen rejuvenators can cause rutting [16]. The same applies to the oil released from the capsules, for example, reference [16] showed an increased rutting depth when the number of capsules in the asphalt increased. However, the influence of capsules morphology on the rutting has never been discussed and, will be a subject of future investigation.

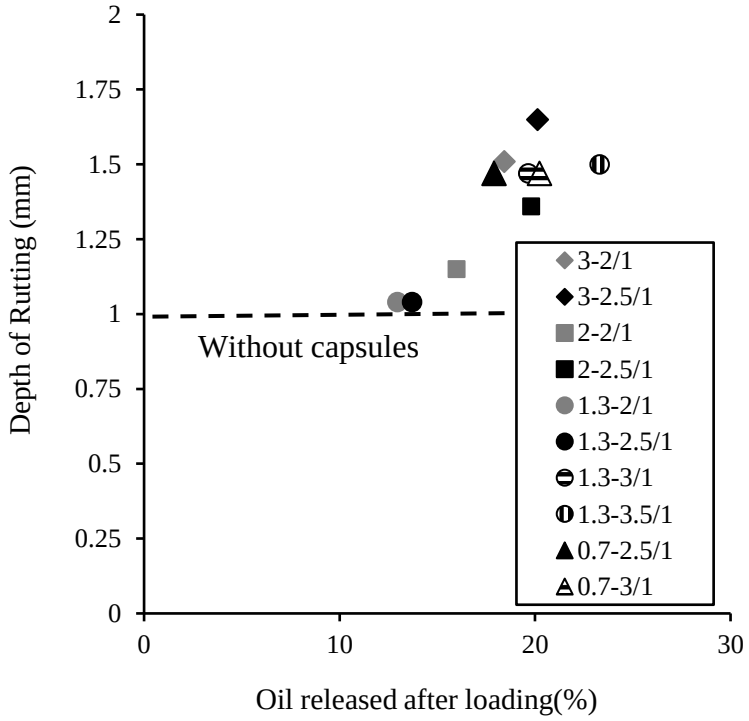


Figure 52. Relationship between the depth of rutting and the amount of oil released by the different types of capsules manufactured.

Figure 52 shows the relationship between the depth of rutting obtained versus the oil released after testing the asphalt wheel track at 30 % of the median number of cycles to reflective cracking. Confirming the results from previous research, rutting grows with the percentage of oil released from the capsules. The curve from Figure 52 has two horizontal asymptotes. The lower one, which corresponds to the rutting of asphalt without capsules and, the higher one, which is determined by the solid skeleton of the asphalt and reflects the binding properties of the bitumen.

Rutting grows with the amount of oil released by the capsules. For example, the highest value of rutting (1.65 mm) occurs with capsules type F, which released 20.12 % of their oil, the second higher amount in the report. While it does not exist a direct observation of this, it cannot be avoided to think that a higher oil release will ease the movement of stones around the capsule, which will promote rutting up to a certain level.

CHAPTER 6

6. Computational simulation of fluid-structure interaction and breakage of capsules.

6.1. Introduction

In this chapter, DMP is used to simulate a 3D elastic core–shell capsule breaking under compression and releasing its internal liquid into the environment. This is one of the first models capable of simulating this phenomenon. The proposed model is an extension of [136], but, in this case, rupture occurs by direct compression of the capsule rather than as a result of shear flow. The computational results were validated by comparing the type of fracture of the capsule and the force/displacement relationship with experimental data for elastic core–shell capsules available in the literature [137]. DMP can effectively reproduce the deformation and the fracture of the capsule. The model was used to study the influence of the shell's Young's modulus and thickness on the force/displacement relationship and on the type of fracture to show how the proposed model could have a significant impact on the design of capsules [86].

6.2. Modelling approach

The version of DMP used in this paper (Figure 53) couples SPH and the LSM. SPH was used to model the fluid, and LSM was used for the solid. Details on these models and how they were coupled together are given in this section.

6.2.1. Smoothed Particle Hydrodynamics (SPH)

The general idea of SPH is to approximate a partial differential equation over a group of movable computational particles that are not collocated over a grid or a mesh [129], [138]. Each particle has an associated mass, momentum, and energy and the motion of the particle is calculated by integrating Newton's second law. Particle properties such as density, velocity, energy per unit of mass, pressure, or heat flux are obtained by interpolating neighbouring particles by means of:

$$f(\mathbf{r}) \approx \iiint f(\mathbf{r}')W(\mathbf{r}-\mathbf{r}',h)dr' \tag{8}$$

where $f(\mathbf{r})$ is a generic property defined over the volume, $\mathbf{r}$ is the position vector where the property is measured, W is the so-called Kernel function, and h is a smoothing length [138]. In this specific study case Lucy kernel equation was used [139]. The Navier–Stokes equation, for instance, can be discretised over a series of computational particles, obtaining:

$$m_i \frac{dv_i}{dt} = \sum_j m_i m_j \left(\frac{P_i}{\rho_i^2} + \frac{P_j}{\rho_j^2} + \sqcap_{i,j}\right) \nabla_j W_{i,j} + \sum F_E \tag{9}$$

where P is the pressure, t represents time, v is the velocity, m is the mass, ρ is the density associated with particles i and j, and F_E refers to the external forces acting on the fluid (e.g., gravity). The viscosity term ($\sqcap$) used in this study is defined in [140]. Equation (9) requires an equation of state that relates density and pressure. In this work, we used Tait's equation [141]:

$$P(\rho) = \frac{c_0 \rho_0}{7}\left[\left(\frac{\rho}{\rho_0}\right)^7 - 1\right] \quad (10)$$

where c_0 is a reference speed of sound and ρ_0 is a reference density. To ensure weak compressibility, c_0 was chosen to be at least 10 times larger than the highest fluid velocity.

Π_{ij} in Equation (9) introduces the viscosity tensor; here, we used the so-called artificial viscosity [30], defined as:

$$\Pi_{ij} = -\alpha h \frac{c_0}{\rho_{ij}} \frac{v_{ij} r_{ij}}{r_{ij}^2 + bh^2} \quad (11)$$

where $v_{ij} = v_j - v_i$ and $\rho_{ij} = \rho_j + \rho_i$. The dimensionless parameters α and b ensure the stability of the simulation. In our case, b = 0.01, while:

$$\alpha = \frac{8v}{hc_0} \quad (12)$$

where v is the kinematic viscosity. At each time step, the local density is updated according to the partition of unity equation [140]:

$$\rho_i = \sum_j m_j W_{i,j} \quad (13)$$

6.2.2. Lattice Spring Model (LSM)

The LSM was used to model the shell of the capsule. Here, only a very general introduction to LSM is given; for additional details see [142]. The computational particles that constitute the solid shell are linked together by spring-like bonds and their trajectories calculated with the Newtonian equations of motion:

$$m_i \frac{d^2 r_i}{dt^2} = -\frac{\partial}{\partial r} U_{tot}(r_1, r_2, \ldots r_N) + \sum F_E \quad (14)$$

where U_{tot} is the potential used to model the bonds between interconnected particles. In this study, linear spring was used, which corresponds to the harmonic potential:

$$U_{bond} = k_b(r - r_0)^2 \quad (15)$$

where r_0 is the equilibrium distance and k_b is the Hookean constant. The Young's modulus of the materials relates to k_b, as explained in Section 2.3.

Equation (15) represents the forces that maintain two particles at a specific distance (r_0). The distribution of the shell's computational particles is determined by defining a quadratic mesh (see Figure 53) over an empty sphere with external diameter 3.1×10^{-5} m and an internal diameter of 2.6×10^{-5} m. Nearest neighbour particles and next-nearest neighbour particles are linked with computational springs. Breakage is simulated assuming that, if the distance between two particles exceeds a maximal value (r_{max}), the bond is broken and the two particles separated (Figure 54).

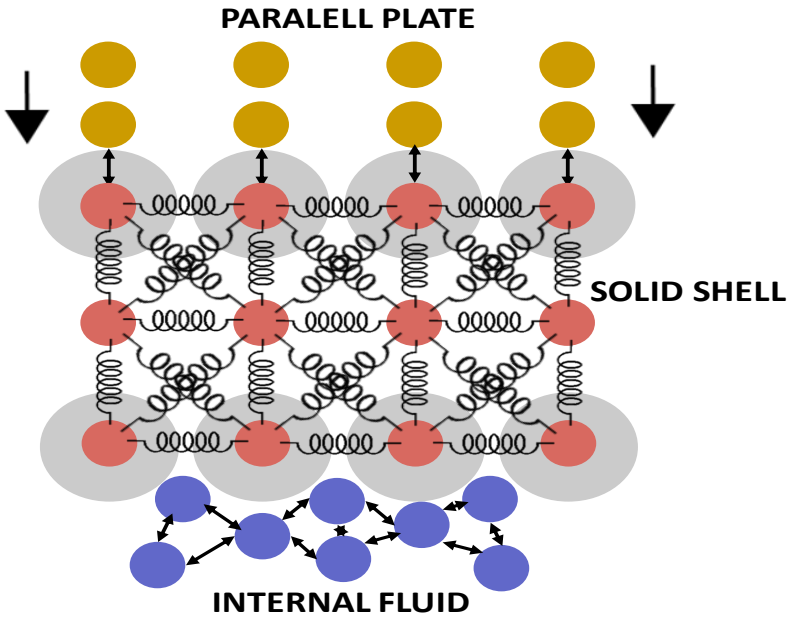


Figure 53. Particle representation and interactions among the computational particles.

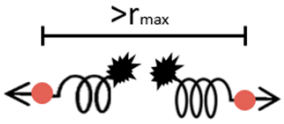


Figure 54. Representation of two computed particle bonds breaking.

How k_b and r_{max} are calibrated to reproduce the capsule mechanical properties is discussed later on.

6.2.3. Coupling the Two Models

Besides the interaction between two liquid particles (model with SPH) and two solid particles (model with LSM), the model also requires specifying the interaction between liquid and solid particles that occurs at the solid–liquid interface. Here, only a general introduction to coupling SPH and LSM is given; for more details, see [113]. In continuum mechanics, three conditions must be satisfied:

$$\left(\frac{\partial}{\partial t}\mathbf{u} - \mathbf{v}\right) \cdot \mathbf{n} = 0 \text{ (no penetration condition)} \tag{16}$$

$$\left(\frac{\partial}{\partial t}\mathbf{u} - \mathbf{v}\right) \times \mathbf{n} = 0 \text{ (no slip condition)} \tag{17}$$

$$\sigma_s \cdot \mathbf{n} = \sigma_f \cdot (-\mathbf{n}) \text{ (continuity of stresses condition)} \tag{18}$$

where **n** is the vector normal to the boundary, **u** is the displacement of the solid, **v** is the velocity of the liquid, and σ_s is the stress tensor in the solid and σ_f in the fluid. The advantage of using a particle method is that we only solve the Newton equation of motion for every particle. The only difference is in the force acting on the particle. Equations (16)–(18) are no exceptions. They do not need a special treatment, but only forces that replicate the effect of the boundary conditions. For Equation (16), this is achieved by using the repulsive potential of the type:

$$E_r = \epsilon \left[\left(\frac{\sigma}{r}\right)^a - \left(\frac{\sigma}{r}\right)^b\right] \; r < \sigma \tag{19}$$

where the constants ϵ, σ, a, and b are given in Table 9. This repulsion force does not influence the simulation itself. It is only used to avoid particle compenetrating and its parameters are determined to achieve this goal without requiring a smaller time step. The cut-off $r < \sigma$ in Equation (19) ensures that, when the particles are not in contact, the force is zero. The parameters in Equation (16) were chosen by trial and error to guarantee no penetration without decreasing the timestep. If the repulsion

potential is too weak, fluid will penetrate inside the solid; if it is too strong, the simulation will require small timesteps to remain stable.

Table 9. Parameters needed for Discrete Multi-Physics simulation.

SPH	
Number of SPH fluid particles	5731
Mass of each particle, m	2.7×10^{-15} kg
Initial distance among particles, dL	1.24×10^{-6} m
Smoothing length, h	$1.1 \cdot dL$
Artificial sound speed, c_0	1.1 m s^{-1}
Density, ρ_0	900 kg m^{-3}
Viscosity, μ_0	0.001 Pa·s
LSM	
Number of particles (shell)	5604
Mass of each particle	2.7×10^{-15} kg
Hookean coefficient, kb	4.6 N m^{-1}
Maximum distance for fracture, r_{max}	1.2 r_0
Shell thickness, t_0	2.5×10^{-6} m
Capsule diameter	31×10^{-6} m
BOUNDARIES	
Repulsive potential constant, ϵ	5×10^{-15} J
Repulsive radius, σ	$1.1 \cdot dL$
Repulsive coefficient, a	1
Repulsive coefficient, b	0

No-slip conditions are modelled by superimposing virtual fluid particles above the solid particles at the interface, providing zero relative velocity at the solid–liquid boundary for the liquid particles that interact with the interface. Finally, in particle methods, the continuity-of-stress is automatically satisfied (it is a consequence of the law of action–reaction) and does not require to be specificity implemented.

The calculations were carried out with LAMMPS, a molecular dynamics software package that also accounts for other particle methods, such as SPH. The reader is referred to [143], [144] for additional details on the numerical formulations and schemes used in the simulation of, respectively, the structure and the fluid.
The model does not account for temperature changes. However, this can be easily implemented in DMP [128].

6.3. Geometry

The starting geometry in the simulations was a three-dimensional single liquid core capsule with a diameter of 0.031 mm. As the purpose of this simulation was to simulate compression of single particles between two parallel plates, the drivers were defined as rectangular geometries that apply force to the capsule. The parallel plates were modelled with solid particles (Figure 55). The lower plate was stationary, while the upper plate moved as a rigid body under the effect of an applied force that compressed the capsules during the compression test.

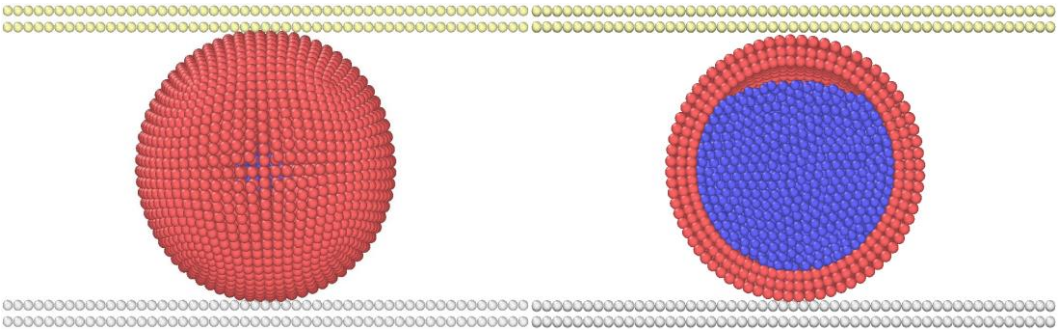


Figure 55. Initial simulation geometry.

Figure 55 shows the geometry of the shell and the parallel plates at the beginning of the simulation. A transversal cut of the capsule shows the fluid particles inside the capsule. In order to prevent penetration, repulsive forces were used between the fluid and the shell, the fluid and the plates, and the shell and the plates by applying no-penetration and no-slip boundary conditions, as explained in the previous section.

The shell was built with three particle layers. Simulations with additional layers (i.e., more particles) were carried out and show similar results. In this study, we only considered elastic capsules. Viscoelastic can be modelled by implementing the method proposed in [145]. From Figure 55, it can be appreciated that the shell was not completely filled with fluid. The empty space was created by the small deformation of the capsule due to gravity and the resulting settling of the fluid particles. In theory, it is possible to add more particles to replenish the capsule. However, we decided not to do this, since the same phenomenon can also occur in real particles. This space is normally within 1%–2% of the total volume. We verified that within this range, and the results were not affected.

6.4. Main Simulation Parameters

The parameters used in the simulations can be divided into three groups (i.e., SPH, MSM, and boundaries) and are shown in Table 9.

The parameter that determines the elastic behaviour of the model is k_b, the Hookean coefficient of the computational springs. The actual Young's modulus of the capsules can be calculated from compression experiments with the technique proposed by Yap et al. [146]. In our case, it corresponds to E = 4.85 MPa. Once the Young's modulus is known, the value of k_b can be calculated with the following equation [120]:

$$k_b = \frac{6Et_0}{3n\sqrt{3}} \tag{20}$$

where E is the Young's modulus, t_0 is the thickness of the shell of the capsule, and n is the number of layers of the shell. The timestep used in the simulation was $\Delta t = 1 \times 10^{-10}$ s. We carried out a sensitivity analysis of the results with the timestep to make sure the results were independent of the timestep adopted.

The parallel plates applied a progressive pressure to the capsule until the capsule broke, replicating the experimental conditions. From the simulations, therefore, we

can plot the force–displacement data and, for validation purposes, compare the plot with that obtained from the experiments.

6.5. Parametric Study and Influence of k_b and r_{max}

The capsule's deformability and strength are governed by two parameters: the Hookean coefficient of the computational springs (k_b) and the maximum distance between solid particles after which the computational spring breaks (r_{max}). In order to analyse the influence of these parameters on the deformability, strength, and type of fracture of the capsule, the main simulation, fitted to the experimental force–displacement curve, was assessed in 9 different simulations modifying k_b (1.56, 4.67, and 14 N m^{-1}) and r_{max} ($1.03 \cdot r_0$, $1.2 \cdot r_0$, and $1.27 \cdot r_0$) values. Many other authors have applied similar methodologies in order to perform sensitivity analysis in different fields [147]–[150].

6.6. Validation of the Simulation of Capsule Compression between Two Parallel Plates

A parallel compression test of a single core–shell capsule under compressive load was reproduced in the simulations. The force–displacement curve obtained from these simulations was compared to the corresponding data obtained experimentally [137] for a core–shell with the same size and internal structure. For validation purposes, we compared the results with only one type of capsule available in the literature [137]. However, it must be noted that the parameters k_b describing the mechanical properties of the capsule are calculated by first-principles Equation (20), and are not the result of fitting a free parameter to the experimental data.

In order to determine the optimal resolution of the core–shell model, various simulations with an increasing number of computational particles were compared. Each simulation had a different layer used to model the shell. The best compromise between accuracy and computational times was found with three layers. Figure 56 compares the force–displacement curve obtained with the model and with the experiments. Furthermore, an additional simulation with the capsule without fluid inside was carried out in order to understand the influence of the fluid on the capsule´s strength.

The results show that the compression can be divided into three regions: (i) an elastic region where the force is proportional to $\delta^{3/2}$ (where δ is the displacement), as predicted by Hertzian theory, and all of the load is supported by the external shell; (ii) an inelastic region where the stress reaches the fluid that adds additional resistance to the compression; (iii) a final region where the capsule breaks and collapses.

These three different stages were observed in both the experimental and the DMP force–displacement curves. The DMP results are very similar to the experimental results and reached the same maximal force required to break the capsule. The force–displacement curve from the simulation of the shell without fluid shows a completely different shape, which indicates that the internal fluid affects significantly the deformation of the capsule, especially at high deformations. It is important to highlight that the model does not account for plastic deformation. Locally, the rupture of every single bond was "fragile." However, this still produced a gradual rupture at the global level. In Figure 56, for instance, we defined the region before the rupture as "inelastic" because we did not observe capsule break-up. However, some of the bonds in the solid structure began to rupture, weakening the structure and producing the observed inelastic behaviour.

Figure 57 shows that the DMP model is consistent with the fracture and the capsule deformation for different coaxial load values applied during the compression test of the real capsule tested in the laboratory [137]. In order to save computational time, the resulting speed of the driver was higher in the simulations shown in Figure 57. However, quasi-static conditions were verified by carrying out simulations at

different driver speeds, enabling a comparison between the force–displacement curves.

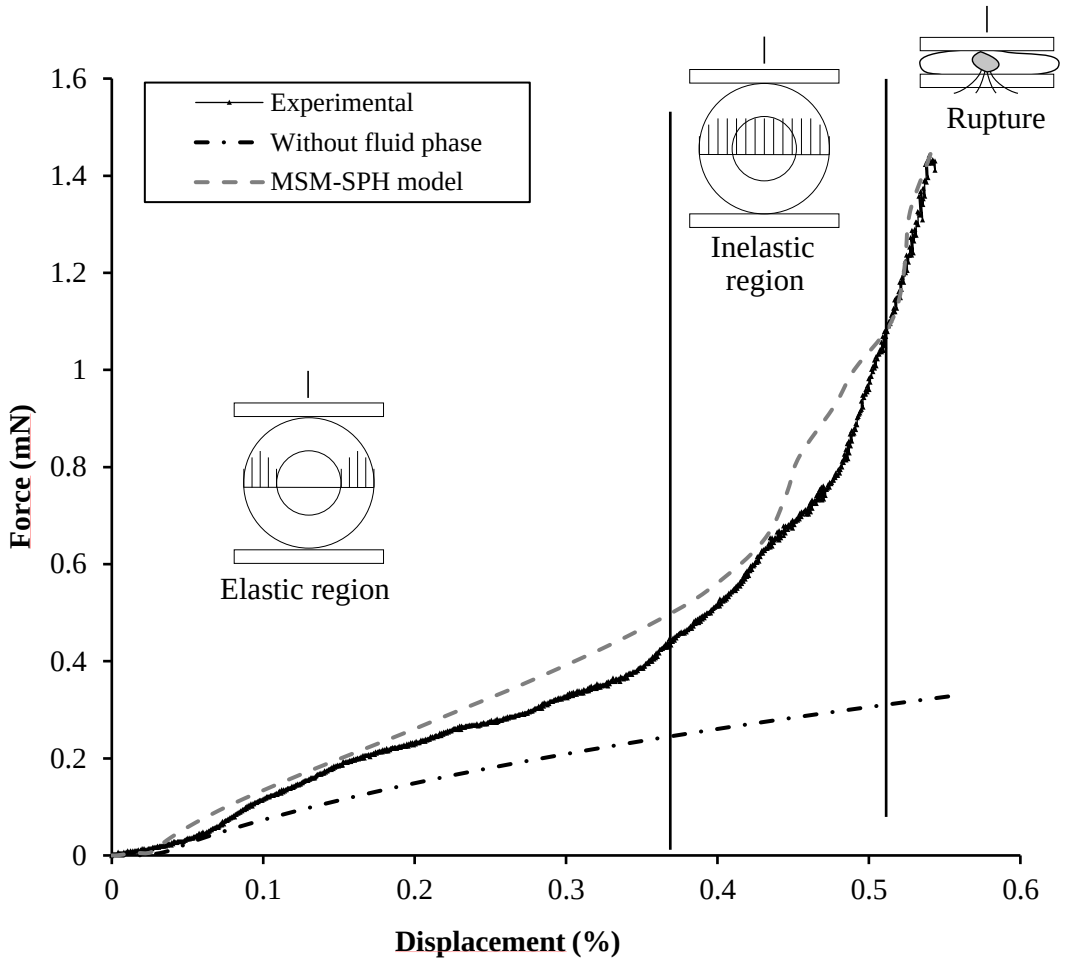


Figure 56. Force–displacement curve obtained from a laboratory parallel plate compression test for a single core–shell capsule, from a simulated single core–shell capsule without fluid inside and from a simulated single core–shell capsule.

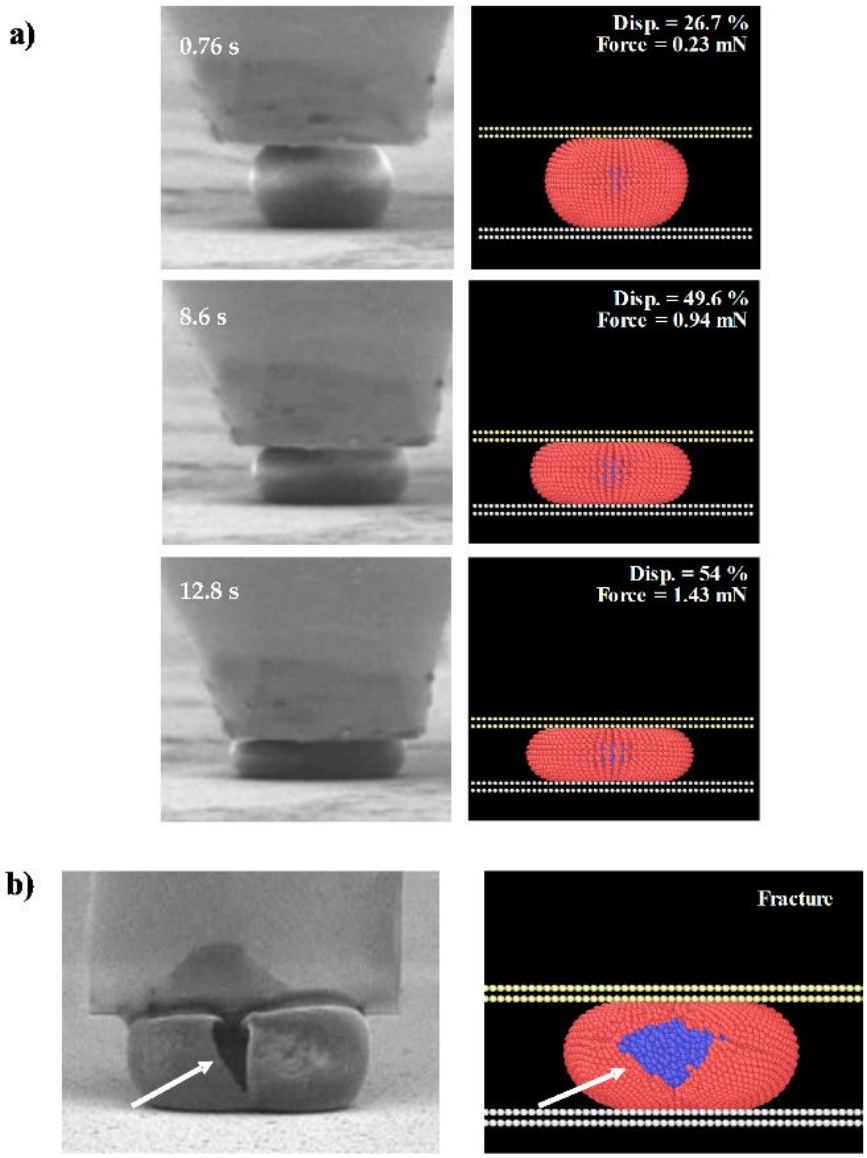


Figure 57. (a) Comparison between the deformation under coaxial load and (b) the fracture of a simulated elastic single liquid core–shell capsule by the Discrete Multi-Physics (DMP) approach and an elastic capsule of 16–50 μm being ruptured (from [151]*).*

6.7. Influence of the Fluid on the Capsule's Strength

Taking into consideration the previous results, it can be said that the internal liquid has an important effect on the force–displacement relationship.

Figure 58 shows an image sequence of the simulation of the parallel compression test of a single liquid core–shell capsule. Figure 58(a) shows the pressure of the internal fluid at the beginning of the test. As the capsule was compressed by the upper plate load and deformed, the pressure increased due to the load applied by the upper plate (Figure 58(b) and Figure 58(c)). Finally, when the capsule started to break, the pressure of the fluid inside the capsule reduced because of the fluid released through the broken shell (Figure 58(d)).

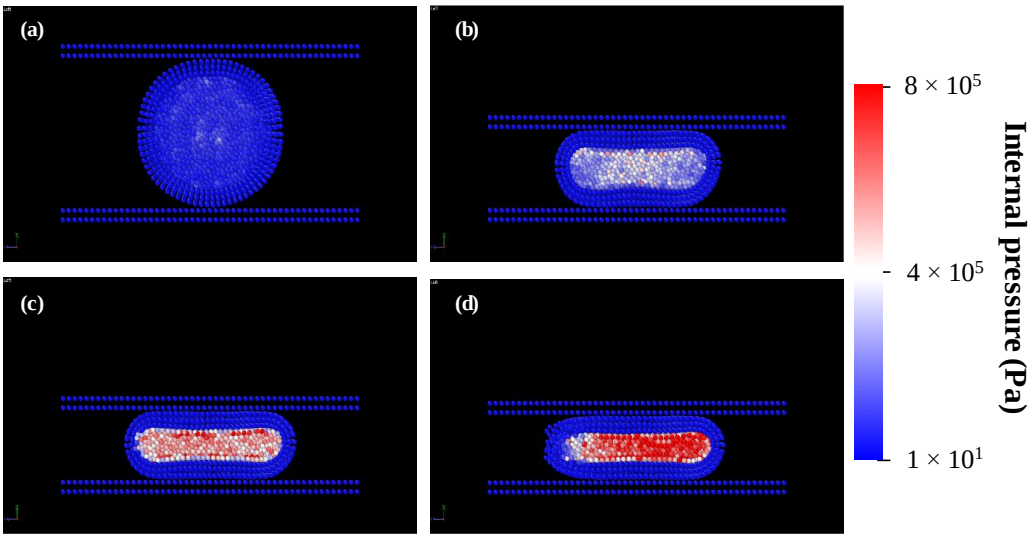


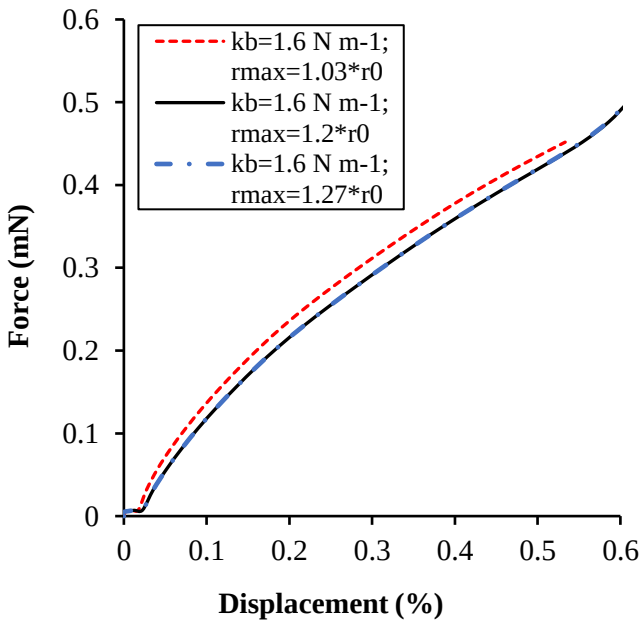
Figure 58. Sequence of the simulation of the parallel compression test of a single liquid core–shell capsule at different stages

6.8. Deformability and Strength of the Capsule (a Parametric Study)

In this section, a parametric study was carried out to understand how the behaviour of the capsule is affected by its mechanical properties: in particular, by k_b (which is related to the Young's modulus by Equation (20) and r_{max} (which provides the maximal local displacement before rupture). Three different values of k_b (i.e., 14, 4.7, and 1.6 N m^{-1}) and r_{max} (i.e., 1.03·r_0, 1.2·r_0, and 1.27·r_0) and all nine possible pairings of these parameters were studied.

Lower r_{max} values imply that the distances required to break the computational springs are shorter. This can be seen, for instance, in Figure 59(b). Given the same k_b, the capsule broke when the displacement reached 45% for r_{max} = 1.03·r_0 and 54% for r_{max} = 1.2·r_0. The load that initiated the breakage of the capsule was also lower (0.54 versus 1.46 mN). This effect was observed for all three values of k_b, but it was more evident at high values of k_b.

(a)



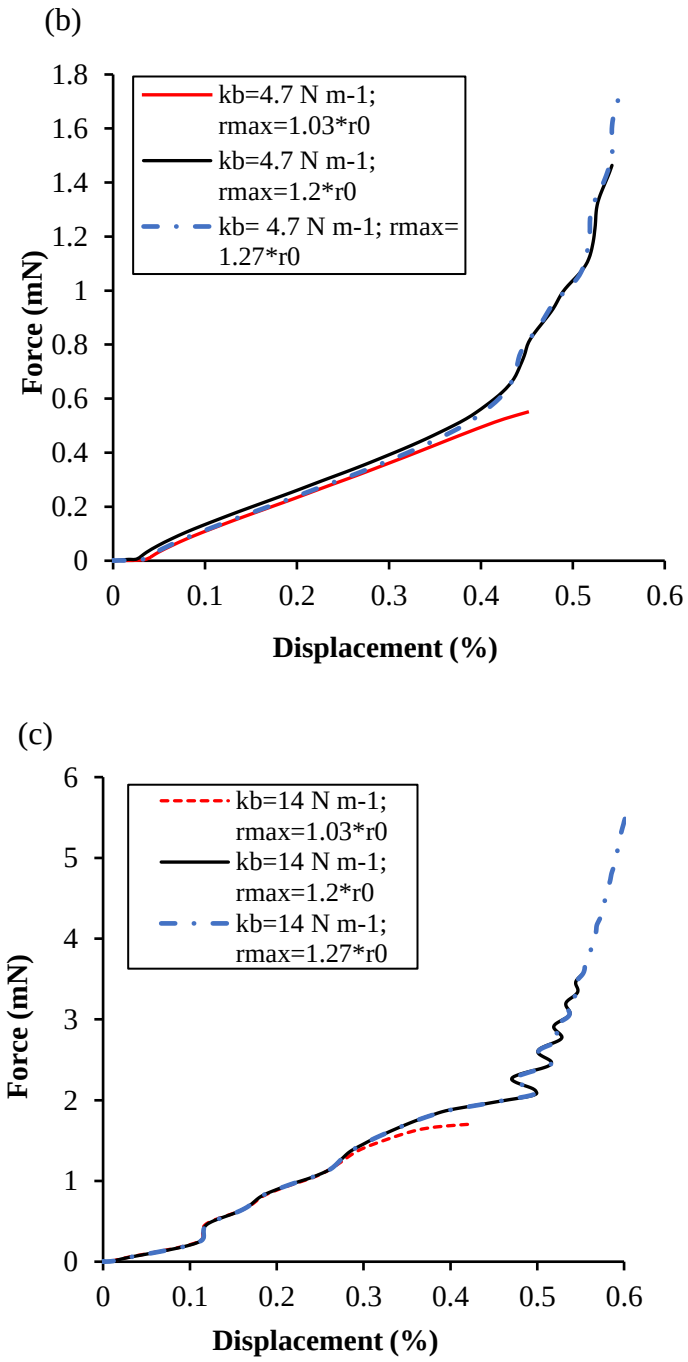


Figure 59. Simulated force–displacement curves for (a) kb = 1.6 N−1 m and different values of rmax, (b) kb = 4.7 N−1 m and different values of rmax and (c) kb = 1.6 N−1 m and different values of rmax.

As Figure 59 and Figure 60 show, lower values of r_{max} mean that the local deformations required to break a computational bond are lower. As a result of this,

breakage occurred at lower displacements in the simulations where r_{max} was lower. High values of k_b mean high Young's moduli (see Equation (20)). The shell was more rigid and, when it broke, the fracture started at a single location and propagated from there, forming a single wedge-shaped gash. When k_b was low, the capsule was flexible and showed little resistance to compression. In this case, the capsule tended to break at various locations at the same time during compression.

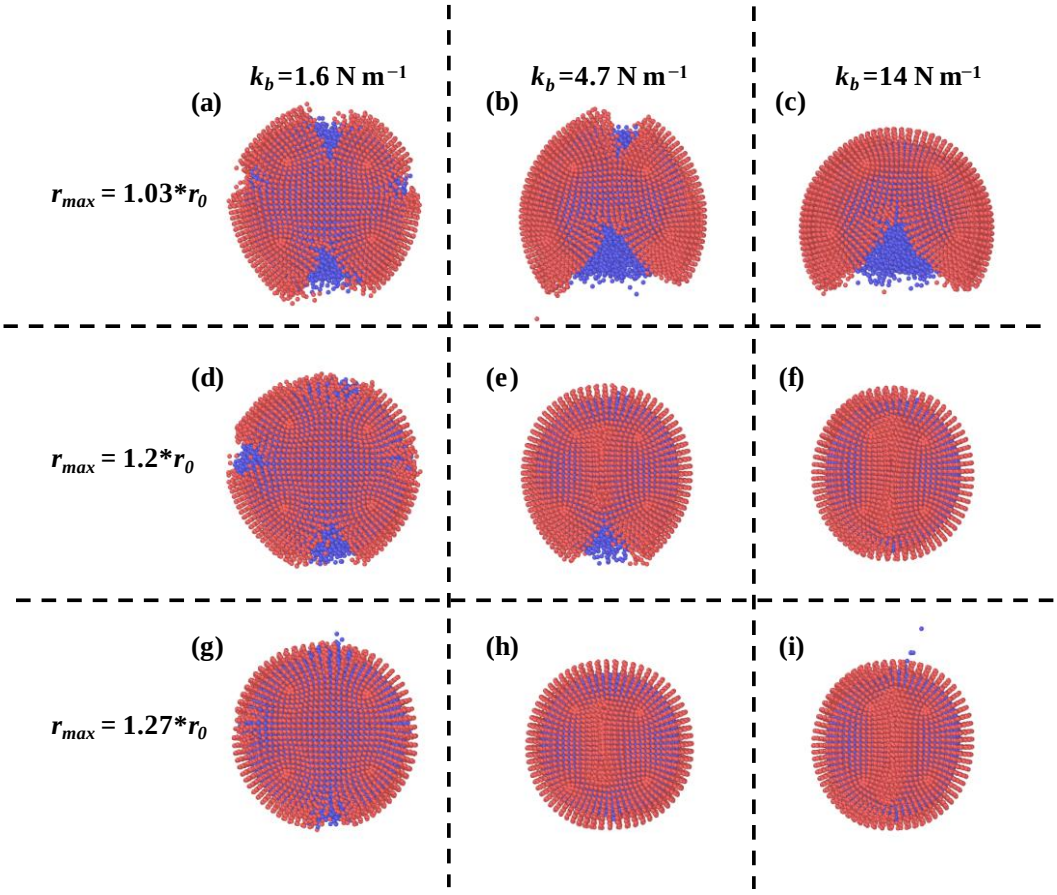


*Figure 60. Capsule fractures (view from the top) at the end of each simulation**

***** (a) k_b =1.6 N m^{-1} and r_{max} = 1.03*r0; (b) k_b =4.7 N m^{-1} and r_{max} = 1.03*r0; (c) k_b = 14 N m^{-1} and r_{max} = 1.03*r0; (d) k_b =1.6 N m^{-1} and r_{max} = 1.2*r0; (e) k_b =4.7 N m^{-1} and r_{max} = 1.2*r0; (f) k_b = 14 N m^{-1} and r_{max} = 1.2*r0; (g) k_b = 1.6 N m^{-1} and r_{max} = 1.27*r0; (h) k_b = 4.7 N m^{-1} and r_{max} = 1.27*r0; (i) k_b = 14 N m^{-1} and r_{max} = 1.27*r0;

CHAPTER 7

7. Conclusions and Recommendations for Future Research

7.1. Conclusions

The aims of this research was clearly differentiated into 3 sections. First of all it was crucial to analyse the influence of the proportions of the capsule materials (oil, water, and alginate) on the strength and diameter of capsules for asphalt self-healing in order to posteriorly relate them with the asphalt performance. In addition, it aims to provide a preliminary explanation about the diffusion of oil through the shell materials when the capsules are subjected to changes of temperature or compressive load is applied. Secondly, the optimization of capsule size and strength to maximise the self-healing properties of asphalt roads without compromising fatigue durability, skidding resistance, and rutting resistance. This second part of the research presented in Chapter 5 would validate the application of encapsulated bitumen rejuvenators as an effective technology for the reflective cracking mitigation. Finally, it was aimed to develop a three-dimensional numerical model to simulate the failure of liquid-core capsules, by validating experimentally capsule mechanical properties such as the Force-Displacement curve, Young's modulus and the type of

fracture. This model could be the starting point for a future development of an automated tool for capsules design.

In the following sections, a detailed review of the main findings and conclusions are summarised after the analysis of the results obtained in the previous sections.

7.1.1. Capsule characterization to maximize asphalt self-healing properties

Calcium-alginate capsules with a range of sizes and strengths were manufactured by modifying the (i) diameter and (ii) oil and calcium alginate ratio, O/A ratio. The influence of the capsule's size and strength in the internal structure of the capsule, thermal and mechanical properties and the oil release mechanism was analysed and, based on the results obtained, the following conclusions were the most relevant:

- The calcium-alginate capsules were not degraded by the high temperature reached in the mixing and compaction processes, 160 ˚C. In average, the capsules lost 3.87% of mass, mostly due to water losses.
- After 7 cycles of temperature change, -10 ˚C to 60 ˚C and back to -10 ˚C, the capsules increased their diameter permanently in about 1%.
- Capsule's porosity increased with the O/A ratio.
- The capsules' strength increased with higher O/A ratio and diameter. It decreased with temperature increases.
- Calcium-alginate capsules may release between 10% and 46% of their total payload when they are embedded in the asphalt. This implies that the capsules can still release oil after healing a crack, which indicates that they may heal a crack several times.
- Capsules with bigger pore sizes release more oil, which may make them more efficient healing asphalt.

7.1.2. Optimisation of self-healing properties for asphalts containing encapsulated oil

The main objective in Chapter 5 was to assess the addition of encapsulated sunflower oil with different sizes and strengths in stone mastic asphalt as a mitigation technique for reflective cracking. It is also important to state that the results and conclusions shown in this section are related to the specific asphalt mixture described in the methodology. Additionally, the influence of the strength and the capsule size in the fatigue durability, self-healing properties, rutting and skid resistance have been assessed. Based on the results discussed in Chapter 5, the following conclusions were obtained:

- The capsules cause a slight reduction in the air voids content. This may be due to their small size, which causes them to sim-ply occupy space in the voids of the solid skeleton.
- 30% of the median number of cycles resisted by the asphalt is the moment when asphalt self-healing is most effective.
- The fatigue durability of the asphalt mixtures is decreased when bigger and weaker capsules are used. These types of capsules increase the self-healing properties due to the higher amount of sunflower oil released by the capsules.
- The addition of weaker capsules, which promote optimal healing, may also reduce the fatigue durability of the asphalt mixtures. Capsules that increase the self-healing of asphalt also promote rutting.
- There is a direct linear relationship between the rutting promoted by capsules and the amount of oil that the capsules release.
- The healing index is directly related to the amount of oil released by the capsules.
- Capsules reduce the skidding resistance of asphalt. However, this difference is not significant to produce a real risk of skidding on the surface of the asphalt

- Capsules may delay reflective cracking, increasing the durability of asphalt up to 21%. Besides, this type of capsule does not show a significant loss in rutting or skid resistance.

7.1.3. Computational simulation of fluid-structure interaction and breakage of capsules

A Discrete Multi-Physics model to simulate capsules formed by a shell containing a fluid was proposed in Chapter 6. The liquid core was implemented with Smoothed Particle Hydrodynamics and the solid shell with the Lattice Spring Model. The model was validated against experimental compression of a single core–shell capsule between two parallel plates.

The results showed that:

- The model replicates with good accuracy the behaviour of the real capsule. Three different stages were highlighted in the force–displacement curve occurring during the compression. In the first stage, the load was supported by the external shell and the behaviour was Hertzian (i.e., the force was proportional to $\delta 3/2$). During the second stage, the stress reached the fluid, which added additional resistance to the compression. Finally, in the third stage, the capsule broke and collapsed.
- After the model had been validated, a parametric study showed how the breakage of the capsule depended on its material properties. By changing the material properties, (i) the maximal stress the capsule can resist before breaking, and (ii) the mode of breakage were varied. In some cases, the shell cracked at one point that opened a wide gash in the capsule. In other cases, the shell fractured at multiple locations. This affected the way the liquid was released from the capsule. In the first scenario, the release was not uniform and was concentrated at one side of the capsule. In the second, the liquid was released from multiple points distributed around the capsule.

- The proposed model can help the design of capsules with specific features. For instance, the mechanical properties of the capsule can be adjusted to make sure that it breaks only when a precise stress level is reached.
- The model also simulates the liquid release occurring after breakage. In this way, capsules can be designed to make sure that the liquid is released effectively. In fact, the capsule breaks in different ways according to its mechanical properties, and only specific combinations of these properties allow for a uniform release of the liquid after breakage.

7.2. Recommendations for Future Research

This section provides some research lines to be followed as future work in order to optimize the properties of the capsules, minimize the production cost and have a smart and efficient application.

One of the most important concerns regarding the application of encapsulated rejuvenators is the cost. The manufacturing cost of the Ca-alginate capsules has been relatively high in comparison to other additives used to prolong the lifespan of the road. For this reason, conducting a whole life cost analysis of a road containing encapsulated bitumen rejuvenators would be highly recommended. It is expected to reduce production cost with the automation of the capsules manufacture and increment in the efficiency of the materials used.

Additionally, it could be interesting to analyse in which specific part of the road, the capsules could be more needed or have higher effectiveness. Capsules could have a good performance in areas where reflective cracking, ravelling or faster ageing of the bitumen are expected whereas they could be counterproductive where rutting is expected to be road distress. In addition to that, more research could be required with different types of bitumen. It was demonstrated that certain re-compaction is related to the bitumen softening caused by the sunflower oil and the healing of the cracks. Therefore, differences in the self-healing properties of the asphalt could be found for bitumens with different softening points or penetration values.

In order to increase the effectiveness of the capsules, and therefore to reduce the price, it would be interesting to increase the sunflower oil released ratio by the capsule. Another possibility to release the sunflower oil left inside the capsule could be the action of an external factor which could promote a multi-time healing process and increment of the self-healing properties.

Based on the experiments carried out, the optimum resting period time should take place after 30 % of the total number of cycles of the asphalt material in a fatigue test. This indicates that a high percentage of the microcracks that the capsules are able to heal occur at that moment. It could be interesting to combine two different types of capsules with different strengths in the same asphalt material for the healing of two different types of microcrack.

In light of future commercialization of the capsules as an additive to prolong the lifespan of the roads, the influence of the temperature should be also analysed in the self-healing properties and the rest of the properties (rutting, fatigue…) of the asphalt containing encapsulated rejuvenators.

Finally, it would be interesting to develop software able to predict the optimum size and strength of the capsule determined by the traffic load, the optimum moment for the capsule to release the oil and the environmental factors. The simulation of this type of phenomenon by means of a Multiphysics model is indicated to have a high potential as demonstrated in this thesis.

REFERENCES

[1] D. Y. Zhu, M. Z. Rong, and M. Q. Zhang, "Self-healing polymeric materials based on microencapsulated healing agents: From design to preparation," *Prog. Polym. Sci.*, vol. 49–50, pp. 175–220, 2015.

[2] B. Blaiszik *et al.*, "Self-Healing Polymers and Composites," *Annu. Rev. Mater. Res*, vol. 40, no. 1, pp. 179–211, 2010.

[3] A. Tabakovic and E. Schlangen, "Self-Healing Technology for Asphalt Pavements," *Adv. Polym. Sci.*, vol. 54, no. 3–4, pp. 349–359, 2016.

[4] R. Micaelo, T. Al-Mansoori, and A. Garcia, "Study of the mechanical properties and self-healing ability of asphalt mixture containing calcium-alginate capsules," *Constr. Build. Mater.*, vol. 123, pp. 734–744, 2016.

[5] B. Gómez-Meijide, H. Ajam, A. Garcia, and S. Vansteenkiste, "Effect of bitumen properties in the induction healing capacity of asphalt mixes," *Constr. Build. Mater.*, vol. 190, pp. 131–139, 2018.

[6] A. Garcia-Hernández, S. Salih, I. Ruiz-Riancho, J. Norambuena-Contreras, R. Hudson-Griffiths, and B. Gomez-Meijide, "Self-healing of reflective cracks in asphalt mixtures by the action of encapsulated agents," *Constr. Build. Mater.*, vol. 252, p. 118929, 2020.

[7] D. Grossegger, B. Gomez-Meijide, S. Vansteenkiste, and A. Garcia, "Influence of rheological and physical bitumen properties on heat-induced self-healing of asphalt mastic beams," *Constr. Build. Mater.*, vol. 182, pp. 298–308, 2018.

[8] D. Grossegger and A. Garcia, "Influence of the thermal expansion of bitumen on asphalt self-healing," *Appl. Therm. Eng.*, vol. 156, no. April, pp. 23–33, 2019.

[9] European Union Road Federation, "Road Statitics Yearbook 2016," no. 32, pp. 1–90, 2020.

[10] G. D. Airey, "State of the Art Report on Ageing Test Methods for

Bituminous Pavement State of the Art Report on Ageing Test Methods for Bituminous Pavement Materials," *Int. J. Pavement Eng.*, no. 4:3, pp. 165–176, 2003.

[11] N. Dhakal, M. A. Elseifi, and Z. Zhang, "Mitigation strategies for reflection cracking in rehabilitated pavements – A synthesis," *Int. J. Pavement Res. Technol.*, vol. 9, no. 3, pp. 228–239, 2016.

[12] S. Hu, F. Zhou, and T. Scullion, "Reflection cracking-based asphalt overlay thickness design and analysis tool," *Transp. Res. Rec.*, no. 2155, pp. 12–23, 2010.

[13] T. Al-Mansoori, "Self-healing properties of asphalt mixtures with embedded capsules," in *Advances in Materials and Pavement Performance Prediction - Proceedings of the International AM3P Conference, 2018*, 2018, pp. 551–555.

[14] T. Al-Mansoori, J. Norambuena-Contreras, R. Micaelo, and A. Garcia, "Self-healing of asphalt mastic by the action of polymeric capsules containing rejuvenators," *Constr. Build. Mater.*, vol. 161, pp. 330–339, 2018.

[15] J. Norambuena-Contreras, Q. Liu, L. Zhang, S. Wu, E. Yalcin, and A. Garcia, "Influence of encapsulated sunflower oil on the mechanical and self-healing properties of dense-graded asphalt mixtures," *Mater. Struct. Constr.*, vol. 52, no. 4, pp. 1–13, 2019.

[16] R. Micaelo, A. C. Freire, and G. Pereira, "Asphalt self-healing with encapsulated rejuvenators: effect of calcium-alginate capsules on stiffness, fatigue and rutting properties," *Mater. Struct. Constr.*, vol. 53, no. 1, pp. 1–17, 2020.

[17] B. Huang, G. Li, D. Vukosavljevic, X. Shu, and B. K. Egan, "Laboratory Investigation of Mixing Hot-Mix Asphalt with Reclaimed Asphalt Pavement," *Transp. Res. Rec. J. Transp. Res. Board*, vol. 1929, no. 1, pp. 37–45, 2005.

[18] NAPA, "Thin Hot Mix Asphalt Surfacings. Information Series 110," *Natl. Asph. Pavement Assoc.*, vol. Lanham, MD, p. 1995, 1995.

[19] NCHRP, "Report 673: A Manual for Design of Hot-Mix Asphalt with Commentary," *Natl. Coop. Highw. Res. Progr.*, vol. Sterling, p. 2011, 2011.

[20] G. D. Airey, A. E. Hunter, and A. C. Collop, "The effect of asphalt mixture gradation and compaction energy on aggregate degradation," *Constr. Build.*

Mater., vol. 22, no. 5, pp. 972–980, 2008.

[21] D. Pearson, "Deterioration and Maintenance of Pavements," *ICE Publ.*, vol. London, Un, 2012.

[22] W. Woods and A. Adcox, "A General Characterization of Pavement System Failures, with Emphasis on a Method for Selecting a Repair Process," *J. Constr. Educ.*, vol. 7, pp. 58–62, 2002.

[23] N. Thom, "Principles of Pavement Engineering," *ICE Publ.*, vol. London, Un, 2014.

[24] S. S. Adlinge and A. K. Gupta, "Pavement Deterioration and its Causes," *Mech. Civ. Eng.*, pp. 9 – 15, 2009.

[25] R. L. Lytton, "Use of geotextiles for reinforcement and strain relief in asphalt concrete," *Geotext. Geomembranes*, vol. 8, no. 3, pp. 217–237, 1989.

[26] J. Baek, H. Ozer, H. Wang, and I. L. Al-Qadi, "Effects of Interface Conditions on Reflective Cracking Development in Hot-Mix Asphalt Overlays," *Road Mater. Pavement Des.*, vol. 11, no. 2, pp. 307–334, 2010.

[27] R. Wu, J. T. Harvey, and J. M. Signore, "Cracking and rutting performance of composite pavements under testing with heavy vehicle simulator: Rubberized hot-mix asphalt with gap-graded aggregates over portland cement concrete," *Transp. Res. Rec.*, vol. 2304, pp. 177–184, 2012.

[28] J. W. Button and R. L. Lytton, "Guidelines for using geosynthetics with hot-mix asphalt overlays to reduce reflective cracking," *Transp. Res. Rec.*, no. 2004, pp. 111–119, 2007.

[29] S. J. Lee, "Mechanical performance and crack retardation study of a fiberglass-grid-reinforced asphalt concrete system," *Can. J. Civ. Eng.*, vol. 35, no. 10, pp. 1042–1049, 2008.

[30] J. Baek and I. L. Al-Qadi, "Effectiveness of Steel Reinforcing Interlayer Systems on Delaying Reflective Cracking," *Airf. Highw. Pavements*, pp. 486–497, 2006.

[31] B. J. Dempsey, "Development and performance of interlayer stress-absorbing composite in asphalt concrete overlays," *Transp. Res. Rec.*, no. 1809, pp. 175–183, 2002.

[32] O. M. Ogundipe, N. Thom, and A. Collop, "Investigation of crack

resistance potential of stress absorbing membrane interlayers (SAMIs) under traffic loading," *Constr. Build. Mater.*, vol. 38, pp. 658–666, 2013.

[33] D. Bischoff, "Evaluation of Strata ® Reflective Crack Relief System Final Report," vol. Report Num, 2007.

[34] M. R. Thompson, "Hot-Mix Asphalt Overlay Design Concepts for Rubblized Portland Cement Concrete Pavements," *Transp. Res. Rec.*, no. 99–0922, pp. 147–155, 1998.

[35] M. L. Nguyen, J. Blanc, J. P. Kerzrého, and P. Hornych, "Review of glass fibre grid use for pavement reinforcement and APT experiments at IFSTTAR," *Road Mater. Pavement Des.*, vol. 14, no. SUPPL.1, pp. 287–308, 2013.

[36] T. Report and S. Page, "Cost Effective Prevention of Reflective Cracking of Composite Pavement September 2011 6.," no. 2, 2011.

[37] S. W. Lee, J. M. Bae, S. H. Han, and S. M. Stoffels, "Evaluation of optimum rubblized depth to prevent reflection cracks," *J. Transp. Eng.*, vol. 133, no. 6, pp. 355–361, 2007.

[38] M. Niederquell, G. G. Baladi, and K. Y. Chatti, "Rubblization of Concrete Pavements: Field Investigation," *Transp. Res. Rec. J. Transp. Res. Board*, vol. 1730, no. 1, pp. 150–160, 2000.

[39] M. Elseifi and N. Dhakal, "Mitigation Strategies of Reflection Cracking in Pavement," no. May 2015, p. 111, 2015.

[40] H. Ajam, P. Lastra-González, B. Gómez-Meijide, G. Airey, and A. Garcia, "Self-healing of dense asphalt concrete by two different approaches: Electromagnetic induction and infrared radiation," *J. Test. Eval.*, vol. 45, no. 6, pp. 1933–1940, 2017.

[41] J. Norambuena-Contreras and A. Garcia, "Self-healing of asphalt mixture by microwave and induction heating," *Mater. Des.*, vol. 106, pp. 404–414, 2016.

[42] A. González, J. Norambuena-Contreras, L. Storey, and E. Schlangen, "Self-healing properties of recycled asphalt mixtures containing metal waste: An approach through microwave radiation heating," *J. Environ. Manage.*, vol. 214, pp. 242–251, 2018.

[43] J. Gallego, M. A. Del Val, V. Contreras, and A. Páez, "Heating asphalt mixtures with microwaves to promote self-healing," *Constr. Build. Mater.*,

vol. 42, pp. 1–4, 2013.

[44] H. Wang, J. Yang, G. Lu, and X. Liu, "Accelerated healing in asphalt concrete via laboratory microwave heating," *J. Test. Eval.*, vol. 48, no. 2, 2020.

[45] B. M. D. Hager, P. Greil, C. Leyens, S. Van Der Zwaag, and U. S. Schubert, "Self-Healing Materials," pp. 5424–5430, 2010.

[46] T. Al-Mansoori, J. Norambuena-Contreras, and A. Garcia, "Effect of capsule addition and healing temperature on the self-healing potential of asphalt mixtures," *Mater. Struct. Constr.*, vol. 51, no. 2, pp. 1–12, 2018.

[47] I. Gonzalez-Torre and J. Norambuena-Contreras, "Recent advances on self-healing of bituminous materials by the action of encapsulated rejuvenators," *Constr. Build. Mater.*, vol. 258, p. 119568, 2020.

[48] T. Al-Mansoori, R. Micaelo, I. Artamendi, J. Norambuena-Contreras, and A. Garcia, "Microcapsules for self-healing of asphalt mixture without compromising mechanical performance," *Constr. Build. Mater.*, vol. 155, pp. 1091–1100, 2017.

[49] A. Garcia, E. Schlangen, M. Van De Ven, and G. Sierra-Beltrán, "Preparation of capsules containing rejuvenators for their use in asphalt concrete," *J. Hazard. Mater.*, vol. 184, pp. 603–611, 2010.

[50] A. Garcia, J. Jelfs, and C. J. Austin, "Internal asphalt mixture rejuvenation using capsules," *Constr. Build. Mater.*, vol. 101, pp. 309–316, 2015.

[51] J. Norambuena-Contreras, E. Yalcin, R. Hudson-Griffiths, and A. García, "Mechanical and Self-Healing Properties of Stone Mastic Asphalt Containing Encapsulated Rejuvenators," *J. Mater. Civ. Eng.*, vol. 31, no. 5, pp. 1–10, 2019.

[52] J. Norambuena-contreras, E. Yalcin, A. Garcia, T. Al-mansoori, M. Yilmaz, and R. Hudson-griffiths, "Effect of mixing and ageing on the mechanical and self-healing properties of asphalt mixtures containing polymeric capsules," *Constr. Build. Mater.*, vol. 175, pp. 254–266, 2018.

[53] B. Shu, S. Wu, L. Dong, Q. Wang, and Q. Liu, "Microfluidic synthesis of Ca-alginate microcapsules for self-healing of bituminous binder," *Materials (Basel).*, vol. 11, no. 4, pp. 1–15, 2018.

[54] J. F. Su and E. Schlangen, "Synthesis and physicochemical properties of high compact microcapsules containing rejuvenator applied in asphalt,"

Chem. Eng. J., vol. 198–199, pp. 289–300, 2012.

[55] Q. Liu *et al.*, "Preparation and characterization of self-healing microcapsules embedding waterborne epoxy resin and curing agent for asphalt materials," *Constr. Build. Mater.*, vol. 183, pp. 384–394, 2018.

[56] X. Tan *et al.*, "Preparation, characterization and repeated repair ability evaluation of asphalt-based crack sealant containing microencapsulated epoxy resin and curing agent," *Constr. Build. Mater.*, vol. 256, no. May, p. 119433, 2020.

[57] D. Sun, T. Lu, X. Zhu, B. Li, and Y. Tian, "Optimization of synthesis technology to improve the design of asphalt self-healing microcapsules," *Constr. Build. Mater.*, vol. 175, pp. 88–103, 2018.

[58] Á. García, E. Schlangen, and M. Van De Ven, "Properties of capsules containing rejuvenators for their use in asphalt concrete," *Fuel*, vol. 90, no. 2, pp. 583–591, 2011.

[59] A. Tabaković, W. Post, D. Cantero, O. Copuroglu, S. J. Garcia, and E. Schlangen, "The reinforcement and healing of asphalt mastic mixtures by rejuvenator encapsulation in alginate compartmented fibres," *Smart Mater. Struct.*, vol. 25, no. 8, 2016.

[60] A. Tabaković *et al.*, "The compartmented alginate fibres optimisation for bitumen rejuvenator encapsulation," *J. Traffic Transp. Eng. (English Ed.*, vol. 4, no. 4, pp. 347–359, 2017.

[61] A. Ammala, "Biodegradable polymers as encapsulation materials for cosmetics and personal care markets," *Int. J. Cosmet. Sci.*, vol. 35, no. 2, pp. 113–124, 2013.

[62] S. J. Lee and D. Y. Ying, "Encapsulation of fish oils," *Deliv. Control. Release Bioact. Foods Nutraceuticals*, pp. 370–403, 2008.

[63] H. Fu, Y. Liu, F. Adrià, X. Shao, W. Cai, and C. Chipot, "From material science to avant-garde cuisine. the art of shaping liquids into spheres," *J. Phys. Chem. B*, vol. 118, no. 40, pp. 11747–11756, 2014.

[64] B. Voncina, O. Kreft, V. Kokol, and W. T. Chen, "Encapsulation of Rosemary oil in ethylcellulose microcapsules," *Taiwan Text. Res. J.*, vol. 19, no. 1, pp. 10–15, 2009.

[65] F. Cárdenas-Bailón, G. Osorio-Revilla, and T. Gallardo-Velázquez, "Microencapsulation techniques to develop formulations of insulin for oral

delivery: A review," *J. Microencapsul.*, vol. 30, no. 5, pp. 409–424, 2013.

[66] M. D. Lopez, A. Maudhuit, M. J. Pascual-Villalobos, and D. Poncelet, "Development of formulations to improve the controlled-release of linalool to be applied as an insecticide," *J. Agric. Food Chem.*, vol. 60, no. 5, pp. 1187–1192, 2012.

[67] K. Van Tittelboom and N. De Belie, *Self-healing in cementitious materials-a review*, vol. 6, no. 6. 2013.

[68] K. Van Tittelboom, N. De Belie, D. Van Loo, and P. Jacobs, "Self-healing efficiency of cementitious materials containing tubular capsules filled with healing agent," *Cem. Concr. Compos.*, vol. 33, no. 4, pp. 497–505, 2011.

[69] Rama Dubey, T. C. Shami, and K. U. B. Rao, "Microencapsulation Technology and Applications Rama," *Def. Sci. J.*, vol. 59, no. 1, pp. 82–95, 2009.

[70] A. Nussinovitch, "Polymer macro- and micro-gel beads: Fundamentals and applications," *Polym. Macro- Micro-Gel Beads Fundam. Appl.*, no. Tomita 2001, pp. 1–303, 2010.

[71] N. V. N. Jyothi, P. M. Prasanna, S. N. Sakarkar, K. S. Prabha, P. S. Ramaiah, and G. Y. Srawan, "Microencapsulation techniques, factors influencing encapsulation efficiency," *J. Microencapsul.*, vol. 27, no. 3, pp. 187–197, 2010.

[72] E. Martins, D. Poncelet, R. C. Rodrigues, and D. Renard, "Oil encapsulation techniques using alginate as encapsulating agent: applications and drawbacks," *J. Microencapsul.*, vol. 34, no. 8, pp. 754–771, 2017.

[73] F. Tiarks, K. Landfester, and M. Antonietti, "Preparation of polymeric nanocapsules by miniemulsion polymerization," *Langmuir*, vol. 17, no. 3, pp. 908–918, 2001.

[74] R. Atkin, P. Davies, J. Hardy, and B. Vincent, "Preparation of aqueous core/polymer shell microcapsules by internal phase separation," *Macromolecules*, vol. 37, no. 21, pp. 7979–7985, 2004.

[75] A. Trojanowska, A. Nogalska, R. Garcia, M. Giamberini, and B. Tylkowski, "Technological solutions for encapsulation," *J. Magn. Magn. Mater.*, pp. 1–20, 2017.

[76] H. N. Yow and A. F. Routh, "Formation of liquid core–polymer shell microcapsules," *Soft Matter*, vol. 2, no. 11, pp. 940–949, 2006.

[77] A. Kanellopoulos, P. Giannaros, D. Palmer, A. Kerr, and A. Al-Tabbaa, "Polymeric microcapsules with switchable mechanical properties for self-healing concrete: Synthesis, characterisation and proof of concept," *Smart Mater. Struct.*, vol. 26, no. 4, 2017.

[78] A. Garcia, E. Schlangen, and M. van de Ven, "Two Ways of Closing Cracks on Asphalt Concrete Pavements: Microcapsules and Induction Heating," *Key Eng. Mater.*, vol. 417–418, pp. 573–576, 2009.

[79] A. Garcia, E. Schlangen, and M. Van De Ven, "Properties of capsules containing rejuvenators for their use in asphalt concrete," *Fuel*, vol. 90, no. 2, pp. 583–591, 2011.

[80] F. H. Tsai, Y. Kitamura, and M. Kokawa, "Liquid-core alginate hydrogel beads loaded with functional compounds of radish by-products by reverse spherification: Optimization by response surface methodology," *Int. J. Biol. Macromol.*, vol. 96, pp. 600–610, 2017.

[81] E. Martins, D. Poncelet, and D. Renard, "A novel method of oil encapsulation in core-shell alginate microcapsules by dispersion-inverse gelation technique," *React. Funct. Polym.*, vol. 114, pp. 49–57, 2017.

[82] E. Martins, D. Renard, J. Davy, M. Marquis, and D. Poncelet, "Oil core microcapsules by inverse gelation technique," *J. Microencapsul.*, vol. 32, no. 1, pp. 86–95, 2015.

[83] S. Abang, E. S. Chan, and D. Poncelet, "Effects of process variables on the encapsulation of oil in ca-alginate capsules using an inverse gelation technique," *J. Microencapsul.*, vol. 29, no. 5, pp. 417–428, 2012.

[84] R. Rodríguez-Dorado, M. Landín, A. Altai, P. Russo, R. P. Aquino, and P. Del Gaudio, "A novel method for the production of core-shell microparticles by inverse gelation optimized with artificial intelligent tools," *Int. J. Pharm.*, vol. 538, no. 1–2, pp. 97–104, 2018.

[85] F. H. Tsai, P. Y. Chiang, Y. Kitamura, M. Kokawa, and M. Z. Islam, "Producing liquid-core hydrogel beads by reverse spherification: Effect of secondary gelation on physical properties and release characteristics," *Food Hydrocoll.*, vol. 62, pp. 140–148, 2017.

[86] A. Gray, S. Egan, S. Bakalis, and Z. Zhang, "Determination of microcapsule physicochemical, structural, and mechanical properties," *Particuology*, vol. 24, pp. 32–43, 2016.

[87] Z. Zhang, J. D. Stenson, and C. R. Thomas, *Chapter 2 Micromanipulation*

in Mechanical Characterisation of Single Particles, vol. 37, no. 09. Elsevier, 2009.

[88] R. Mercadé-Prieto and Z. Zhang, "Mechanical characterization of microspheres capsules, cells and beads: A review," *J. Microencapsul.*, vol. 29, no. 3, pp. 277–285, 2012.

[89] R. Mercadé-Prieto, C. R. Thomas, and Z. Zhang, "Mechanical double layer model for Saccharomyces Cerevisiae cell wall," *Eur. Biophys. J.*, vol. 42, no. 8, pp. 613–620, 2013.

[90] M. O'Sullivan, Z. Zhang, and B. Vincent, "Silica-shell/oil-core microcapsules with controlled shell thickness and their breakage stress," *Langmuir*, vol. 25, no. 14, pp. 7962–7966, 2009.

[91] Y. Long, D. York, Z. Zhang, and J. A. Preece, "Microcapsules with low content of formaldehyde: preparation and characterization," *J. Mater. Chem.*, vol. 19, no. 37, p. 6882, 2009.

[92] S. R. White *et al.*, "Autonomic healing of polymer composites," *Nature*, vol. 409, no. 6822, pp. 794–797, 2001.

[93] A. P. Esser-Kahn, S. A. Odom, N. R. Sottos, S. R. White, and J. S. Moore, "Triggered release from polymer capsules," *Macromolecules*, vol. 44, no. 14, pp. 5539–5553, 2011.

[94] L. Lo, X. Lu, and D. Lloyd, "Dissolution testing of a controlled release capsule formulation: Challenges and solutions using a semi-automated dissolution system," *Dissolution Technol.*, vol. 20, no. 2, pp. 6–13, 2013.

[95] X. Roy, J. K. H. Hui, M. Rabnawaz, G. Liu, and M. J. MacLachlan, "Prussian blue nanocontainers: Selectively permeable hollow metal-organic capsules from block ionomer emulsion-induced assembly," *J. Am. Chem. Soc.*, vol. 133, no. 22, pp. 8420–8423, 2011.

[96] B. G. De Geest, C. Déjugnat, G. B. Sukhorukov, K. Braeckmans, S. C. De Smedt, and J. Demeester, "Self-rupturing microcapsules," *Adv. Mater.*, vol. 17, no. 19, pp. 2357–2361, 2005.

[97] B. M. Sauer, D. Streich, and W. Meier, "pH-Sensitive Nanocontainers," *Adv. Mater.*, no. 21, pp. 1649–1651, 2001.

[98] G. R. Liu and M. B. Liu, *Smoothed Particle Hydrodynamics, a meshfree particle method*. Singapore: World Scientific Publishing Co., 2003.

[99] G. R. Liu and Y. T. Gu, *An introduction to Meshfree Methods and their Programming*. Dordrecht: Springer, 2005.

[100] S. Li and W. K. Liu, "Meshfree and particle methods and their applications," *Appl. Mech. Rev.*, vol. 55, no. 1, p. 1, 2002.

[101] D. Garijo and F. J. Montans, "Meshless models for aerospace structures numerical simulation," Polytechnic University of madrid, 2015.

[102] H. Liu and P. Shi, "Meshfree Particle Method," *IEEE Int. Conf. Comput. Vis.*, 2003.

[103] W. C. Huang and D. B. Goldgof, "Adaptive-Size Meshes for Rigid and Nonrigid Shape Analysis and Synthesis," *IEEE Trans. Pattern Anal. Mach. Intell.*, vol. 15, no. 6, pp. 611–616, 1993.

[104] G. Hou, J. Wang, and A. Layton, "Numerical Methods for Fluid-Structure Interaction — A Review," *Commun. Comput. Phys.*, vol. 12, no. 02, pp. 337–377, Aug. 2012.

[105] C. S. Peskin, "The immersed boundary method," *Acta Numer.*, vol. 11, pp. 479–517, 2002.

[106] M. Ariane *et al.*, "Discrete multi-physics: A mesh-free model of blood flow in flexible biological valve including solid aggregate formation," *PLoS One*, vol. 12, no. 4, p. e0174795, Apr. 2017.

[107] M. Müller, S. Schirm, M. Teschner, B. Heidelberger, and M. Gross, "Interaction of fluids with deformable solids," *Comput. Animat. Virtual Worlds*, vol. 15, no. 3–4, pp. 159–171, 2004.

[108] M. Soleimani, P. Wriggers, H. Rath, and M. Stiesch, "Numerical simulation and experimental validation of biofilm in a multi-physics framework using an SPH based method," *Comput. Mech.*, vol. 58, no. 4, pp. 619–633, 2016.

[109] A. Komoróczi, S. Abe, and J. L. Urai, "Meshless numerical modeling of brittle-viscous deformation: First results on boudinage and hydrofracturing using a coupling of discrete element method (DEM) and smoothed particle hydrodynamics (SPH)," *Comput. Geosci.*, vol. 17, no. 2, pp. 373–390, 2013.

[110] B. Solenthaler, J. Schlafli, and R. Pajarola, "A unified particle model for fluid-solid interactions," *Comput. Animat. Virtual Worlds*, vol. 18, pp. 69–82, 2007.

[111] M. Müller, B. Solenthaler, R. Keiser, and M. Gross, “Particle-Based Fluid-Fluid Interaction,” no. July, pp. 29–31, 2005.

[112] A. G. . Strozzi *et al.*, “3D porous media liquid-solid interaction simulation using SPH modeling and tomographic images,” *Proc. 11th IAPR Conf. Mach. Vis. Appl. MVA 2009*, pp. 328–331, 2009.

[113] A. Alexiadis, “A new Framework for Modelling the Dynamics and the Breakage of Capsules, Vesicles and Cells in Fluid Flow,” *Procedia IUTAM*, vol. 16, no. 0, pp. 80–88, 2015.

[114] J. Walter, A. V. Salsac, D. Barthes-Biesel, and P. Le Tallec, “Coupling of finite element and boundary integral methods for a capsule in a Stokes flow,” no. March, pp. 829–850, 2010.

[115] J. Wretborn, R. Armiento, and K. Museth, “Animation of crack propagation by means of an extended multi-body solver for the material point method,” *Comput. Graph.*, vol. 69, pp. 131–139, 2017.

[116] N. Liu, X. He, S. Li, and G. Wang, “Meshless simulation of brittle fracture,” *Comput. Animat. Virtual Worlds*, vol. 22, no. April, pp. 115–124, 2011.

[117] P. Eberhard *et al.*, “Particles - Bridging the gap between solids and fluids,” *Procedia IUTAM*, vol. 10, pp. 161–179, 2013.

[118] L. Hedjazi, C. L. Martin, S. Guessasma, G. Della Valle, and R. Dendievel, “Application of the Discrete Element Method to crack propagation and crack branching in a vitreous dense biopolymer material,” *Int. J. Solids Struct.*, vol. 49, no. 13, pp. 1893–1899, 2012.

[119] S. M. Harrison and P. W. Cleary, *Towards modelling of fluid flow and food breakage by the teeth in the oral cavity using smoothed particle hydrodynamics (SPH)*, vol. 238, no. 2. 2014.

[120] P. Van Liedekerke, E. Tijskens, H. Ramon, P. Ghysels, G. Samaey, and D. Roose, “Particle-based model to simulate the micromechanics of biological cells,” *Phys. Rev. E - Stat. Nonlinear, Soft Matter Phys.*, vol. 81, no. 6, pp. 1–15, 2010.

[121] C. X. Wang, L. Wang, and C. R. Thomas, “Modelling the mechanical properties of single suspension-cultured tomato cells,” *Ann. Bot.*, vol. 93, no. 4, pp. 443–453, 2004.

[122] A. Alexiadis *et al.*, “Using discrete multi-physics for detailed exploration of hydrodynamics in an in vitro colon system,” *Comput. Biol. Med.*, vol.

81, no. December 2016, pp. 188–198, 2017.

[123] M. Ariane, S. Kassinos, S. Velaga, and A. Alexiadis, “Discrete multi-physics simulations of diffusive and convective mass transfer in boundary layers containing motile cilia in lungs,” *Comput. Biol. Med.*, vol. 95, no. January, pp. 34–42, 2018.

[124] M. Ariane, D. Vigolo, A. Brill, F. G. B. Nash, M. Barigou, and A. Alexiadis, “Using Discrete Multi-Physics for studying the dynamics of emboli in flexible venous valves,” *Comput. Fluids*, vol. 166, pp. 57–63, 2018.

[125] M. Ariane *et al.*, “Modelling and simulation of flow and agglomeration in deep veins valves using discrete multi physics,” *Comput. Biol. Med.*, vol. 89, no. July, pp. 96–103, 2017.

[126] A. Alexiadis, S. Ghraybeh, and G. Qiao, “Natural convection and solidification of phase-change materials in circular pipes: A SPH approach,” *Comput. Mater. Sci.*, vol. 150, no. April, pp. 475–483, 2018.

[127] K. Wu, D. Yang, and N. Wright, “A coupled SPH-DEM model for fluid-structure interaction problems with free-surface flow and structural failure,” *Comput. Struct.*, vol. 177, pp. 141–161, 2016.

[128] A. Alexiadis, “The discrete multi-hybrid system for the simulation of solid-liquid flows,” *PLoS One*, vol. 10, no. 5, pp. 1–26, 2015.

[129] Y. J. Huang and O. J. Nydal, “Coupling of discrete-element method and smoothed particle hydrodynamics for liquid-solid flows,” *Theor. Appl. Mech. Lett.*, vol. 2, no. 1, p. 012002, 2012.

[130] M. Zendehzaban, M. Ashjari, and S. Sharifnia, “Preparation of floatable TiO2/poly(vinyl alcohol)-alginate composite for the photodegradation of ammonia wastewater,” *Int. J. Energy Res.*, vol. 44, no. 3, pp. 2150–2163, 2020.

[131] Y. Al-Abdullat, S. Tsutsumi, N. Nakajima, M. Ohta, H. Kuwahara, and K. Ikeuchi, “Surface modification of magnesium by NaHCO3 and corrosion behavior in Hank’s solution for new biomaterial applications,” *Mater. Trans.*, vol. 42, no. 8, pp. 1777–1780, 2001.

[132] R. Shan *et al.*, “Immobilization of Calcined Layered Double Hydroxide into Alginate Hydrogel Beads for PNP and PAP Removal: Kinetics, Isotherms, Thermodynamics, and Mechanism,” *Water. Air. Soil Pollut.*, vol. 229, no. 10, 2018.

[133] J. Qiu, M. van de Ven, S. Wu, J. Yu, and A. Molenaar, "Evaluating Self Healing Capability of Bituminous Mastics," *Exp. Mech.*, vol. 52, no. 8, pp. 1163–1171, 2012.

[134] Á. García, "Self-healing of open cracks in asphalt mastic," *Fuel*, vol. 93, no. SEPTEMBER 2011, pp. 264–272, 2012.

[135] N. Ruiz-riancho, D. Grossegger, T. Saadoon, A. Garcia, and R. Hudson-, "Properties of Ca-alginate capsules to maximise asphalt self-healing properties," pp. 1–28.

[136] A. Rahmat, M. Barigou, and A. Alexiadis, "Deformation and rupture of compound cells under shear: A discrete multiphysics study," *Phys. Fluids*, vol. 31, no. 5, 2019.

[137] R. Mercadé-Prieto *et al.*, "Determination of the elastic properties of single microcapsules using micromanipulation and finite element modeling," *Chem. Eng. Sci.*, vol. 66, no. 10, pp. 2042–2049, 2011.

[138] J. J. Monaghan, "Smoothed particle hydrodynamics," *Reports Prog. Phys.*, vol. 68, no. 8, pp. 1703–1759, 2005.

[139] L. B. Lucy, "A numerical approach to the testing of the fission hypothesis," *Astron. J.*, vol. 82, no. 12, pp. 1013–1024, 1977.

[140] J. P. Morris, P. J. Fox, and Y. Zhu, "Modeling low Reynolds number incompressible flows using SPH," *Int. J. Numer. Methods Fluids*, no. 136, pp. 214–226, 1997.

[141] R. H. Cole, *Underwater explosions*. 1948.

[142] M. Kot, H. Nagahashi, and P. Szymczak, "Elastic moduli of simple mass spring models," *Vis. Comput.*, vol. 31, no. 10, pp. 1339–1350, 2015.

[143] S. Plimpton, "Fast parallel algorithms for short-range molecular dynamics," *Journal of Computational Physics*, vol. 117, no. 1. pp. 1–19, 1995.

[144] G. C. Ganzenm, M. O. Steinhauser, and P. Van Liedekerke, "The implementation of Smooth Particle Hydrodynamics in LAMMPS," *avilable online at https://lammps.sandia.gov/doc/PDF/SPH_LAMMPS_userguide.pdf*, pp. 1–23, 2011.

[145] I. H. Sahputra, A. Alexiadis, and M. J. Adams, "A Coarse Grained Model for Viscoelastic Solids in Discrete Multiphysics Simulations,"

ChemEngineering, vol. 4, no. 2, p. 30, 2020.

[146] S. F. Yap, M. J. Adams, J. P. K. Seville, and Z. Zhang, "Single and bulk compression of pharmaceutical excipients: Evaluation of mechanical properties," *Powder Technol.*, vol. 185, no. 1, pp. 1–10, 2008.

[147] H. Ghasemi, S. Darjani, H. Mazloomi, and S. Mozaffari, "Preparation of stable multiple emulsions using food-grade emulsifiers: evaluating the effects of emulsifier concentration, W/O phase ratio, and emulsification process," *SN Appl. Sci.*, vol. 2, no. 12, 2020.

[148] H. Ghasemi, B. Aghabarari, M. Alizadeh, A. Khanlarkhani, and N. Abu-Zahra, "High efficiency decolorization of wastewater by Fenton catalyst: Magnetic iron-copper hybrid oxides," *J. Water Process Eng.*, vol. 37, no. July, p. 101540, 2020.

[149] A. Sokolov, A. Mozaffari, R. Zhang, J. J. De Pablo, and A. Snezhko, "Emergence of Radial Tree of Bend Stripes in Active Nematics," *Phys. Rev. X*, vol. 9, no. 3, p. 31014, 2019.

[150] J. Li, S. Dong, W. Hua, X. Li, and X. Pan, "Numerical investigation of hydraulic fracture propagation based on cohesive zone model in naturally fractured formations," *Processes*, vol. 7, no. 1, 2019.

[151] Y. L. Ren, A. M. Donald, and Z. B. Zhang, "Investigation of radiation damage to microcapsules in environmental SEM," *Mater. Sci. Technol.*, vol. 23, no. 7, pp. 857–864, 2007.